ADVECTIVE-DIFFUSIVE SCALAR TRANSPORT IN LAMINAR PERIODIC FLOWS

AN EXPERIMENTAL INVESTIGATION

PROEFSCHRIFT

ter verkrijging van de graad van doctor aan de
Technische Universiteit Eindhoven, op gezag van de
rector magnificus prof. dr. ir. F. P. T. Baaijens, voor een
commissie aangewezen door het College voor
Promoties, in het openbaar te verdedigen
op maandag 28 september 2015 om 16.00 uur

door

Özge Başkan

geboren te Ankara, Turkije

Dit proefschrift is goedgekeurd door de promotoren en de samenstelling van de promotiecommissie is als volgt:

voorzitter:	prof. dr. ir. G. M. W. Kroesen
1$^\text{e}$ promotor:	prof. dr. H. J. H. Clercx
copromotor:	dr. ir. M. F. M. Speetjens
leden:	prof. dr. ir. G. J. F. van Heijst
	prof. dr. ir. J. M. J. den Toonder
	prof. dr. ir. P. D. Anderson
	prof. dr. M. Rudman (Monash University)
	dr. E. Gouillart (CNRS)

Aileme

CONTENTS

1

INTRODUCTION

If nature were not beautiful, it would not be worth studying it.
And life would not be worth living.

Henry Poincaré

Mixing of scalars in fluid systems occurs in a wide variety of natural systems and industrial applications. Examples of natural processes are transport of pollutants in the atmosphere and warm streams in oceans (Samelson and Wiggins, 2006; Wiggins, 2005), whereas water treatment in bioreactors (Alvarez et al., 2005) and micro-mixers (Nguyen and Wu, 2005) are examples of man-made industrial systems. The present study will focus on a particular class of mixing flows, namely inline mixing flows operating under laminar flow conditions. This flow configuration is key to many laminar mixing and heat-transfer processes in industry, including mixing and thermal processing of polymers (Aref, 2002; Ottino, 1989; Wiggins and Ottino, 2004), compact mixers and heat exchangers for pharmaceutical applications (Becht et al., 2007; Jaluria, 2003; Sunden and Shah, 2007) and a broad scope of micro-fluidic devices (Beebe et al., 2002; Bertsch et al., 2001; Meagher et al., 2008; Mills et al., 2000; Nguyen and Wu, 2005; Stone et al., 2004; Weigl et al., 2008). Such systems, notwithstanding their great practical relevance, are still primarily designed and optimized by way of empirical studies and practical experience. This motivates the present study, which seeks to deepen the fundamental understanding of scalar transport in inline mixing flows.

1.1. SCALAR TRANSPORT AND MIXING IN LAMINAR FLOWS

Advection and diffusion are the two fundamental mechanisms that determine mixing of non-reactive scalars. Diffusion is the molecular transport of a substance from a region of high concentration to a region of low concentration. Diffusion achieves a uniform final state – and thus good mixing – yet this takes a long time even in small-scale fluid systems. Advection is the transport of a substance by the motion of the fluid and, depending on the flow characteristics, can accelerate the mixing process significantly by rapidly increasing the interface across which diffusion can occur. The stochastic and irregular nature of turbulence invariably results in such rapid interface stretching and thus renders turbulent flows natural good-mixing flows. However, many (industrial) fluid systems operate under laminar flow conditions due to either high viscosity of the working fluid (e.g., food and polymer industry) or relatively small length scales of the system (e.g., microfluidics). Laminar flows are highly regular in that the wide range of vortical structures that characterizes turbulence are absent and fluid particles move in a far more orderly manner. The important consequence for scalar transport is that, contrary to turbulence, efficient mixing is not automatic in laminar flows. This can be exemplified by the famous dye experiments in a pipe flow of Reynolds (Reynolds, 1883). In the laminar regime, the injected dye remains entrapped in parallel layers (laminae); in the turbulent regime, on the other hand, the dye stream rapidly becomes mixed over the entire cross-section (Kundu and Cohen, 1990).

Scalar transport in laminar flows is typically characterized by the coexistence of regions with efficient mixing and regions with poor mixing. This is illustrated in Fig. 1.1 by the advection of a red and blue blob of a passive scalar in a simple laminar flow driven by alternating upward motion of the side walls. The red blob undergoes repeated stretching and folding, causing its interface to grow exponentially in time. This process is known as "chaotic advection" and is the fastest way to increase fluid interfaces and, thereby, the most efficient way to enhance mixing in a laminar flow. The blue blob, apart from some shearing, basically retains its initial compact shape and, consequently, no appreciably mixing

enhancement occurs here. This notion of chaotic versus non-chaotic advection has been put forward in the seminal paper by Aref (Aref, 1984) and has been the catalyst for a vast body of work on laminar mixing since the early 1980s.
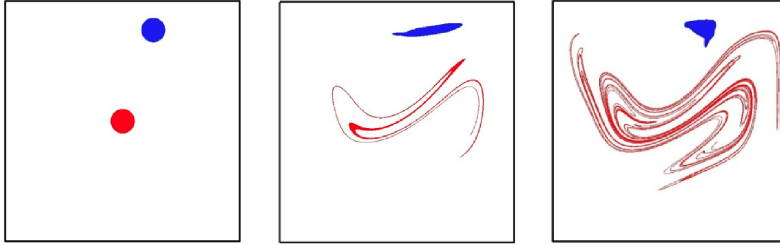
Figure 1.1: Chaotic advection (red) versus non-chaotic advection (blue) visualized by the evolution of two initially circular patches of dye in a 2D unsteady flow (left to right: progression in time).

1.2. LAGRANGIAN ANALYSIS OF ADVECTIVE TRANSPORT

Advection is determined by the motion of fluid particles induced by the flow itself and thereby is an essentially Lagrangian process. Hence, enhancement of laminar mixing must concentrate on the Lagrangian transport properties of a given flow. The Lagrangian framework leans on the equations of motion for fluid particles that are passively advected by the flow. For generic three-dimensional (3D) unsteady flows they are given by

$$\frac{d\boldsymbol{x}}{dt} = \boldsymbol{u}(\boldsymbol{x}, t), \tag{1.1}$$

where $\boldsymbol{x} = (x, y, z)$ and $\boldsymbol{u} = (u, v, w)$ are the momentary particle position and fluid velocity, respectively. For laminar flows this constitutes a non-autonomous deterministic dynamical system (Shivamoggi, 2014). Thus Lagrangian fluid trajectories of incompressible flows become analogous to the phase-space trajectories of conservative dynamical systems. This analogy enables application of dynamical-systems theory to the analysis of Lagrangian transport, which has proven instrumental to the investigation of laminar mixing.

In two-dimensional (2D) incompressible flows, equations of motion (1.1) admit expression in the form

$$\frac{dx}{dt} = u = \frac{d\psi}{dy}, \quad \frac{dy}{dt} = v = -\frac{d\psi}{dx} \tag{1.2}$$

with $\psi = \psi(x, y, t)$ the stream function. The 2D equations of motion (1.2) define a particular kind of dynamical system, namely a non-autonomous one-degree-of-freedom Hamiltonian system, with ψ the corresponding Hamiltonian. For steady flows, system (1.2) becomes autonomous, i.e. $\psi = \psi(x, y)$, and the fluid trajectories coincide with the streamlines described by the level sets of stream function ψ. This constitutes a so-called integrable state and admits only non-chaotic advection. Thus the Hamiltonian nature of (1.2) has the fundamental consequence that time dependence is a necessary (but not sufficient) condition for chaotic advection in 2D laminar flows (Aref, 1984; Ottino, 1989).

Accomplishment of chaotic advection in 2D unsteady flows, though fulfilling the condition of unsteadiness, is far from trivial, however. Typically a situation of coexisting chaotic and regular advection as illustrated in Fig. 1.1 exists. Such poor-mixing and good-mixing regions relate to coherent structures formed by the fluid trajectories and many studies have been devoted to visualization of such structures and investigation of their properties as a function of system parameters (Aref, 1984, 2002; Chaiken et al., 1986; Hwu et al., 1997; Jana et al., 1994a; Lester et al., 2009; Meleshko and Peters, 1996; Ottino, 1989; Stremler and Chen, 2007). This coherent-structure approach, arguably, is the most common within the context of Lagrangian mixing analyses yet other methods based on Lagrangian characteristics have been developed and successfully employed as well. This includes, among other approaches, techniques based on deformation and stretching characteristics of material elements (Haller, 2015; Shadden et al., 2005; Voth et al., 2002) and methods concerning purely topological properties, i.e. the concepts of ghost rods and braiding (Finn et al., 2006; Gouillart et al., 2006; Stremler et al., 2011; Thiffeault and Finn, 2006).

Laminar mixing in 3D configurations is far less explored due to two main reasons: (1) the much greater topological complexity of 3D fluid trajectories and coherent structures; (2) the fact that the 3D Lagrangian equations of motion (1.1) lack a well-defined structure analogous to the Hamiltonian structure of their 2D counterpart (1.2) (Speetjens et al., 2004). However, generalizations of Hamiltonian concepts to generic 3D flows exist (Bajer, 1994; Cartwright et al., 1996; Cheng and Sun, 1989; Mezić and Wiggins, 1994). A fundamental difference with 2D flows is that fluid particles in 3D flows admit complex dynamics (including chaotic advection) already under steady conditions (Bajer, 1994; Bajer and Moffatt, 1990; Dombre et al., 1986; Piro and Feingold, 1988). Hence, contrary to 2D flows, here distinction must be made between steady and unsteady flows. The present study is restricted to a particular class of 3D steady flows, viz. inline mixing flows, which will be elaborated below in Sec. 1.4; reviews on 3D unsteady flows are in Aref et al. (2014); Cartwright et al. (1996); Speetjens and Clercx (2013).

1.3. Eulerian analysis of advective-diffusive transport

The total mixing process involves an interplay of advection and diffusion (Sec. 1.1). The seminal (computational) work of Pierrehumbert (1994) revealed that, comparable to formation of coherent structures by fluid trajectories, advective-diffusive transport may also exhibit coherence in that self-similarly decaying patterns were observed in a diffusive scalar field stirred by a time-periodic flow. These repeating patterns were, due to their complex spatial structure, denoted "strange eigenmodes". Several numerical studies confirmed this observation by also exposing such strange eigenmodes that decayed exponentially in time (Antonsen Jr et al., 1996; Sukhatme and Pierrehumbert, 2002). First experimental evidence of this phenomenon was given by visualizations of transported fluorescent dye in an electromagnetically-driven 2D fluid layer Rothstein et al. (1999). They reported the existence of structurally-invariant, slowly-decaying mixing patterns and their quantitative analysis showed how advection and diffusion interplayed in the mixing of the scalar field.

The linearity of the transport equations governing advective-diffusive transport implies that the evolving scalar field $C(\boldsymbol{x}, t)$ possesses a generic eigenmode decomposition of the form

$$C(\boldsymbol{x}, t) = \sum_{k=0}^{\infty} \gamma_k \varphi_k(\boldsymbol{x}) e^{\mu_k t}, \tag{1.3}$$

with φ_k the eigenfunctions, μ_k the corresponding eigenvalues and γ_k the expansion coefficients (determined by the initial condition). Property $Re(\mu_k) \leq 0$ for advective-diffusive transport causes the terms in (1.3) to decay exponentially in time at a rate determined by the time constant $\tau_k = -1/Re(\mu_k)$. The decay rates are typically different, meaning that the evolution quickly becomes dominated by the slowest-decaying contribution and thus to good approximation assumes the form

$$C(\boldsymbol{x}, t) \approx \gamma_0 \varphi_0(\boldsymbol{x}) e^{\mu_0 t} + C_{\infty}(\boldsymbol{x}), \tag{1.4}$$

with $k = 0$ (by definition) the slowest-decaying contribution and $C_{\infty}(\boldsymbol{x})$ the steady state. The leading term $\gamma_0 \varphi_0(\boldsymbol{x}) e^{\mu_0 t}$ in (1.4) is the so-called "dominant eigenmode" of the evolution and results in a self-similarly decaying pattern (time constant $\tau_0 = -1/Re(\mu_0)$) with spatial distribution $\gamma_0 \varphi_0(\boldsymbol{x})$. The before-mentioned strange eigenmode corresponds with this dominant eigenmode; the term "strange" refers to the typically very complex spatial structure of this eigenmode in case of advection-dominated transport. The eigenmode decomposition (1.3) and the notion of dominant (or strange) eigenmodes following (1.4) have proven to be a very powerful concept for gaining (fundamental) insight into the advective-diffusive transport of scalars (Gorodetskyi et al., 2014; Gouillart et al., 2008; Lester et al., 2009; Liu and Haller, 2004; Metcalfe et al., 2012; Popovych et al., 2007; Singh et al., 2009). Dominant eigenmodes and their decay rates e.g. enable characterization of the scalar transport without the need for full resolution of the scalar field (Lester et al., 2009). Important to note is that recent developments in operator theory show that the decomposition (1.3) – and thus the entire machinery of eigenmode analyses – generalizes to nonlinear systems (Mezic, 2013).

1.4. SCALAR TRANSPORT IN INLINE MIXING FLOWS

The present study considers a particular class of 3D steady flows, viz. inline mixing flows, which consist of a (pressure-driven) continuous throughflow in a duct that is "stirred" in transverse direction via systematic reorientation of the cross-sectional flow by e.g. internal elements or boundary forcing. This flow configuration underlies many laminar mixing and heat-transfer processes in industry, ranging from the mixing and thermal processing of polymers (Aref, 2002; Ottino, 1989; Wiggins and Ottino, 2004) via compact mixers and heat exchangers for pharmaceutical applications (Becht et al., 2007; Jaluria, 2003; Sunden and Shah, 2007) down to micro-fluidic devices (Beebe et al., 2002; Bertsch et al., 2001; Meagher et al., 2008; Mills et al., 2000; Nguyen and Wu, 2005; Stone et al., 2004; Weigl et al., 2008). However, despite their great practical relevance, these systems are still primarily designed and optimized on the basis of empirical studies and practical experience. This

motivates the present study, which aims at deepening the fundamental understanding of scalar transport in inline mixing flows.

Scalar transport in inline mixing flows will be investigated by way of two representative case studies: the Rotated Arc Mixer (RAM) and the Quatro static mixer. The RAM is shown in Fig. 1.2 and consists of two concentric cylinders: a stationary inner cylinder (radius R) with consecutive windows (length L and opening angle Δ) that are offset in angular direction by an angle Θ and an outer rotating cylinder that induces a transverse flow via viscous drag at the windows (Metcalfe et al., 2006). This window offset accomplishes a systematic reorientation of the transverse flow after each axial "cell" of length L. Employing offsets Θ that are commensurate with 2π causes the window sequence to repeat itself after N cells (e.g. $\Theta = 2\pi/5$ yields $N = 5$). This results, upon omitting inlet and outlet effects, in an axially-periodic flow:

$$\boldsymbol{u}(x, y, z) = \boldsymbol{u}(x, y, z + NL). \tag{1.5}$$

Moreover, the flow in cell $1 \le k \le N$, located in axial segment $(k-1)L \le z \le kL$, is a reorientation of the flow $\boldsymbol{u}_1$ in the first cell ($k = 1$) following $\boldsymbol{u}(r, \theta, z) = \boldsymbol{u}_1(r, \theta - (k-1)\Theta, z)$. Here, the velocity is given in cylindrical coordinates for the ease of representation.
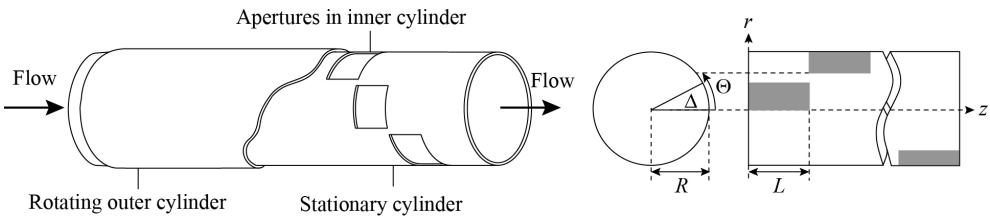
Figure 1.2: A schematic of the Rotated Arc Mixer (RAM). The left panel shows the geometry of the RAM with the rotating outer cylinder, stationary inner cylinder, and the axial throughflow. The right panel shows the definition of the cylindrical coordinate system, the cylinder radius R, offset angle Θ, aperture arc angle Δ, and the aperture length L. (Lester et al., 2009)

The Quatro mixer is shown in Fig. 1.3 and, similar to the RAM, consists of a cylinder with radius R. However, instead of via boundary forcing, transverse flow is here induced via internal mixing elements composed of chevron-shaped central plates of length L and diagonal $D = 2R$ with perpendicular elliptical segments extending to the inner wall of the cylinder (Jilisen et al., 2013). A part made of a central plate and four attached elliptical segments constitutes one mixing element and two consecutive elements relate via axial reflection about their connecting cross-section and subsequent rotation by 90°. Two consecutive elements, in turn, constitute one element pair (highlighted in gray-scale in Fig. 1.3) that is repeated successively in axial direction. This yields, as the RAM, an axially-periodic flow according to (1.5), with here $N = 2$.

The net axial throughflow results (besides exceptional cases) in streamlines that run from inlet $z = 0$ to outlet $z = NL$, which enables association of the downstream motion with an evolution in time (Speetjens et al., 2014). This becomes particularly simple in case of a uniform axial flow U, for which the axial position straightforwardly relates to time via $z = Ut$. This readily translates the 3D axially-periodic flow (1.5) into a 2D time-periodic
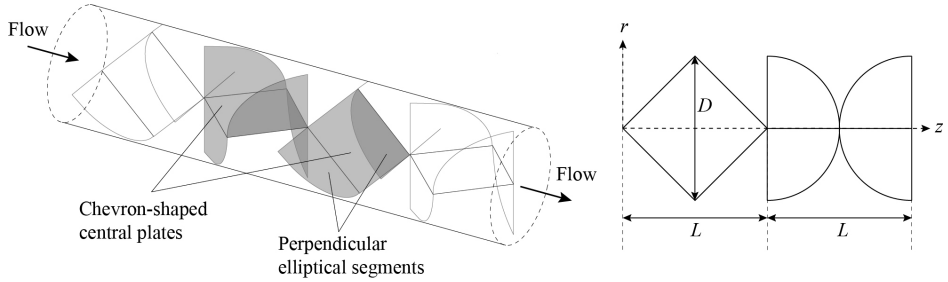
Figure 1.3: A schematic of the Quatro mixer. The left panel shows the geometry of the Quatro mixer with the chevron-shaped central plates, perpendicular elliptical segments extending to the cylinder wall and the axial throughflow. The right panel shows the r-axis and z-axis of the cylindrical coordinate system, the cylinder diameter and the diagonal D and the element length L.

flow

$$u(x, y, t) = u(x, y, t + T), \quad v(x, y, t) = v(x, y, t + T), \tag{1.6}$$

in the cross-sectional coordinates (x, y), with period time $T = NL/U$. Moreover, the cross-sectional equations of motion assume the Hamiltonian form (1.2), with $\psi(x, y, t) = \psi(x, y, t + T)$ the time-periodic stream function. Important for this study is that translation from 3D axially-periodic to 2D time-periodic flow, though technically more involved, is also possible in case of non-uniform axial flow (Speetjens et al., 2006, 2014).

The fact that 3D steady inline mixing flows are analogous to 2D time-periodic flows has a number of important consequences. First, it means that the Lagrangian transport is governed by essentially Hamiltonian mechanisms and can therefore be investigated using results, methods and concepts from Hamiltonian systems. Second, it enables investigation of 3D scalar transport in terms of the evolution of the scalar distribution in consecutive axial cross-sections. Finally, it enables (at least) qualitative representation of 3D transport in inline mixing flows by that in 2D time-periodic flows. (Direct quantitative correspondence exists only in case of uniform axial flow.) These approaches have found widespread and successful application for the modeling and analysis of inline mixers and heat exchangers (Byrde and Sawley, 1999; Chagny et al., 2000; Gorodetskyi et al., 2014; Lester et al., 2009; Meleshko et al., 1999; Metcalfe et al., 2006; Ottino, 1989; Singh et al., 2008; Speetjens et al., 2006, 2014). However, transport analyses of inline mixing flows to date concern primarily computational studies. In-depth experimental studies, on the other hand, remain scarce. This motivates the strong focus of the present study on experimental analyses.

1.5. RESEARCH OBJECTIVES

Better understanding scalar transport in industrial inline mixing flows is crucial for further technological advancement. To this end, deeper insight into the underlying fundamental transport mechanisms is necessary. However, studies so far on scalar transport in laminar flows are mainly computational. Experimental studies on inline-mixing flows, in contrast, are relatively rare and so far restricted to simplified configurations and/or visualization of

1

local mixing patterns or integral quantities as e.g. pressure drop and heat-transfer coeffi-
cients. This motivates the present study, which has as principal aims:

- development and realization of dedicated laboratory set-ups for experimental stud-
  ies on scalar transport in 2D time-periodic flows and 3D steady inline flows;

- direct measurement of global 3D flow fields, Lagrangian transport and the evolution
  of Eulerian concentration fields in a realistic mixer geometry (i.e. the Quatro mixer);

- experimental investigation of the interplay between (chaotic) advection and diffu-
  sion in scalar transport in two representative case studies: the RAM and the Quatro
  mixer;

- comparative analysis of the measured transport properties of the two representative
  case studies with predictions by theoretical models and numerical simulations.

The experimental studies will employ state-of-the-art measurement techniques. Nu-
merical simulations will employ both in-house and commercial CFD packages. Post-
processing and analysis of experimental and computational data will employ dedicated
software. These methods are elaborated in the respective discussions of the analyses.

1.6. THESIS OUTLINE

This thesis is organized as follows. Chapter 2 gives an overview of the experimental facil-
ities and techniques developed and employed in the current research. In Chapter 3, the
entire Hamiltonian progression of the Lagrangian dynamics from integrable to chaotic
state are visualized and investigated experimentally in a 2D time-periodic representation
of the RAM and compared with numerical simulations. Chapter 4 expands on the analysis
in Chapter 3 by a comparative experimental-computational study on scalar transport in
the 2D time-periodic RAM. This is investigated for the purely advective limit and a typ-
ical advective-diffusive case. Chapter 5, in turn, expands on Chapter 4 by presenting a
parametric study on advective-diffusive scalar transport in the 2D time-periodic RAM as
a function of geometrical and temporal parameters. This again involves a comparative
experimental-computational analysis. Chapter 6 discusses an experimental analysis on
the 3D flow field and resulting scalar transport in the Quatro mixer. The scalar transport
is investigated via visualization and measurement of the 3D concentration distribution of
a tracer substance that results from typical industrial inlet conditions. This enables de-
tailed determination of the downstream evolution of cross-sectional scalar fields, which
are compared with numerical simulations. The study ends with conclusions and recom-
mendations in Chapter 7.

Important to note is that this thesis is written such that each of the following chapters
(except Chapter 2, where experimental facilities and techniques are reported) is largely in
a self-contained form. Hence, the specific mathematical models and numerical methods
as well as experimental details relevant to the topic in question will be treated separately
within each chapter. The above discussion serves as a general introduction to these topic-
wise expositions. This may in some instances give some repetition and overlap.

2

EXPERIMENTAL FACILITIES AND METHODS

2.1. Introduction

The first experimental studies on laminar mixing and chaotic advection were performed for 2D time-periodic flows. This concerned highly-idealized geometries such as the lid-driven cavity (Chien et al., 1986; Leong and Ottino, 1989), the journal-bearing flow (Chaiken et al., 1986; Swanson and Ottino, 1990), the two-stirrer flow (modeling Aref's blinking vortex flow) (Jana et al., 1994a) and the baffled-cavity flow (Jana et al., 1994b). In these studies the evolution and advection of a blob or a line of (fluorescent) dye was monitored. This enabled visualization and qualitative validation of chaotic dynamics in 2D time-periodic flows. Following studies also primarily relied on dye advection and investigated important (quantitative) aspects as e.g. emergence of persistent patterns, stretching fields, mixing rates and effect of no-slip walls (Gouillart et al., 2007, 2008; Rothstein et al., 1999; Voth et al., 2002, 2003).

Experimental studies specifically on 3D steady inline mixing flows are scarce and largely concern dye visualization and/or measurement of either integral or local quantities as e.g. pressure drop, residence time distributions, mean heat-transfer coefficients and wall shear stress Avalosse and Crochet (1997); Hirech et al. (2003); Jaffer and Wood (1998); Kusch and Ottino (1992); Li and Fasol (1997); Metcalfe et al. (2006); Yang (2007). The first quantitative global measurements are the experiments on 3D flow and streamline patterns in the Quatro mixer in Jilisen et al. (2013). Experimental studies on other 3D steady flows include visualization of coherent structures in planar cross-sections by (fluorescent) dye (Arratia et al., 2005; Fountain et al., 1998, 2000; Shinbrot et al., 2001; Sotiropoulos et al., 2002) and measurement of the corresponding planar velocity using particle image velocimetry (PIV) (Fountain et al., 2000).

Experimental transport analyses under 3D unsteady conditions concern measurement of flow, Lagrangian trajectories and coherent structures in a variety of 3D time-periodic flows (Cheng and Diez, 2011; Miles et al., 1995; Otto et al., 2008; Speetjens et al., 2004; Wu et al., 2014; Znaien et al., 2012). The common denominator in these studies is employment of 3D particle tracking velocimetry (3D PTV), an advanced technique for measurement of 3D velocity fields and Lagrangian trajectories. This technique will also be utilized in the current study.

The experimental analyses of the two case studies in the current investigation, viz. the 2D time-periodic representation of the RAM and the 3D Quatro mixer, will employ (advanced) versions of the measurement techniques utilized in the above-mentioned literature. The 2D time-periodic RAM is investigated using PIV for the velocity field and tracer particles for the Lagrangian transport. Scalar transport is studied by dye visualization (purely advective limit) and measurement of evolving temperature fields (advective-diffusive transport) using infrared thermography (IRT). The 3D Quatro is investigated using 3D PTV for flow and streamline measurements and 3D Laser-Induced-Fluorescence (3D LIF) for visualization and analysis of 3D fluorescent dye distributions. The corresponding laboratory facilities and measurement techniques are discussed in detail below.

2.2. TIME-PERIODIC 2D RAM FACILITY

Fig. 2.1 shows a schematic of the laboratory setup for the 2D time-periodic representation of the 3D RAM in Fig. 1.2. Basically, the 3D cylindrical geometry is reduced to a 2D cross-sectional (circular) area, which simplifies experimental analysis considerably (easy visual access for temperature measurements and relatively simple optical flow measurements). The setup is composed of a test section which is a shallow circular tank (with an effective depth of 0.01 m and a radius of 0.25 m) with systematically oriented apertures on the circumference. Only two apertures are shown in the figure, yet there are two more configurations with four and five apertures. Here, the test section represents the inner cross-sectional area of the RAM, whereas the circumference with the apertures imitates the stationary inner cylinder. A computer controlled, motor-driven belt system (Maxon Motor-Gear-Sensor combination with a stability of 0.07 % at 675 rpm, which corresponds to a belt velocity of 0.005 m/s) is positioned on the apertures and it reproduces the motion of the rotating outer cylinder. The elastic belts are gently pressed against the apertures from the outside so as to seal-off the flow domain. Note that the belts (the height of the belts h_b = 18 mm) are larger than the apertures (the height of the apertures h_a = 10 mm) so as to ensure that they follow the curvature of the circular boundary upon being pressed against it from the outside.
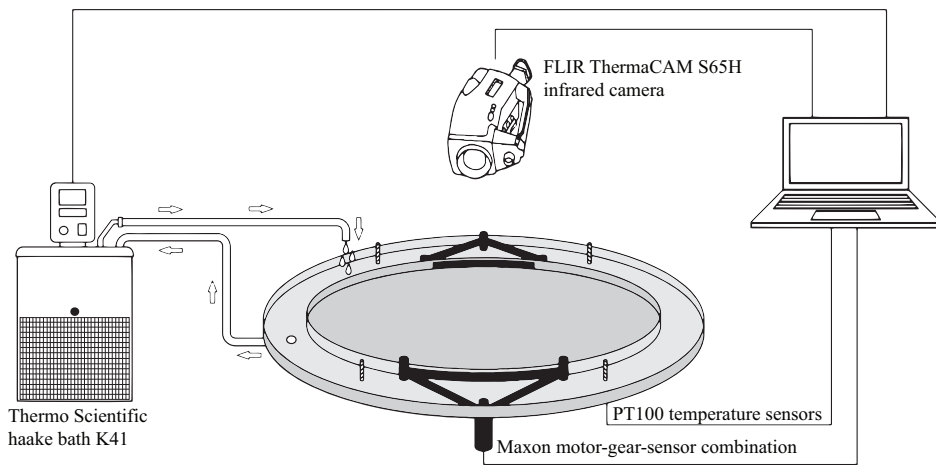
Figure 2.1: A schematic sketch of the 2D RAM facility: a circular test section (dark gray) enclosed by an external annular reservoir (light gray) holding motor–belt systems (black) and PT100 temperature sensors. A Haake bath, locations of the temperature sensors, two Maxon motor–gear–sensor combinations, and an infrared camera are schematically indicated. For flow and scalar field experiments at isothermal conditions, the infrared camera is replaced by a MegaPlus ES2020 CCD camera or type Pike F145B (Allied Vision Technology) CCD camera.

The test section is filled with layers of two immiscible fluids: a silicon oil layer with a depth of 0.005 m at the top, and a glycerol–water solution with the same depth of 0.005 m at the bottom. The particular silicon oil of interest is one with a kinematic viscosity of v = 0.01 m^2/s and thermal diffusivity of α = 10^{-7} m^2/s (AK10000, Wacker GmbH, Ger-

many). The density of silicon oil (970 kg/m^3) is smaller than the density of the glycerol–water solution (1186 kg/m^3) so that the silicon oil layer always remains at the top throughout the experiment. The low viscosity of the glycerol–water solution (1.745 ×10^{-5}m^2/s) reduces the viscous effects from the bottom surface of the tank on the motion of the top-layer fluid.

In the actual RAM, there is only one aperture at an axial location and progressing along the axis of the RAM the azimuthal location of the aperture changes by an offset angle Θ (Fig.1.2). This results in a systematic reorientation of the flow and it is reflected in the experimental facility via the sequential actuation of the motor–belt system. This generates a time-periodic piece-wise steady flow field in the test section.

Non-isothermal experiments

Non-isothermal (i.e., temperature field) experiments require the use of complimentary equipment, viz. a hot water reservoir, a Haake bath, temperature sensors and an infrared camera (Figure 2.1). The annular hot water reservoir enclosing the test section serves for keeping the temperature of the circumference constant by circulating water between the reservoir and the Haake bath (Thermo Scientific Haake Bath K41). The reservoir also accommodates the motor-driven belt system and the temperature sensors (PT100 with a relative accuracy of 0.01 °C, calibrated in TempControl Company in The Hague, The Netherlands) controlling the temperature of the water. The circulating water that is preheated to the desired temperature of 35 °C in the Haake bath is sent to the hot-water reservoir just before the initialization of the experiment. The sensors immediately start to check the temperature of the water in the reservoir. In general, once the equilibrium is reached in the circulation system (the heat added to the circulating water by the Haake bath is equal to the heat loss from the water during circulation), the temperature of the water in the reservoir only changes within the accuracy of the Haake bath (0.05 °C). In the case that the temperature drops below (or rises above) a predefined threshold (here 35±0.1 °C), a signal is sent to the Haake bath to increase (or decrease) the temperature of the water inside. This ensures a uniform and constant temperature throughout the circular wall of the test section. The wall is made of aluminum with a thermal conductivity of 205 W/mK whereas the belts are made of steel cords (k_{steel} = 43 W/mK) that run helically in the polyurethane belt ($k_{polyurethane}$ = 0.65 W/mK) and have a lower conductivity than aluminum. This situation causes an average temperature difference of 0.65 °C between the belt and the wall, hence, the total heat transfer from the wall to the fluid is reduced in the experiments compared to numerical simulations which assumes a uniform temperature distribution at the wall.

2.2.1. Validity as physical model

Effect of temperature-dependent material properties

For the sake of simplicity in the 2D numerical simulations (a finite element method (FEM) is used in Comsol Multiphysics 4.3b for the simulations) it is assumed that the material properties do not vary with temperature to preclude the coupling between the momentum and energy equations (Eq.(4.5) and Eq.(6.2), respectively) so as to increase computational efficiency. This means that effects of temperature-dependent material properties

are neglected, an assumption which should be tested. In practice, the viscosity of the silicone oil used in the experiments in the temperature range of 20–35 °C changes by 17 % (see Wacker (2002)). In order to estimate the effect of non-constant viscosity on the flow field, a temperature-dependent function is defined for the viscosity. Subsequently, a simulation with a mesh of 40000 elements have been performed for 100 periods, which is computationally expensive due to inherently coupled momentum and energy equations (temperature-dependent material properties necessitate the re-calculation of Eq.(4.5) at each time step, the flow field changes accordingly and, in turn, affects the temperature field distribution). To stay in reasonable computational limits, a mesh with relatively low resolution is used to check the effect of buoyancy. To evaluate the deviation from the constant-viscosity case a deviation parameter is defined as

$$\delta_{\|\boldsymbol{u}^*\|} = \frac{\sqrt{\frac{1}{M} \sum_{i=1}^{M} \left(\|\boldsymbol{u}(x_i, y_i)\| - \|\boldsymbol{u}^*(x_i, y_i)\| \right)^2}}{\langle \|\boldsymbol{u}\| \rangle} \tag{2.1}$$

where M is the total number of data points in the numerical domain, $\boldsymbol{u}(x, y)$ the reference constant-viscosity flow field and $\boldsymbol{u}^*(x, y)$ the flow field with non-constant viscosity. $\langle \|\boldsymbol{u}\| \rangle$ stands for the average velocity, which is calculated by the integration of velocity magnitude on the surface normalized by the surface area. Figure 2.2 (left) shows that the deviation of the normalized velocity difference $\delta_{\|\boldsymbol{u}^*\|}$ has its largest values during the first periods after starting the numerical experiment (a maximum is found in the 3rd period) and reduces dramatically as the number of periods increases. The error is defined as $\varepsilon = |\|\boldsymbol{u}\| - \|\boldsymbol{u}^*\||$ and represented per histogram for the 3rd period in Figure 2.2 (right), which shows that the difference is mostly smaller than 0.1 %. We can therefore conclude that the effect of a temperature dependent viscosity can safely be ignored in the current study.
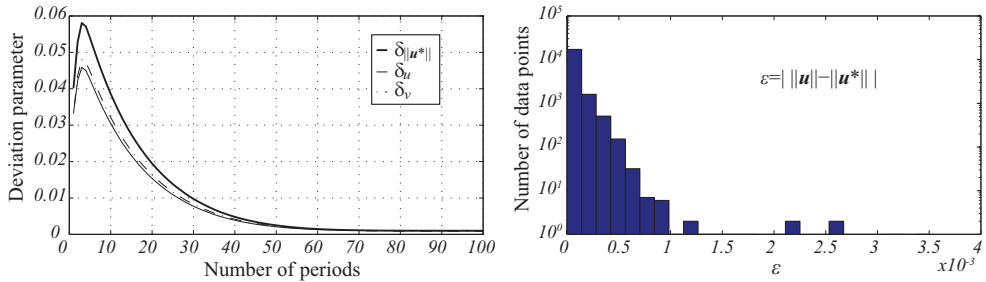
Figure 2.2: Deviation of velocity magnitude, $\delta_{\|\boldsymbol{u}^*\|}$, velocity component in the x-direction, δ_u, and in the y-direction, δ_v, for 100 periods (left). The histogram gives the distribution of the error, ε, in velocity magnitude for the period where the deviation is maximum (right).

EFFECT OF THREE-DIMENSIONALITY

In order to check the assumption of two-dimensionality of the flow field of the top layer, a 3D numerical simulation mimicking the experimental settings and flow characteristics (see Figure 2.3) is performed with Comsol 4.3b Multiphysics software. The computational

domain is divided into two layers as in the experiments. A tangentially moving wall condition is used at the location of the aperture and a zero-velocity condition is applied for the remaining part of the circumference (both representing no-slip boundary conditions). To avoid singularities at the corners of the aperture, the change between zero and constant azimuthal velocity at the boundary is smoothed by replacing the step function by a continuous function for the azimuthal velocity. The no-slip boundary condition is applied at the bottom surface of the tank and a stress-free condition is applied at the top surface (assuming that the surrounding air does not exert a force on the silicon oil in the top layer). At the interface we apply a dynamic boundary condition which means that the shear and normal stresses are continuous over the internal interface: $\rho_t \nu_t \frac{\partial \mathbf{u}_{H,t}}{\partial z} = \rho_b \nu_b \frac{\partial \mathbf{u}_{H,b}}{\partial z}$, with $\mathbf{u}_H = (u, v)$ the horizontal velocity components in top (t) and bottom (b) fluid layers, and $\rho_t \nu_t \frac{\partial \mathbf{u}_{V,t}}{\partial z} = \rho_b \nu_b \frac{\partial \mathbf{u}_{V,b}}{\partial z}$ with $\mathbf{u}_V = w$ for the vertical velocity component. Deformation of the interface and the free surface (implying baroclinic vorticity production) are weak as in previous studies by Akkermans et al. (2008, 2010), where the dynamics of dipolar structures in single and two-layer fluids have been investigated, and are therefore ignored. The 3D computational domain is discretized with 915000 mesh elements. The Navier-Stokes equation governing the simulations is given by Eq.(6.1) in Section 4.2.1. In order to obtain a quantitative measure for the importance of the 3D effects in the flow field of the top-layer fluid, the ratio of the kinetic energy contained in the vertical motion $E_{k,V}$ to that in the horizontal motion $E_{k,H}$ is calculated at the mid-plane of the top layer (see Akkermans et al. (2010)), where $E_{k,V}$ has its maximum value. The ratio is defined as

$$\frac{E_{k,V}}{E_{k,H}} = \frac{2 \int\int w^2 dx dy}{\int\int (u^2 + v^2) dx dy},$$

(2.2)

This ratio turned out to have the value of 3.2×10^{-5} and with this value we can safely conclude that the flow in the top layer is sufficiently close to 2D (with possibly a weak vertical variation of the horizontal velocity components) for our purpose.
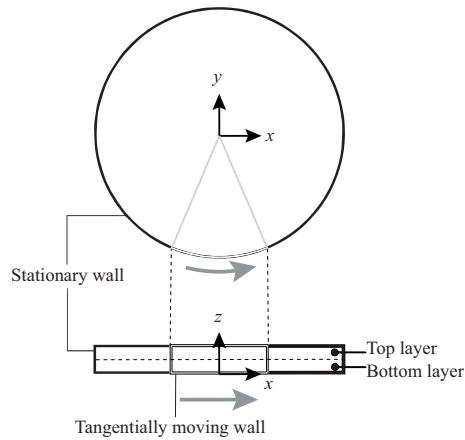
Figure 2.3: Schematic top and side views of the 3D computational domain used for the two-layer simulations. The dashed line indicates the (non-deformable) interface.

EFFECT OF SURFACE HEAT LOSS

The fluid inside the test section has a free surface which causes heat loss that cannot be eliminated by a different setup design, since two-dimensionality and optical accessibility require a free and accessible top surface. However, we can reduce the heat loss from the free surface by using a lid transparent for the infrared camera above the fluid–air interface without touching the fluid. This will strongly decouple the two-layer fluid system from the free atmosphere. The surface heat loss can be estimated by an approach described below. The main conclusion is that we can control thermal heat losses at the free surface fairly well during the early stages of the experiment, but heat losses at the free surface start to become significant compared to the heat transfer from the side wall reservoir into the fluid layers after a certain time.

The heat transfer Q_{sw} from the heat reservoir to the fluid via the stationary wall by conduction is

$$Q_{sw} = k_f A_{sw} \frac{\partial T_1(r, t)}{\partial r}\Big|_{\Gamma}, \tag{2.3}$$

where k_f is the thermal conductivity of the fluid, A_{sw} the contact surface area between fluid and the stationary part of the circular side wall. The temperature gradient at the boundary can be estimated by using the analytical solution of the axisymmetric 2D diffusion equation $T_1(r, t)$. Typical values for Q_{sw} are shown in Figure 2.4. The estimation of the heat transfer Q_{mw} from the heat reservoir to the fluid via the moving side wall (thus representing the effect of convection) is based on the time period T_f that a fluid particle stays in contact with the moving side wall, i.e. $T_f = R\Delta/U$. Then, the heat transfer Q_{mw} can be written as

$$Q_{mw} = k_f h_f \int_0^{T_f} \frac{\partial T_1(r, t)}{\partial r}\Big|_{\Gamma} U dt, \tag{2.4}$$

where h_f is the depth of the fluid (the constant value is also indicated in Figure 2.4). The sum of Q_{sw} and Q_{mw} gives a reasonable estimate of the total heat transfer Q_w from the reservoir to the fluid.

Figure 2.4: Typical values of Q_{sw} and Q_{mw} for the first ten periods.

The heat transfer in the air gap between the lid covering the test section and the fluid

can be approximated by considering it as a Rayleigh-Bénard cell. It turns out that the associated Rayleigh number is smaller than the critical number so that the heat release to the air (and subseq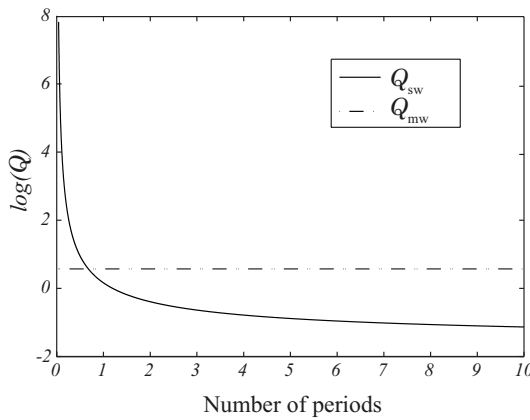uent transport through the top lid to the free atmosphere) is dominated by diffusion (see Kundu and Cohen (1990)). Based on the total energy input $E_{in} = \int Q_w dt$ an equivalent axisymmetric temperature profile is defined for the surface via $T_1(r, t)$. By using the analytical solution of the 1D diffusion equation in axial direction $T_2(r, z, t)$ (in the air gap, with $T_2(r, z = 0, t) = T_1(r, t)$) with inhomogeneous boundary conditions in radial direction at $z = 0$ the heat loss Q_s can be estimated by

$$Q_s = k_{air} \int_0^R \frac{\partial T_2(r, z, t)}{\partial z}\Big|_{z=0} 2\pi r \, dr. \tag{2.5}$$

The evaluation of the ratio Q_s/Q_w for the first ten periods gives a maximum of 25 %, i.e. 25 % of the heat transferred from the wall to the fluid is eventually released to the air. In our view this explains why the comparison in Section 4.3.2 later on should be restricted to a few periods only. Under this condition it can thus be concluded that the experimental analysis discussed in Section 4.3.2 can be based on thermal boundary conditions that sufficiently correspond to the 2D configuration.

2.3. STEADY 3D QUATRO MIXER FACILITY

Two separate laboratory setups have been constructed for experimental analyses of the Quatro mixer shown in Fig. 1.3: the first setup for measurement of flow, streamlines and Lagrangian transport by way of 3D PTV; the second setup for visualization and measurement of scalar transport by way of 3D LIF. The main structure and the working principle of both facilities are the same. The main difference is that they are equipped with different data acquisition systems.

The design of the first Quatro mixer facility is based on the implementation of 3D particle tracking velocimetry (3D PTV) (see Jilisen (2011)). The facility, which is shown in Fig. 2.5 (left panel), is a closed-loop system that recirculates the working fluid. It comprises an optically-accessible test section: transparent replicas of the Quatro mixer elements (perspex; thickness 1.5 mm) that closely fit into a glass circular cylinder (inner diameter $D = 56$ mm and thickness $a = 2$ mm), which is called the mixer model, and a glass rectangular viewing box ($200 \times 200 \times 200$ mm) enclosing the model. Placement of the mixer model inside the box, which is filled with the same material as the working fluid, reduces internal refractions (see Budwig (1994) and Jilisen et al. (2013)). The test section is placed vertically between two reservoirs so as to use the pressure gradient as the driving force for a continuous throughflow. The top reservoir is connected to the test section via an entrance tube ($D_{et} = 56$ mm) which accommodates a flow straightener at the inlet. The fluid leaving the test section passes through a rotameter (which monitors the flow) and a valve (which regulates the flow), then accumulates in the bottom reservoir. A pump connected to the bottom reservoir continuously feeds the inner part of the top reservoir. The flow rate of the pump is higher than the flow rate of the throughflow, so that the inner part overflows. This keeps the pressure head and, consequently, the flow rate constant and assures a steady continuous flow inside the facility. Overflowing fluid returns back to the bottom reservoir through an overflow tube. The work presented in Jilisen (2011) and Jilisen et al.

(2013) uses water as the working fluid (with a flow rate $\dot{Q} = 80$ L/h and a mean axial velocity $U_{mean} = 9$ mm/s), which results in a Reynolds number $Re = U_{mean}D/\nu = 505$ (kinematic viscosity $\nu_{water} = 10^{-6}$ m^2/s). Afterwards, in the work by Rajaei (2013), water is replaced with silicone oil (with a density $\rho = 970$ kg/m^3 and a kinematic viscosity $\nu = 10^{-4}$ m^2/s) and the Reynolds number is lowered to 3.5 ($\dot{Q} = 56$ L/h and $U_{mean} = 6.3$ mm/s).
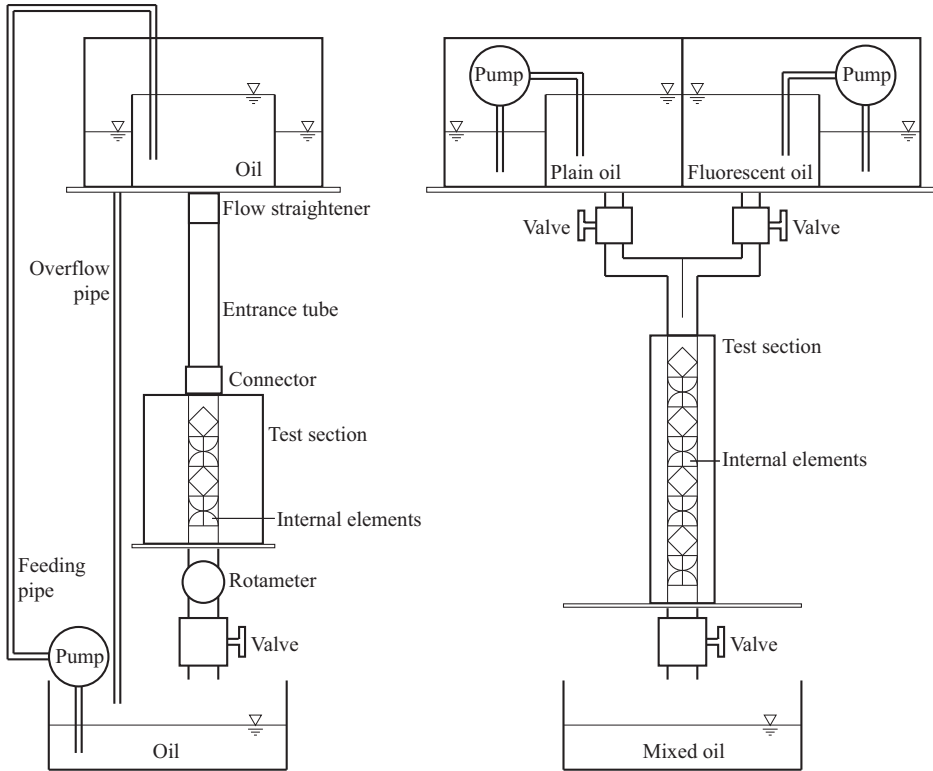
Figure 2.5: A schematic sketch of the Quatro mixer facilities: the left and the right figures show the setups used for 3D PTV and 3D LIF measurements, respectively. Both facilities accommodate a transparent test section with a pressure-driven flow inside, reservoirs and connecting tubes.

The second Quatro mixer facility, which is shown in Fig. 2.5 (right), is designed for 3D LIF measurements. Unlike the first facility, it is an open-loop system that uses both plain and fluorescent silicone oils (with a density $\rho = 970$ kg/m^3 and a kinematic viscosity $\nu = 10^{-4}$ m^2/s) as the working fluid. It possesses two top reservoirs which hold plain oil and fluorescent oil separately and a bottom reservoir which stores the mixed oil. As in the former facility, the top reservoirs are divided into two parts to keep the flow rate constant inside the facility. The test section of this facility is made of the same materials (the viewing box and the tube are glass and the mixing elements are perspex), however it is longer (the length is 1 m) than the one of the former facility so as to accommodate more mixing elements and narrower (the cross-sectional area of the viewing box is a square with a side length of 100 mm). Having a narrower viewing box does not have any effect on the optical quality but significantly decreases the amount of liquid that is needed to fill it.

2.4. EXPERIMENTAL METHODS

The main purpose of the experiments in the simplified RAM facility and the Quatro mixer facilities is the investigation of the flow and scalar patterns under the action of time-periodic and spatially-periodic flow fields. Both facilities, through their optically-accessible test sections, allow the use of non-intrusive measurement techniques. The flow field, temperature field and passive scalar field in the simplified RAM mixer are investigated via particle image velocimetry (PIV), infrared thermography (IRT), dye visualization and particle position detection experiments. The Quatro mixer facilities, on the other hand, are equipped with a 3D particle tracking and a 3D laser induced fluorescence system. The details of the experimental procedures are presented in this section.

2.4.1. PARTICLE IMAGE VELOCIMETRY

For the PIV measurements polystyrene foam particles (with a density $\rho_p = 500$ kg/m^3 and a diameter $d_p = 1.5$ mm, respectively) floating on the free surface of the top layer (silicone oil) were used as tracer particles. Typical response time of particles, which is a measure of the difference between particle and local fluid velocity, was estimated as $T_p = d_p{}^2\rho_p/(18\rho_f\nu_f) = 6.4$ μs, which is negligible compared to the typical flow time scale $T_a = R/U = 62.5$ s (see Raffel et al. (1998)). In other words, the particle Stokes number being $St = T_p/T_a \ll 1$ and the tracer particles were passively advected by the flow. The test section was illuminated by ambient light which suffices for visualization purposes due to relatively low velocities of the tracer particles (typically $u_{max} = 9$ pixels/s). During the PIV measurements, 12-bit images were captured by a MegaPlus ES2020 CCD camera placed above the test section with a resolution of 1600×1200 pixels. A field of view of 500 mm $\times$ 500 mm was captured with a magnification factor of approximately 0.02 at a digital resolution of 2.3 pixels/mm. PIVview 3C Version 2.4 software was used for post-processing. Images of tracer particles were interrogated using windows of final size 24×24 pixels with an overlap factor of 50 % resulting in a vector spacing of about 5 mm in each direction.

The main uncertainty source in the flow field measurements was the uncertainty in the determination of the particle image displacement and was determined by the magnification factor, non-uniformity in particle distribution, mis-matching error and sub-pixel analysis (see Nishio and Murata (2003); Okamoto et al. (2000)). An estimation based on these error sources gives an uncertainty of 9×10^{-5} m in displacement and corresponding to an uncertainty of 1.8×10^{-4} m/s in velocity (the time between two consecutive images was 0.5 s). When normalized with the maximum velocity in the flow field (which is the velocity of the belt), the relative error is approximately 4 %.

2.4.2. INFRARED THERMOGRAPHY

The infrared thermography measurements were performed with a FLIR ThermaCAM S65H imaging system, operating in 7.5–13 μm spectral range (see ThermaCAM^{TM} (2006)). The infrared camera was placed above the test section and measured the infrared radiation from the top surface of silicon oil. In order to reduce heat losses from the surface of the fluid to the surrounding ambient air, a lid made of polyethylene PE is placed on the top

of the test section. The lid is assumed to be at room temperature (20 °C) for the calculation of the corrected temperature distribution. Based on the transmission curve of PE (which is almost constant within 7.5–13 μm spectral range), the graybody emittence of silicone oil and the Planck's law for blackbody emittance, the infrared camera signal is converted to the surface temperature (see ThermaCAM$^{\text{TM}}$ (2006)). In the range of 20–35 °C the corrected values are found to be linearly dependent on the uncorrected readings. Measurement accuracy was specified as ±2 °C or ±2 % in the User's Manual of the manufacturer (see ThermaCAM$^{\text{TM}}$ (2006)), but comparison with a PT100 temperature probe showed an even better accuracy for our application, namely ±0.5 °C.

2.4.3. Dye visualization

Dye visualization is employed for experimental transport studies in the limit of infinite-Pe by replacing the temperature field, which is the diffusive scalar field of the finite-Pe experiments, by a non-diffusive scalar field. For creation of the initial conditions, the tank is divided into two regions by placing a cylindrical tube concentrically in the circular tank. The radius R_{in} of the tube is chosen such that the inner and outer regions of the tube have the same area, thus $R_{\text{in}} = \sqrt{2}R/2$. The inner region of the tube is filled with silicone oil colored by white dye whereas the outer region is colored by black dye, which, after the removal of the cylindrical tube, serves as the initial condition for infinite-Pe experiments. The evolution of the scalar patterns in time is captured by an AVT Pike F145B CCD camera placed above the test section. The 12-bit gray scale images have a resolution of 1388 × 1038 pixels and can distinguish $2^{12} = 4096$ gray levels.

2.4.4. 3D particle tracking velocimetry

For 3D PTV experiments, two arrays of light-emitting diodes (LEDs, LUXEON Rebel Color, Philips, The Netherlands) with an intensity peak at 530 nm wavelength are used for the illumination of the flow with fluorescent seeding particles [polymethylmethacrylate (PMMA) hollow sphere particles doped with rhodamine-B; $d_{\text{p}} = 50$ μm, $\rho_{\text{p}} = 1190$ kg/m^3; Microparticles GmbH, Germany] (Jilisen et al., 2013). The particles have an absorption and an emission peak at $\lambda_{\text{ab}} = 560$ nm (green) and $\lambda_{\text{em}} = 585$ nm (red), respectively. This enables the elimination of the reflections due to fluid–wall interfaces and small air bubbles, which deteriorates the image quality otherwise, by two-step optical filtering: cyan dichroic filters are mounted on the collimator lenses of the LEDs to exclude the LED contributions above $\lambda = 570$ nm that may interfere with the fluorescence and 590 nm high-pass filters (type OG-590, Schott Glass, Germany) are mounted on camera lenses to remove the reflections (around the LED peak) from the test section. The slight mismatch between the emission wavelength of the particles and the cut-off wavelength of the high-pass filter does not cause significant reduction in light intensity due to broad emission wavelength of the particles.

The typical response time of the particles to changes in velocity field is estimated as $T_{\text{p}} = d_{\text{p}}^2 \rho_{\text{p}}/(18\rho_{\text{f}}\nu_{\text{f}}) = 1.7$ μs, which is negligible compared to the typical flow time scale T_{a}, where $T_{\text{a}} = D/U_{\text{mean}} = 56$ s (Raffel et al., 1998). In other words, the particle Stokes number is $St = T_{\text{p}}/T_{\text{a}} \ll 1$, meaning that the tracer particles are passively advected by the flow. The drift velocity due to buoyancy $U_{\text{p}} = |\rho - \rho_{\text{p}}|gd_{\text{p}}^2/(18\rho_{\text{f}}\nu_{\text{f}}) = 3.1$ μm/s is much less

than the fluid velocity $U_{mean} = 1$ mm/s and may cause a deviation in particle trajectory, i.e. $\Delta x_p \equiv U_p T_a \sim 0.2$ mm, during its residence within the test section. This is also considered negligible in the present work.

Four synchronized 12 bit CCD cameras (with a resolution of 1600×1200 pixels; MegaPlus ES2020, Kodak, United Kingdom) equipped with 50 mm lenses (type NMV-50M1, Navitar, USA) are positioned and aligned in such a way that each camera views the test section from a different perspective. This configuration provides an efficient matching performance for the 3D PTV algorithm. Camera control, synchronization and data storage are achieved by a data acquisition system (DVCR5000, Iris Vision, The Netherlands) (Jilisen et al., 2013).

This study uses the non-commercial 3D PTV algorithm developed at ETH Zurich, Switzerland (Lüthi et al., 2005; Willneff, 2003), which can handle the refractions due to medium change at two interfaces (i.e. the interfaces between ambient/working fluid and the viewing box wall) and is capable of performing particle matching and trajectory construction based on four camera configuration. The calibration procedure is explained in Section 2.4.4.

In the previous study by Jilisen et al. (2013) the error in measurements is found to be around 10–15 %. In the present study, the error is reduced significantly by a new method comprising a modification procedure in calibration and a correction procedure in post-processing of data. Details are given below.

MODIFICATION IN CALIBRATION

The current study employs the ETH algorithm for the detection of the particle position and the reconstruction of the particle trajectories, which assumes that there is a flat wall with two different media at the both sides (i.e. cubic viewing box). However, in the present experimental facility the existence of the cylindrical wall of the model mixer and the mixing elements introduces more complexities than a cubic viewing box does.

To calculate the particle positions more accurately, the calibration procedure is accomplished in two steps. In the first step, a calibration body is placed inside the test section that is filled with the working fluid and the camera images are processed by the ETH algorithm to compute the view angles and the positions of the four cameras. In the second step, by taking into account the refraction effects due to the curved wall (which can not be handled by the ETH algorithm), synthetic particle images (with 5000 particles) are generated by an in-house developed C code based on the configuration of the cameras (i.e. the view angles and the positions of the cameras) and Snell's law. Then, the positions of the particles in the synthetic images are calculated by the ETH algorithm.

Figure 2.6 depicts the exact (generated by the C code) and calculated (by the ETH algorithm) positions of the particles inside the tube. It shows that the maximum error occurs in close proximity of the tubular walls. Hence, to compensate the error due to the existence of the tubular wall the following coefficients are introduced:

$$y_{cor} = \begin{cases} y\left(1 - \frac{1}{R}\right), & \text{for } y \geq 0 \\ y\left(1 - \frac{0.68}{R}\right), & \text{for } y < 0 \end{cases} \tag{2.6}$$

where R is the radius of the tube and y_{cor} is the y-component of the corrected particle positions. This improves the calculation of the particle positions compared the previous

work by Jilisen et al. (2013) and the effect of the correction on the processed data (i.e. velocities) is discussed in Section 2.4.4.
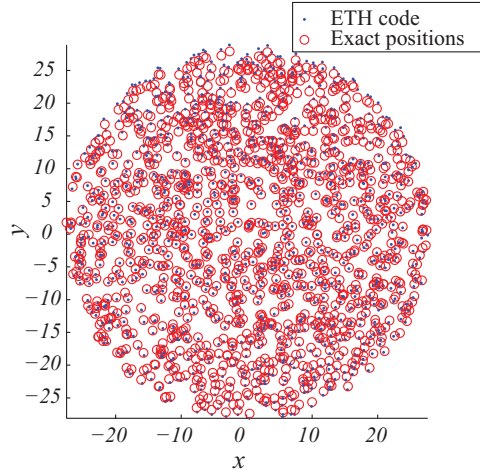
Figure 2.6: Deviations in particle positions due to the curved wall of the model mixer. The circles (∘) demonstrate the (exact) positions of the particles synthetic images of which is generated by the C code, whereas the dots (·) indicate the calculated positions of the particles from the synthetic images by the ETH algorithm.

LOW-PASS FILTERING FOR PARTICLE TRAJECTORIES

In order to eliminate the random error in the position data (which may result in very high error in the velocity field otherwise, since the velocity field is determined through central differencing), a moving cubic spline filter, see Lüthi et al. (2005), has been utilized. The velocity is then defined as the first derivative of the cubic spline.

In this method, a cubic polynomial is fitted for each time step t using ten preceding and subsequent time steps, from $t - 10 \cdot \triangle t$ to $t + 10 \cdot \triangle t$. $x_i(t)$ represents raw position signal of a point at time t in i direction and it is expressed as;

$$x_i(t) = c_{i,0} + c_{i,1} t + c_{i,2} t^2 + c_{i,3} t^3 + \epsilon(t) \tag{2.7}$$

where $\epsilon(t)$ is the noise. The constants c_i are determined as

$$c_i = (A^T x_i)(A^T A)^{-1} \tag{2.8}$$

where

$$A = \begin{pmatrix} 1 & (t-10\Delta t) & (t-10\Delta t)^2 & (t-10\Delta t)^3 \\ 1 & (t-9\Delta t) & (t-9\Delta t)^2 & (t-9\Delta t)^3 \\ \vdots & \vdots & \vdots & \vdots \\ 1 & (t+10\Delta t) & (t+10\Delta t)^2 & (t+10\Delta t)^3 \end{pmatrix}$$

and

$$c_i = \begin{pmatrix} c_{i,0} \\ c_{i,1} \\ c_{i,2} \\ c_{i,3} \end{pmatrix}.$$

Position and velocity after filtering are expressed as;

$$x_i(t) = c_{i,0} + c_{i,1}t + c_{i,2}t^2 + c_{i,3}t^3, \tag{2.9}$$

$$u_i(t) = c_{i,1} + 2c_{i,2}t + 3c_{i,3}t^2. \tag{2.10}$$

The reader is referred to the work by Lüthi et al. (2005) for detailed discussion on this approach.

ERROR ANALYSIS

In order to quantify the error in 3D PTV experiments, a comparative analysis between experimental and numerical velocity fields is performed for velocity components u, v and w, and magnitude $\|\boldsymbol{u}\|$, for which more than 18,000 data points are taken into account. The positions are taken from the experimental data set and to obtain the corresponding numerical values a cubic interpolation fit is employed on the simulated data. The deviations in the experimental data are quantified via $\epsilon(u) \equiv |u_n - u_e|/|u_{n,max}|$ where u can be u, v, w or $\|\boldsymbol{u}\|$ (n and e stand for numerical and experimental data, respectively). The associated statistics are given in Table 2.1. The maximum error is calculated for the velocity component in y-direction which corresponds to the depth direction of the mixer according to the camera configuration. Overall, the error is found to be between 3–7 % which implies that the modification in the calibration and the low-pass filtering in the particle tracks result in an improvement in post-processing, hence an overall good agreement between the numerical and the experimental results.

Velocity components and magnitude	σ (standard deviation)	μ (mean)	M (median)
u	3.34	0.18	0.16
v	6.76	1.21	0.24
w	3.69	0.13	0.17
$\|\boldsymbol{u}\|$	6.50	1.06	0.27

Table 2.1: Statistics of the error analysis for velocity components u, v, w and magnitude $\|\boldsymbol{u}\|$ calculated by comparing experimental and numerical velocity fields (the numbers are in percentage).

Figure 2.7 shows a sample experimental and numerical trajectory. Notwithstanding the small deviations, the trajectories show a very good agreement. The main reason for the deviation is that the position and the alignment of the mixing elements inside the tube is not perfect.

2.4.5. 3D LASER-INDUCED FLUORESCENCE

The 3D laser induced fluorescence (3D LIF) measurements are performed in a cylindrical volume with diameter $D = 56$ mm and a height of 800 mm, in which 14 mixing elements (i.e. 7 mixing periods) are hold. The measurement volume is illuminated by use of a continuous argon–ion laser (Stabilite 2016, Spectra Physics, USA) at a wavelength of 488 nm
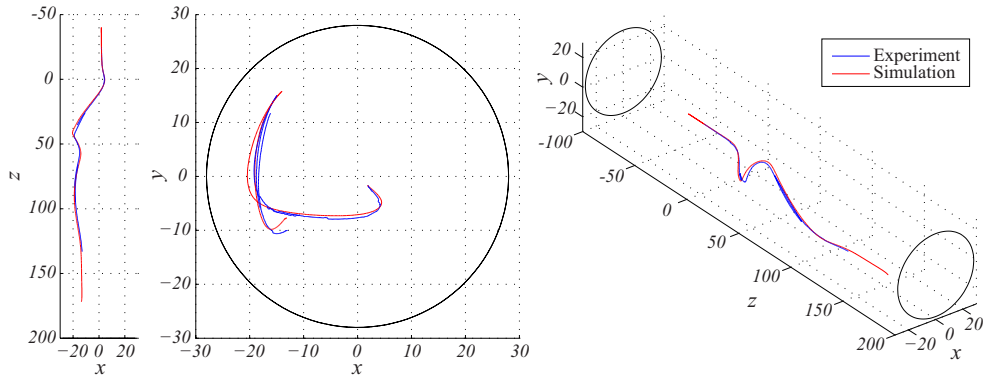
Figure 2.7: Comparison of experimentally (blue) and numerically (red) acquired particle trajectories. From left to right: side view (normal to xz-plane), top view (normal to xy-plane) and isometric view.

and a laser sheet scanner (LaVision, Germany) (see Fig. 2.8). The fluorescent oil (with a dye concentration of 40 μg/L) is a mixture of an oil-soluble fluorescent dye (Sudan Orange 183 by BASF AG, Ludwigshafen, Germany) and silicone oil , which emits light at 580 nm. This allows the visualization of the concentration field after filtering the laser wavelength by use of a 570 nm high-pass optical filter (Thorlabs, Germany). The images of the concentration fields are recorded using a high speed 12 bit CMOS camera (with a resolution of 1024 × 1024 pixels; HighSpeedStar 5.1, LaVision, Germany) with its optical axis perpendicular to the laser sheet. The camera is equipped with a lens (AF Nikkor 28–70 mm, Nikon, Japan) at a focal length of 70 mm. In order to acquire in-focus images of the scalar patterns at a relatively high signal-to-noise ratio (i.e., at $f\# = 5.6$ to have reasonable amount of light recorded during the image exposure), the measurements are repeated by focusing the camera at two different planes along the diameter of the tube. The focal plane is positioned in the middle of the near half-diameter in the first run and then it is moved to the middle of the far half-diameter for the second run. The field of view of the camera in the center plane of the tube is approximately 65 × 65 mm and in order to acquire the concentration field throughout the test section the image acquisition is repeated at 23 positions in the axial direction. This is facilitated by placing the laser sheet scanner and the camera on an L-beam carrying both devices on each side and moving upwards and downwards systematically.

The synchronization between the illumination system and high-speed imaging system is performed by a signal generator (Stanford, USA) and a high-speed controller (LaVision, Germany). The signal generator produces a TTL signal at a frequency of 0.05 Hz that is input to the laser sheet scanner, which results in a scanning period of 20 s. The high-speed camera is configured to capture images at a recording frequency of 50 Hz. The image acquisition is started by a trigger signal that is generated by the laser sheet scanner and received by the high-speed controller. This configuration brings in a total of 1000 images captured during one turn-around time of the laser scanner. Image acquisition and pre-processing are performed in Davis 7.2 (LaVision, Germany).
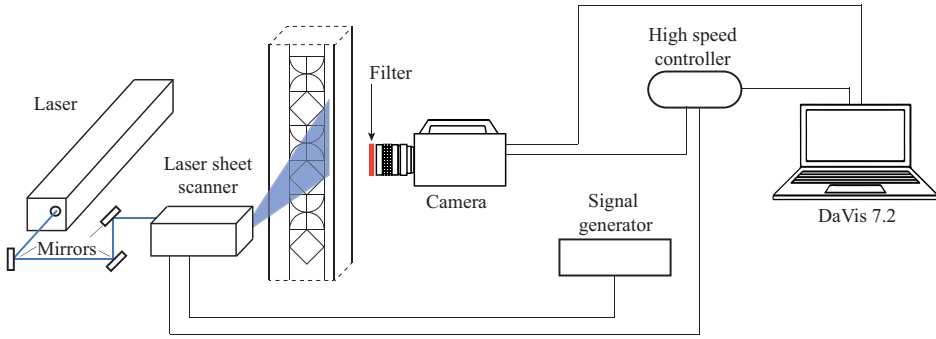
Figure 2.8: A schematic sketch of the 3D LIF data-acquisition system. The system is composed of a continuous laser equipped with a laser sheet scanner device, a high-speed camera with a multifocal lens on which a high-pass filter is mounted, a signal generator by which the laser sheet scanner is activated and a high speed controller for the synchronization of these devices.

Calibration and corrections

Considering the fact that the aim of the experiments is the (qualitative) investigation of the scalar patterns rather than a quantitative analysis, the camera readings are kept non-dimensional (not converted to any physical units) with the assumption that the camera has a linear response to fluorescence intensity. Nonetheless, for a better image quality, several corrections are applied. First, in order to improve the contrast in the concentration field, dark image calibration is performed on the raw images. This is achieved by subtracting the dark images taken in a dark room (when the camera lens is covered) from the raw images. Second, the correction images captured at uniform concentration values (by running only the fluorescent oil in the test section) are analyzed to check the effect of the attenuation of the laser on the camera readings. The data analysis shows that the attenuation due to absorption of the dye, which has a concentration of 40 μg/L, is negligible. Finally, all images are resized according to their distance to the sensor by taking into account the refraction due to the existence of the flat wall, silicone oil and the circular wall. By use of the resized 2D images, 3D concentration field is constructed and the downstream cross-sectional evolution of the scalar patterns is investigated.

3

The Global Hamiltonian Progression of 2D Lagrangian Flow Topologies From Integrable to Chaotic State

Countless theoretical/numerical studies on transport and mixing in two-dimensional (2D) unsteady flows lean on the assumption that Hamiltonian mechanisms govern the Lagrangian dynamics of passive tracers. However, experimental studies specifically investigating said mechanisms are rare. Moreover, they typically concern local behavior in specific states (usually far away from the integrable state) and generally expose this indirectly by dye visualization. Laboratory experiments explicitly addressing the global Hamiltonian progression of the Lagrangian flow topology entirely from integrable to chaotic state, i.e. the fundamental route to efficient transport by chaotic advection, appear non-existent. This motivates our study on experimental visualization of this progression by direct measurement of Poincaré sections of passive tracer particles in a representative 2D time-periodic flow. This admits (i) accurate replication of the experimental initial conditions, facilitating true one-to-one comparison of simulated and measured behavior, and (ii) direct experimental investigation of the ensuing Lagrangian dynamics. The analysis reveals a close agreement between computations and observations and thus experimentally validates the full global Hamiltonian progression at a great level of detail.

3.1. Introduction

Advection of passive tracers in a two-dimensional (2D) incompressible steady flow defines an autonomous Hamiltonian system with one degree of freedom, where the stream function acts as the Hamiltonian. Here passive tracers are restricted to individual streamlines and, in consequence, always perform non-chaotic motion. Introducing unsteadiness to the flow field causes breakdown of this situation and thus enables (yet not guarantees) chaotic tracer dynamics. This has first been demonstrated for the blinking vortex flow in the seminal paper by Aref (1984) and has since been investigated in numerous studies on a great variety of 2D fluid systems (Aref, 2002; Aref and Balachandar, 1986; Boyland et al., 2000; Chaiken et al., 1986; Chien et al., 1986; Hackborn et al., 1997; Krasnopolskaya et al., 1999; Leong and Ottino, 1989; Meleshko and Peters, 1996; Ottino et al., 1994; Stremler and Chen, 2007; Tel et al., 2000; Yi et al., 2002). Essentially similar dynamics occurs in the continuum regime of 2D unsteady granular flows (Christov et al., 2010; Cisar et al., 2006; Fiedor and Ottino, 2005; Khakhar et al., 1999; Meier et al., 2007) and cross-sections of certain 3D steady flows (Arratia et al., 2005; Fountain et al., 1998, 2000; Shinbrot et al., 2001; Sotiropoulos et al., 2002).

Unsteadiness is (due to its simplicity) commonly introduced by time-periodic variation of the flow field with a certain period time T, where $T = 0$ corresponds with the steady (and thus non-chaotic) state (Aref, 2002; Ott, 2002). Increasing T from zero generically causes the characteristic Hamiltonian disintegration of the global streamline pattern at $T = 0$ ("integrable state") into regular and chaotic regions in the Poincaré section of the flow following the famous KAM and Poincaré-Birkhoff theorems (Ott, 2002). Here regular regions comprise (arrangements of) island-like structures known as "Kolmogorov-Arnold-Moser (KAM) tori".

Investigations on this Hamiltonian progression in 2D incompressible flows to date almost exclusively concern numerical studies. A substantial body of work does exist on experimental analysis of 2D chaotic advection and its impact on transport processes. However, such studies focus predominantly on ramifications and signatures of chaotic advection as e.g. (exponential) stretching and folding of material elements (Ottino et al., 1988; Solomon et al., 2003; Voth et al., 2002), transport enhancement and anomalous diffusion (Fogleman et al., 2001; Solomon and Gollub, 1988; Solomon et al., 1993, 1994; Weeks et al., 1996), crossing of transport barriers (Solomon et al., 1996) and the formation of persistent patterns (Rothstein et al., 1999).

Laboratory experiments dedicated specifically to the Hamiltonian dynamics and kinematic mechanisms that underly the above phenomena (e.g. emergence of periodic points, formation and breakdown of KAM tori, manifold dynamics) are rare, on the other hand. Moreover, they typically concern local behavior in specific states (usually far away from the integrable state) instead of the entire global progression from integrable to chaotic state and generally expose this via dye visualizations (Arratia et al., 2005; Chaiken et al., 1986; Chien et al., 1986; Hackborn et al., 1997; Leong and Ottino, 1989; Yi et al., 2002).

Particularly detailed dye visualizations of KAM tori are those in the 3D steady counterparts to 2D time-periodic flow examined in various studies (Fountain et al., 1998, 2000; Shinbrot et al., 2001; Sotiropoulos et al., 2002). Similar visualization experiments, i.e. on correlations between KAM tori and segregation patterns, have been performed for 2D time-periodic granular flows (Cisar et al., 2006; Fiedor and Ottino, 2005; Khakhar et al.,

1999; Meier et al., 2007). However, direct experimental visualization of the global Hamiltonian progression of 2D Lagrangian flow topologies entirely from integrable to chaotic state is, to the best of our knowledge, non-existent. This motivates our study on visualization of this progression in a representative flow: the 2D time-periodic Rotated Arc Mixer (RAM).

Laboratory experiments will be reconciled with theory through comparison of the measured flow and Lagrangian dynamics with simulated predictions. To this end computations will be performed using an analytical solution to the formal 2D RAM flow and a data-fitted 2D approximation to the measured flow field (so as to account for experimental and modeling imperfections). This enables detailed comparative investigations.

This study, besides to fluid mechanics, contributes to the broader field of experimental state-space visualization and analysis of dynamical systems in two ways. First, existing studies in this context generally concern visualization of (chaotic) attractors in non-Hamiltonian non-fluid systems, e.g. magneto-elastic (Moon and Holmes, 1979, 1985; Moon and Li, 1985) and micro-electromechanical (DeMartini et al., 2007) oscillators, gravity-driven motion of objects (Gottwald et al., 1992), electrical circuits (Roy and Basuray, 2003; Rulkov, 1996) and nonlinear pendulums (Siahmakoun et al., 1997). Our study is dedicated to visualization of essentially Hamiltonian dynamics. Second, said non-fluid systems are finite-dimensional, i.e. their state is described by a finite (and typically small) set of variables (e.g. the tip position of an oscillator (Moon and Holmes, 1985)). Fluid systems, on the other hand, unite characteristics of both finite-dimensional and infinite-dimensional systems and thus also in this sense belong to a different class. Their state is infinite-dimensional by consisting of an infinite union of fluid-parcel positions; these positions, in turn, are each governed by a finite-dimensional (Hamiltonian) system. Hence, the evolution of a single initial state of fluid systems is analogous to the simultaneous evolution of all initial states of said non-fluid systems. Moreover, the physical and state spaces are the same for fluid systems. These properties facilitate direct and full visualization of Hamiltonian dynamics with individual experiments in 2D fluid systems.

3.2. PROBLEM DEFINITION

The RAM is given schematically in Fig. 3.1(left) and consists of a circular domain of radius R enclosed by a wall composed of stationary (black) and moving (gray) arcs (Metcalfe et al., 2006). The four moving arcs, offset by an angle $\Theta = -\pi/2$ (negative sign indicates that the offset is in the direction opposite to the direction of moving arc) and each spanning an angle $\Delta = \pi/4$, drive the internal flow by viscous drag as e.g. in various lid-driven cavity flows investigated in literature (Chien et al., 1986; Krasnopolskaya et al., 1999; Meleshko and Peters, 1996; Stremler and Chen, 2007). Clockwise steady motion only of arc 1 at an angular velocity Ω gives the dark streamline pattern in Fig. 3.1(right); individual activation of arcs 2–4 gives shown reorientations of this pattern. 2D time-periodic flow is accomplished by successive activation of arcs 1–4 each for a duration τ, resulting in $T = 4\tau$ as total period time. Dimensional analysis yields the Reynolds number $Re = \Omega R^2/\nu$ with ν the kinematic viscosity, and dimensionless period time $\mathcal{T} = \Omega T$ as system parameters. Our study is restricted to Stokes flow ($Re = 0$), which can be done without loss of generality, leaving $\mathcal{T}$ as sole parameter.
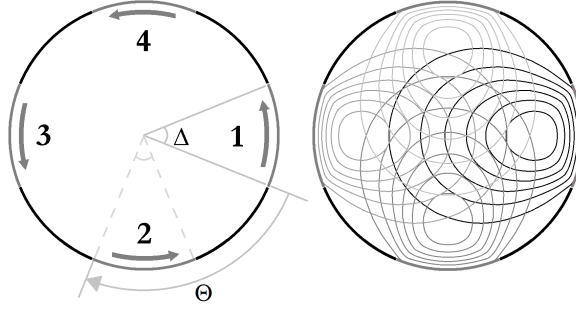
Figure 3.1: 2D Rotated Arc Mixer: (left) circular flow domain bounded by stationary (black) and 4 moving (gray) arcs (opening angle $\Delta = \pi/4$ and offset angle $\Theta = -\pi/2$); (right) streamline patterns induced by individual motion of arcs 1–4 in counterclockwise direction (black: arc 1; gray: arcs 2–4)

The dynamics of passive tracers, described by their current position $\boldsymbol{x}(t)$ and released at initial position $\boldsymbol{x}_0$, is governed by the Hamiltonian equations of motion

$$\frac{dx}{dt} = \frac{\partial H}{\partial y}, \quad \frac{dy}{dt} = -\frac{\partial H}{\partial x}, \tag{3.1}$$

with $H(x, y, t) = H(x, y, t + \mathcal{T})$ the corresponding (time-periodic) Hamiltonian (Aref, 1984; Ott, 2002). Here H can (using polar coordinates (r, θ)) be arc-wise constructed from the stream function $\psi(x, y)$ corresponding with arc 1, i.e. $H(r, \theta)|_{\text{arc } n} = \psi(r, \theta - (n-1)\Theta)$ for $1 \leq n \leq 4$ and $\Theta = -\pi/2$, where ψ is available in closed form through Hwu et al. (1997). This analytical solution will be employed in two ways: (i) description of the Stokes flow in the 2D RAM; (ii) determination of a Stokes-flow approximation to the experimental flow so as to reconcile observed and predicted behavior (Section 3.4).

The tracer dynamics is examined by Poincaré sections $\boldsymbol{X}(\boldsymbol{x}_0) = \{\boldsymbol{x}_0, \boldsymbol{x}_1, ...\}$, with $\boldsymbol{x}_p = \boldsymbol{x}(p\mathcal{T})$ the position after p periods, versus dimensionless period time $\mathcal{T}$:

- Limit $\mathcal{T} \to 0$ yields an autonomous Hamiltonian consisting of the average of the arc-wise stream functions: $H(r, \theta) = \frac{1}{4}\sum_{n=1}^{4} \psi(r, \theta - (n-1)\Theta)$ This corresponds with simultaneous activation of all arcs and defines the integrable limit (Fig. 3.2(a)).

- Non-zero $\mathcal{T} > 0$ introduces unsteadiness and breaks the integrable state. This manifests itself in the characteristic Hamiltonian breakdown of the global island of the integrable state into a progressively smaller central island surrounded by emerging island chains and a chaotic sea (Figs. 3.2(b–d)).

The Poincaré sections in Figs. 3.2(b–d) are simulated by numerical integration of Eq. 3.1 using the analytical stream function following Hwu et al. (1997) and 20 initial positions $\boldsymbol{x}_0$ consisting of two equidistant distributions of 10 tracers each on the x- and y-axis (origin at domain center). The key objective of our study is to experimentally visualize and validate this progression by direct measurement of the Poincaré sections via tracking of tracer particles.

The tracking approach has key advantages over dye visualization for the present kind of experiments. Particles namely mark individual fluid parcels and, inherently, visualize
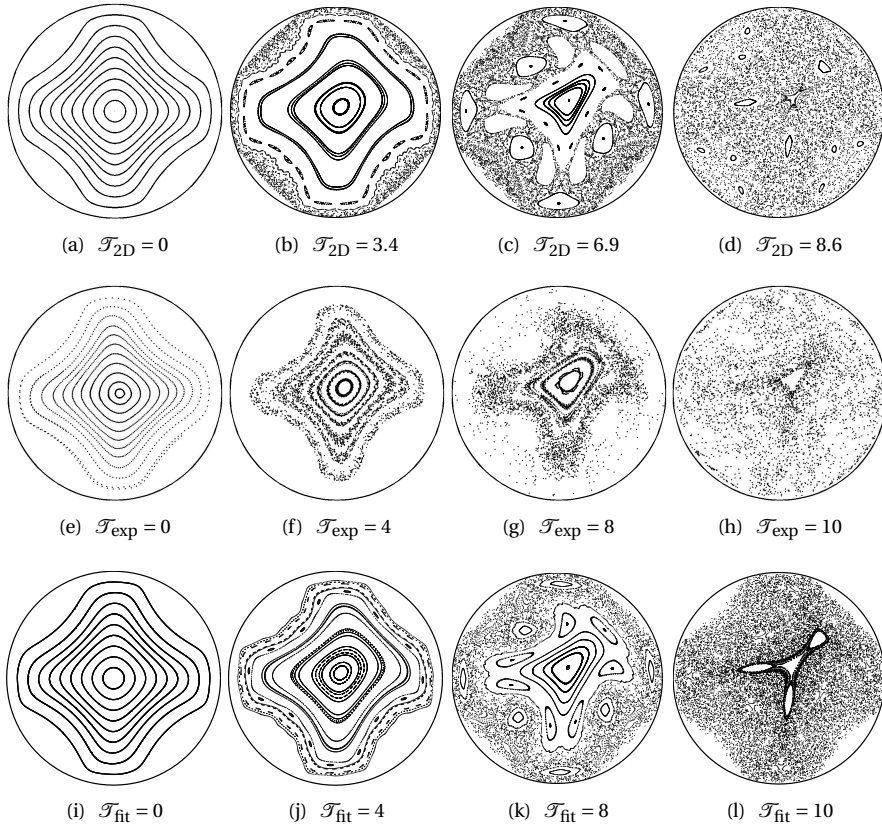
Figure 3.2: Hamiltonian progression of the Lagrangian flow topology of the 2D time-periodic RAM from integrable to (nearly) chaotic state: simulated Poincaré sections using the analytical 2D Stokes flow (top) versus experiments (center) and simulations using the Stokes-flow fit to the experimental surface flow (bottom). The experimental analysis is discussed in Secs. 3.3–3.5; the Stokes-flow fit and adjustment in period times are discussed in Sec. 3.4.

Lagrangian entities in the Poincaré section from the first period on. Dye patterns, on the other hand, converge on such entities strictly only in the limit of infinite time, meaning that finite-time dye traces can basically only approximate Lagrangian entities. (Compare e.g. with the evolution of concentration patterns in distributive mixing (Metcalfe et al., 2012)). An alternative dye visualization method exists in time-averaging of successive dye patterns (Sotiropoulos et al., 2002). However, this strictly also requires an infinite sequence. Moreover, employment of tracer particles enables accurate replication of the experimental initial conditions in numerical simulations, which facilitates true one-to-one comparison and validation of features and behavior. A further argument in favor of tracer particles here is that molecular diffusion is far less relevant than for dye. This is a crucial practical factor for the long-term visualization experiments in our study (Sec. 3.3).

3.3. EXPERIMENTAL PROCEDURE

The experimental apparatus is shown schematically in Fig. 3.3. Different from the setup shown in Fig. 2.1, a modified version that consists of four apertures with an offset angle Θ of −90° is used in the experiments presented in this chapter. The experiments are conducted at isothermal conditions and the belt velocity is set to U = 5 mm/s. The reader is referred to Section 2.2 for detailed information about the experimental setup and the measurement system.
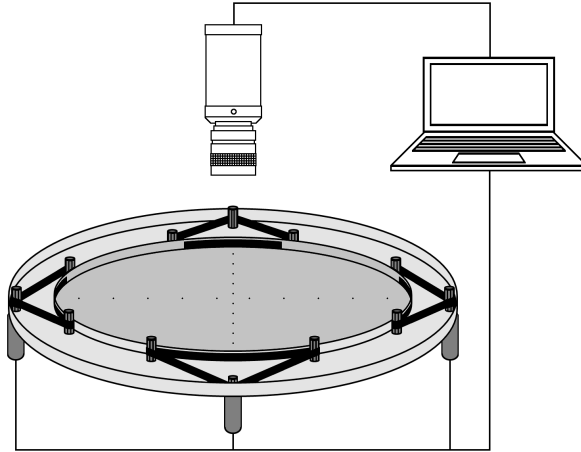
Figure 3.3: Schematic of the experimental facility: test section (dark gray) enclosed by external annular region (light gray) holding 4 computer-controlled motor-belt systems (black) that create the moving arcs. Poincaré sections are measured by tracking of tracer particles floating on the fluid interface (dots indicate initial positions) by an overhead CCD camera.

Direct measurement of the Poincaré sections is achieved by combining the successive positions of tracer particles in exactly the same way as the numerical Poincaré sections are attained. To this end polystyrene foam particles (diameter d_p = 1.5 mm and density ρ_p = 500 kg/m^3) are released on the free surface of the top layer ($\rho_p < \rho_{\text{silicon oil}}$ = 970 kg/m^3 ensures they remain floating throughout the experiment). The typical response time of particles to changes in velocity is estimated at $T_p = d_p^2 \rho_p/(18\rho_f \nu_f)$ = 6.4 μs, which is negligible compared to the typical flow time scale $T_a = R/U = \Omega^{-1}$ = 50 s, meaning they are indeed passively advected by the flow (Raffel et al., 1998). Tracer particles are released at the same 20 positions as in the numerical simulations and their subsequent positions after each period are recorded by a CCD camera synchronized with the motion control system (type Pike F145B, Allied Vision Technology, Germany) placed above the fluid surface (Fig. 3.3). The particle positions are determined from the imagery in sub-pixel accuracy by a dedicated particle detection code implemented in the high-level programming language MATLAB and combined into experimental Poincaré sections. Note that detection of particles suffices to construct Poincaré sections; actual tracking of individual particles is unnecessary. One pixel corresponds for given camera resolution of 1388×1038 pixels^2 with

approximately 0.5×0.5 mm^2, meaning that an individual particle covers about 3×3 pixels^2, which ensures reliable detection of the particle location. Experiments are run for 250 periods in all cases. The actual period time is $T = \Omega^{-1}\mathcal{T} = 50\mathcal{T}$ s, amounting for a typical dimensionless period time $\mathcal{T} = 5$ to $T = 250$ s and a total duration of about 17 hours. It is important to note that dye visualization over such extensive time spans is extremely difficult if not impossible due to molecular diffusion. This basically leaves tracer particles as the sole option for this kind of experiment. The results below demonstrate that this indeed enables successful visualizations.

Furthermore, velocity measurements by way of Particle Image Velocimetry (PIV) are performed in the current laboratory set-up using the approach following Baskan et al. (2015) so as to support the analyses. This involves employment of the same optical set-up and tracer particles as described above. Particle imagery has been processed with the commercial PIV package `PIVview 3C Version 2.4` using interrogation windows of size 24×24 pixels^2 with an overlap factor of 50%. Consult Sec. 2.4.1 for further details.

3.4. EXPERIMENTAL FLOW FIELD

One premise of the current analysis is that the experimental surface flow adequately represents the analytic 2D Stokes flow introduced in Section 3.2. Examinations of the surface flow in Section 4.4.1 revealed a close agreement with 2D Stokes flow. However, for the current study, compliance with these conditions is far more critical, since (experimental) visualization of the Lagrangian flow topology by passive tracers is a long-term process that is very sensitive to minute deviations. This necessitates further analysis.

Said premise holds true wherever the experimental surface flow admits expression as a 2D Stokes flow driven by azimuthal motion of the circular boundary. This is, expanding on the flow field given in Section 4.4.1, investigated below for the base flow corresponding with the first window. To this end the azimuthal boundary condition is expressed in the generic form

$$u_\theta(1,\theta) = f(\theta) = \sum_{n=1}^{\infty} \alpha_n f_n(\theta), \tag{3.2}$$

with $f_k(\theta) = \delta(\theta - \theta_k)$, $0 \le \theta_k \le 2\pi$ a single angular position on the circular boundary and $\delta(.)$ the Kronecker delta function ($f_n(\theta) = 1$ for $\theta = \theta_n$ and zero elsewhere). (Note $u_r(1,\theta) = 0$ for all θ.) This structure, by virtue of linearity of Stokes flows, carries over to the internal flow, yielding

$$\boldsymbol{u}(\boldsymbol{x}) = \sum_{n=1}^{\infty} \alpha_n \boldsymbol{u}_n(\boldsymbol{x}), \tag{3.3}$$

with $\boldsymbol{u}_n$ the elementary flow field given by the analytical solution of Hwu et al. (1997) for boundary condition $u_r(1,\theta) = 0$ and $u_\theta(1,\theta) = f_n(\theta)$. Discrete approximation of Eq. (3.2) as

$$f(\theta) \approx \sum_{n=1}^{N} \alpha_n f_n^*(\theta), \tag{3.4}$$

with $f_n^*(\theta)$ the top-hat function ($f_n^*(\theta) = 1$ for $2\pi(n-1)/N \le \theta \le 2\pi n/N$ and zero elsewhere) enables determination of expansion coefficients α_n from the experimental flow field obtained through PIV via the least-squares method, which in matrix notation yields the linear set of equations (Strang, 1976)

$$A\alpha = b, \tag{3.5}$$

with $\alpha = [\alpha_1, ..., \alpha_n]$,

$$A = \begin{bmatrix} u_{1,r}(r_1) & \cdots u_{N,r}(r_1) \\ \vdots & \vdots \\ u_{1,r}(r_M) & \cdots u_{N,r}(r_M) \\ u_{1,\theta}(r_1) & \cdots u_{N,\theta}(r_1) \\ \vdots & \vdots \\ u_{1,\theta}(r_M) & \cdots u_{N,\theta}(r_M) \end{bmatrix}$$

and

$$b^T = [u_{r,\exp}(r_1) \cdots u_{r,\exp}(r_M), u_{\theta,\exp}(r_1) \cdots u_{\theta,\exp}(r_M)],$$

where r_m are the data positions. The coefficients subsequently follow from

$$\alpha = (A^T A)^{-1} A^T b, \tag{3.6}$$

and accomplish an orthogonal projection of the experimental field on the 2D Stokes flow.

The order of approximation N of expansion (3.4) is determined via the resolution of PIV. The employed settings according to Sec. 3.3 yield interrogation windows with relative size $(\Delta x/R, \Delta y/R) = (0.03, 0.04)$, signifying a relative spatial resolution of $\Delta = \max(\Delta x/R, \Delta y/R) = 0.04$. One $\Delta \times \Delta$ cell within the spatial grid thus defined can hold a circular boundary segment with maximum arc length of approximately $\Delta s = \sqrt{2}\Delta$. This determines the corresponding relative spatial resolution on the circular boundary and translates into a grid of $2\pi/\Delta s = \sqrt{2}\pi/\Delta \approx 110$ boundary segments. The latter sets the upper bound for N, since it slightly overestimates the true boundary resolution. The arc length of boundary segments is namely estimated by the diagonal of a $\Delta \times \Delta$ cell, while the actual segments are curved and thus slightly longer. Hence, N must be set somewhat below this upper bound for Eq. (3.3) to be consistent with the PIV resolution.

Important to note is that N cannot be determined through an unambiguous convergence criterion. The quality of the Stokes fit is namely determined by the degree to which it adequately captures that part of the experimental surface flow that behaves as a 2D Stokes flow. However, strict separation between surface regions with Stokes and non-Stokes behavior – and thus definition of said criterion – is impossible. Instead, convergence and quality of the Stokes fit has been examined by its sensitivity to variation of N in the range $80 \le N \le 110$. This revealed appreciable variations only in the direct window proximity, that is, the area identified as the non-Stokes-flow region in Sec. 3.4. Sensitivity to changes in N outside these areas proved marginal, on the other hand, signifying (sufficient) convergence of the Stokes fit to that part of the experimental surface flow that exhibits 2D Stokes behavior. Thus N can basically be chosen arbitrarily in the examined range; here $N = 90$ has been adopted.

Figure 3.4 gives the boundary profile $f(\theta)$ according to Eq. (3.4) thus attained (black solid) for $N = 90$ in comparison with that of the true 2D configuration (gray dashed). This reveals an overall good correspondence, giving a first indication that the surface flow indeed (largely) behaves as a 2D Stokes flow. (Discrepancies with full 2D Stokes flow are discussed below.) It must be stressed that $f(\theta)$ does not represent the true experimental boundary condition, but the boundary condition of the Stokes fit to the surface flow. Hence, departures of $f(\theta)$ from the imposed boundary condition do not signify experimental imperfections. Moreover, $f(\theta)$ must not be interpreted in terms of physical characteristics of the flow. Its profile, instead of reflecting flow physics, most and for all is a consequence of fitting a 2D Stokes flow to an experimental surface flow that not everywhere behaves as such.
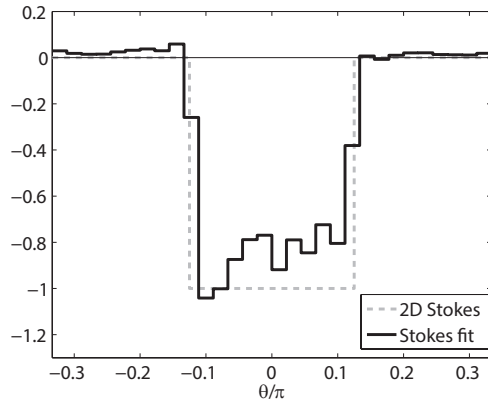
Figure 3.4: Boundary profile (3.2) of the azimuthal velocity: Stokes-flow fit to the experimental surface flow versus full 2D Stokes flow.

The Stokes fit is shown in Fig. 3.5(top) and overall captures the experimental surface flow to a high degree of accuracy; appreciable deviations $\Delta \boldsymbol{u}_{\text{exp-fit}} = \boldsymbol{u}_{\text{exp}} - \boldsymbol{u}_{\text{fit}}$ inside the flow domain occur only very locally in the direct proximity of the driving window (Fig. 3.5, center). Deviations in the radial component u_r are concentrated in peaks at the window edges (indicated by arrows) and in a small patch just above the lower window edge; deviations in the azimuthal component u_θ are confined to a thin layer directly at the window. Hence, save these localized areas, the experimental surface flow to a high degree of approximation behaves as a 2D Stokes flow. This validates the before-mentioned premise of the present study. However, important to note is that the Stokes fit differs essentially from the full 2D Stokes flow for the physical boundary conditions (dashed profile in Fig. 3.4). Comparison of the latter with the surface flow namely reveals, in contrast with the Stokes fit, a significant departure in substantial parts of the domain (Fig. 3.5, bottom). This implies that, despite indeed largely behaving as a 2D Stokes flow, the experimental surface flow exhibits different flow characteristics in the direct proximity of the window.

Direct comparison of Stokes fit and full 2D Stokes flow in Fig. 3.6(top) exposes two important features that may offer an explanation for the above observations: (i) the Stokes-fit velocity is relatively lower; (ii) the deviations closely correlate with the window edges (indicated by arrows). The overall slowing down is in part the result of viscous friction with
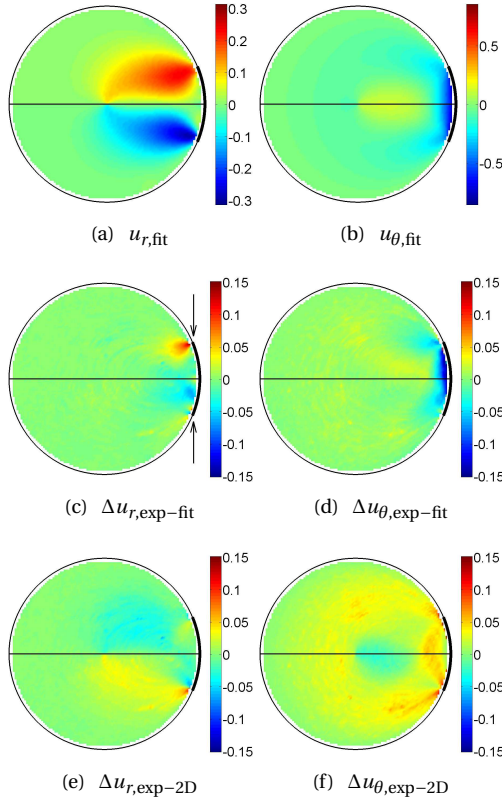
Figure 3.5: Experimental surface flow $\boldsymbol{u}_{\exp}$ versus 2D Stokes-flow representations: Stokes fit $\boldsymbol{u}_{\text{fit}}$ following (3.3) (top); departure Stokes fit from experimental flow $\Delta\boldsymbol{u}_{\text{exp-fit}} = \boldsymbol{u}_{\exp} - \boldsymbol{u}_{\text{fit}}$ (center); departure full 2D Stokes flow from experimental flow $\Delta\boldsymbol{u}_{\text{exp-2D}} = \boldsymbol{u}_{\exp} - \boldsymbol{u}_{\text{2D}}$ (bottom). Arrows indicate window edges.

the bottom wall; this effect is significantly reduced by the two-fluid layer yet can never be fully eliminated (Sec. 3.3). The impact of viscous friction increases near the window edges due to the strong velocity gradients that occur here. This is likely to be aggravated by the formation of an additional vertical boundary layer on the stationary part of the side wall in this region. Fluid inertia is a probable secondary factor by suppressing the actual fluid acceleration relative to its Stokes limit and thus tending to smooth the local velocity gradients near the window edges. This may somewhat mitigate said viscous friction yet at the same time reduce the viscous drag — and thus the effective driving velocity — at the window (which is proportional to the surfacial velocity gradients) that sets up the surface flow. Moreover, such gradient smoothing — and resulting deviation in velocity — will be most pronounced near the window edges, which may explain why the deviations "radiate away" from these regions (Part of the smoothing is inherent in the working principle of PIV; velocities are namely determined on the basis of local average particle displacements. However, this effect alone cannot explain the observations, implying physical causes). Conclusive establishment of the exact causes for the discrepancies requires more detailed analysis.

(a) $\Delta u_{r,\text{2D-fit}}$ (b) $\Delta u_{\theta,\text{2D-fit}}$
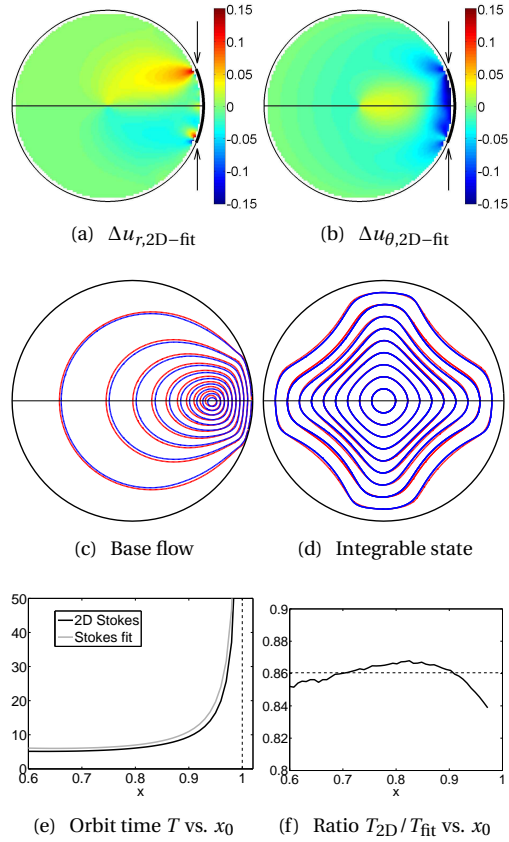
(c) Base flow   (d) Integrable state

(e) Orbit time T vs. x_0 (f) Ratio $T_{\text{2D}}/T_{\text{fit}}$ vs. x_0

Figure 3.6: Comparison of full 2D Stokes flow $\boldsymbol{u}_{\text{2D}}$ versus Stokes fit $\boldsymbol{u}_{\text{fit}}$ to experimental surface flow: departure $\Delta\boldsymbol{u}_{\text{2D-fit}} = \boldsymbol{u}_{\text{2D}} - \boldsymbol{u}_{\text{fit}}$ (top); streamlines base flow/integrable state of $\boldsymbol{u}_{\text{2D}}$ (red) versus $\boldsymbol{u}_{\text{fit}}$ (blue) (center); corresponding orbit times of streamlines base flow (bottom). Arrows indicate window edges.

This is beyond the present scope, however. Relevant here is mainly the demonstration of the 2D Stokes nature of the experimental surface flow everywhere outside the direct vicinity of the window.

Further examination reveals that the discrepancy of the experimental flow with the analytic flow primarily concerns the magnitude of the flow yet not its direction, as evidenced in Fig. 3.6 (center) by the close resemblance of the streamline patterns (emanating from identical initial conditions on the x-axis) of both the base flow and integrable states of Stokes fit (blue) and full 2D Stokes flow (red). This strongly suggests that the Lagrangian dynamics will predominantly differ quantitatively in terms of distance traveled along a trajectory for a given time and thus closely relate via an offset in time. Figure 3.6(e) gives the time T to complete one loop on each closed streamline of the base flow for the full 2D Stokes flow (black) versus the Stokes fit (gray) parameterized by the initial position on the x-axis. (Note that only one side of the stagnation point need be considered.) This exposes a structurally shorter orbit time for the full 2D Stokes flow, or equivalently, a delay of the

Stokes-fit case, by an approximately constant factor $T_{2D}/T_{fit} \approx 0.86$ (Fig. 3.6(f)). Accounting for this shift will be important for proper interpretation and comparison of the results on Lagrangian dynamics.

3.5. Experimental Poincaré sections

The above revealed that the Lagrangian dynamics of the base flows of the Stokes fit and the full 2D Stokes case closely correspond up to a temporal scaling factor: $t_{2D}/t_{Stokes\,fit} \approx T_{2D}/T_{Stokes\,fit} \approx 0.86$. This implies, given the full periodic flow being a composition of re-oriented base flows, that the progressions of the Poincaré sections versus period time for the Stokes fit of the surface flow — and thus the experimental Poincaré sections — will closely follow that of the full 2D Stokes flow upon tuning the period times as

$$\frac{\mathscr{T}_{fit}}{\mathscr{T}_{exp}} = 1, \quad \frac{\mathscr{T}_{2D}}{\mathscr{T}_{exp}} = \frac{\mathscr{T}_{2D}}{\mathscr{T}_{fit}} = 0.86 \tag{3.7}$$

so as to account for said scaling factor.

The experimental Poincaré sections are shown for increasing $\mathscr{T}_{exp}$ in Fig. 3.2 (center) versus their simulated counterparts using the Stokes fit at identical period time $\mathscr{T}_{fit} = \mathscr{T}_{exp}$ (bottom) and the full 2D Stokes flow with $\mathscr{T}_{2D}$ rescaled following Eq. 3.7 (top). Comparison of the measured and predicted progressions reveals an excellent agreement. (Note that time spans for the simulated Poincaré sections are chosen to ensure optimal visualization of features; the number of periods may thus vary and differ from the fixed 250 periods employed in the experiments (Sec. 3.3).) The central island of the experimental progression clearly undergoes the same Hamiltonian breakdown from its original integrable state ($\mathscr{T}_{exp} = 0$) to its strongly diminished state just before the onset of global chaos ($\mathscr{T}_{exp} = 10$). Moreover, both these states as well as the intermediate states at ($\mathscr{T}_{exp} = 4$) and ($\mathscr{T}_{exp} = 8$) are in close agreement with their corresponding simulated states during this progression. This is strong evidence of the fact that simulated and measured dynamics result from the same fundamental (Hamiltonian) mechanisms. Furthermore, this substantiates the Stokes-flow nature of the experimental surface flow established in Sec. 3.4 as well as its translation to the full 2D Stokes flow via a scaling factor.

The behavior near the integrable limit can be further examined via the rotation number

$$\mathscr{R}(\boldsymbol{x}_0) = \lim_{P \to \infty} \frac{1}{P} \frac{\sum_{p=0}^{P-1} \Delta\theta_p}{2\pi}, \tag{3.8}$$

with $\Delta\theta_p = \theta_p - \theta_{p+1}$ and p the step number, describing the average step-wise rotation of a tracer about the origin. (The employed definition of $\Delta\theta_p$ yields $\mathscr{R} > 0$ and $\mathscr{R} < 0$ in case of clockwise and counterclockwise rotation, respectively.) Tracer motion diminishes with decreasing period time $\mathscr{T}$, implying $\lim_{\mathscr{T} \to 0} \mathscr{R}(\boldsymbol{x}_0) = 0$ for all $\boldsymbol{x}_0$. This asymptotic behavior is demonstrated in Fig. 3.7 for experiments at $\mathscr{T}_{exp}$ as indicated (panel (a)) and simulations using the 2D Stokes field with corresponding $\mathscr{T}_{2D}$ according to Eq. 3.7 (panel (b)) for tracers released at the indicated positions $\boldsymbol{x}_0$ on the x-axis. This reveals the distribution of $\mathscr{R}$ over the concentric streamlines that occur near the integrable limit (Fig. 3.2(a)). (Note that isolation of individual trajectories from experimental Poincaré sections for the evaluation of $\mathscr{R}$ is straightforward in this $\mathscr{T}$-range.) Rotation numbers $\mathscr{R}_{exp}$
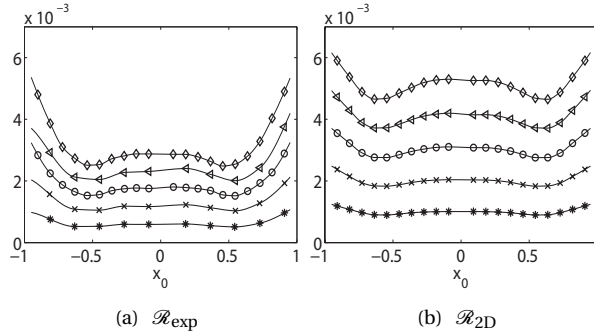
Figure 3.7: Tracer dynamics near the integrable limit $\mathcal{T} \to 0$ investigated by rotation number $\mathcal{R}$ versus step time $T_{\text{step}} = \mathcal{T}/4$: experiments versus simulations by full 2D Stokes flow with rescaling (3.7). Symbols differentiate T_{step}: $T_{\text{step}} = 0.05$ ($\diamond$); $T_{\text{step}} = 0.1$ ($\triangleleft$); $T_{\text{step}} = 0.15$ ($\circ$); $T_{\text{step}} = 0.2$ ($\times$); $T_{\text{step}} = 0.25$ ($*$); x_0 indicates initial tracer position on the x-axis.

and $\mathcal{R}_{\text{2D}}$ both meet $\mathcal{R} > 0$, signifying counter-clockwise tracer rotation along with the rotor (Fig. 3.1(a)). Moreover, they closely agree with respect to magnitude and (in particular) qualitative dependence on initial position x_0 and approach the limit $\mathcal{R} = 0$ with decreasing $\mathcal{T}$ at a comparable rate. Minor quantitative differences exist in that the experiments asymptote somewhat faster towards the integrable limit.

The particular distribution of $\mathcal{R}$ over the concentric streamlines reveals that the tracer motion basically consists of two regimes separated by a "minimum-rotation" streamline at $r \approx 0.5$. (The streamline pattern can for the purpose of this discussion be treated as being axisymmetric, allowing substitution of x_0 by r.) Development of a plateau in $\mathcal{R}$ towards the center signifies solid-body-like behavior ($d_\theta/d_t \sim w \leftrightarrow R \sim wT_{\text{step}}$); linear growth towards the boundary signifies shear-like behavior ($d_\theta/d_t \sim wr \leftrightarrow R \sim wT_{\text{step}}r \propto r$). Thus the departure from integrability sets in via emergence of these coexisting fluid motions. Shear and solid-body flow are of comparable strength in the simulations for all T_{step} (maximum of $\mathcal{R} \approx 0.005$ revolutions per step in both regimes). The experiments, on the other hand, exhibit a relative intensification of shear versus solid-body flow with growing T_{step}: $\mathcal{R}_{\text{shear}} = \mathcal{R}_{\text{solid-body}} \approx 1$ at $T_{\text{step}} = 0.05$ to $\mathcal{R}_{\text{shear}} = \mathcal{R}_{\text{solid-body}} \approx 5/3$ at $T_{\text{step}} = 0.25$. However, overall the flow remains very weak; a tracer typically takes at least $\mathcal{R}^{-1} \approx 0.005^{-1} = 200$ steps for one revolution. The close agreement between experiments and simulations near the integrable limit, notwithstanding minor quantitative differences, further substantiates the earlier finding that they are subject to the same (Hamiltonian) mechanisms.

The experiments also provide (circumstantial) evidence of island chains. The region surrounding the central island at $\mathcal{T}_{\text{fit}} = 8$ ($\mathcal{T}_{\text{2D}} = 6.9$) is e.g. dominated by the two period-7 island chains highlighted in Figs. 3.8(a,c). The simulated outer island chain (blue in Figs. 3.8(a,c)) coincides well with the "blank zones" in the corresponding experimental Poincaré section at $\mathcal{T}_{\text{exp}} = 8$. This is demonstrated in Figs. 3.8(b) and (d) by inserting the simulated period-7 island chains of Figs. 3.8(a) and (c), respectively, in the experimental Poincaré section (black), revealing that both parts indeed fit like pieces of a puzzle. Moreover, an inner period-7 chain and accompanying chaotic band can be identified in the experimental results that coincides with a period-7 island chain in the simulations (red

3

(a) $\mathcal{T}_{\text{fit}} = 8$ (b) $\mathcal{T}_{\text{exp}} = 8$

(c) $\mathcal{T}_{\text{2D}} = 6.9$ (d) $\mathcal{T}_{\text{exp}} = 8$
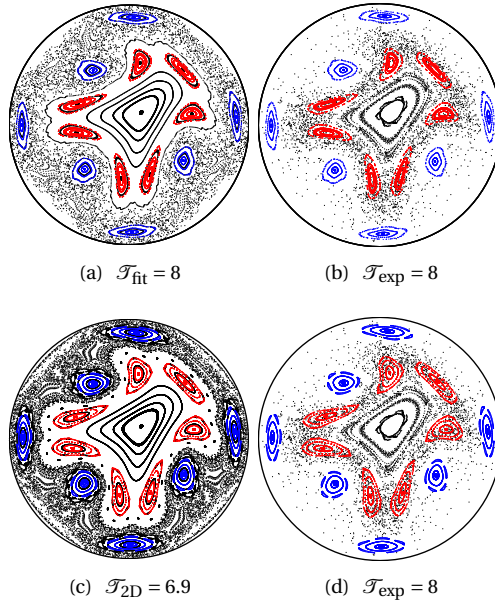
Figure 3.8: Circumstantial experimental evidence for island chains: coincidence of the simulated outer (blue) and inner (red) period-7 chains using the Stokes fit to the surface flow (panel (a)) and the adjusted full 2D Stokes flow (panel (c) with the "blank zones" of the experimental Poincaré section at $\mathcal{T}_{\text{exp}} = 8$ (right; simulated island chains of panels a and c inserted in respectively panels b and d).

in Figs. 3.8(a,c)). This coincidence is demonstrated in Figs. 3.8(b) and (d) by overlaying these entities with the numerical island chains of Figs. 3.8(a) and (c), respectively. The mismatch in dynamical state (i.e. intact simulated islands versus partially disintegrated experimental islands), rather than signifying a fundamental difference, must be attributed to the high sensitivity—and intrinsic unpredictability—of such island chains (typically increasing with smaller size) to parametric variations and weak (experimental) disturbances (e.g. finite-size effects of tracer particles). They namely emanate from instability of resonant orbits of the original island and are therefore far less robust than the latter. The experimental period-7 chain may thus already be in a relatively higher state of disintegration, which is consistent with the fact that this chain is embedded in a chaotic band that coincides well with the simulated inner period-7 island chain. Hence, despite lack of one-to-one correspondence between all individual features, also for island chains a close agreement between simulations and experiments is observed. Important to note is that this element of unpredictability in the actual state of the island chains is inherent in the nature of the system and not a consequence of experimental imperfections per se.

3.6. Conclusions

This study provides (to the best of our knowledge) the first experimental investigation of the global Hamiltonian progression of the Lagrangian flow topology of 2D time-periodic

flows entirely from integrable to chaotic state by direct measurements of Poincaré sections. To this end the 2D time-periodic Rotated Arc Mixer has been adopted as representative flow. The analysis reveals a close agreement between simulated and measured dynamics and thus experimentally validates the Hamiltonian mechanisms that are assumed to govern the Lagrangian dynamics in the considered flow class. The first analyses by the rotation number $\mathscr{R}$ lay the groundwork for quantitative experimental studies on the onset of chaos. Key to the latter are symmetry breaking and resonance of trajectories, which are inextricably linked to symmetry and mode locking. These "locking phenomena" admit quantification by (generalized definitions of) $\mathscr{R}$ and have thus been investigated theoretically and numerically in parametric studies by Lester et al. (2014).

4

SCALAR MODES IN A PERIODIC LAMINAR FLOW

Scalar fields can evolve complex coherent structures under the action of periodic laminar flows. This comes about from the competition between chaotic advection working to create structure at ever finer length scales and diffusion working to eliminate fine-scale structure. Recently, analysis of this competition in terms of spectra of eigenfunctions of the advection–diffusion equation has proven fruitful because these spectra contain both fundamental information about how mixing processes create emergent Lagrangian coherent structure and also clues about how to optimize flows for heat and mass transfer processes in industry. While theoretical and computational studies of ADE spectra exist for several flows, experiments, to date, have focused either solely on the asymptotic state or on highly idealized flows. Here a coupled experimental and computational study of the spectrum for the scalar evolution of a model of an industrially relevant viscous flow is shown. The main results are the methods employed in this study corroborate the eigenmode approach and the outcomes of different methods agree well with each other. Furthermore, this study employs a Lagrangian formalism for thermal analysis of convective heat transfer in the representative geometry to determine the impact of the fluid motion in the thermal homogenization process. The experimental/numerical methods and tools used in the current study are promising for further qualitative parameter studies of the mixing/heat transfer characteristics of many inline mixers and heat exchangers.

4.1. INTRODUCTION

Classification of industrial heat transfer processes with respect to their ultimate goals admits the application of goal-oriented methods for the investigation of thermal phenomena. In literature these processes are analyzed in two groups: rapid thermal homogenization processes and heat transfer processes with high transfer rates in inhomogeneous directions, see Speetjens and van Steenhoven (2010). Examples of thermal homogenization processes are the production of foods, polymers, steel and glass whereas heat treatment of certain polymers is an example for the latter class of processing.

Thermal homogenization is mainly the evolution of the temperature field from its non-uniform initial state towards the final homogeneous state where the evolution to the final state is governed by the balance between advection and diffusion. Advective-diffusive transport of passive scalars in both time-periodic and spatially-periodic flow fields have been studied extensively (Adrover et al., 2001; Lester et al., 2008, 2009; Liu and Haller, 2004; Pikovsky and Popovych, 2003; Popovych et al., 2007; Rothstein et al., 1999; Voth et al., 2003) since the pioneering work in Pierrehumbert (1994) on 'strange eigenmodes' — periodic modes with highly complex spatial structure in the limit of zero-diffusivity. These studies are mainly focused on the decomposition of an advecting-diffusing scalar field into its spatial and temporal components: spatial patterns are persistent (and repeating in the case of a time-periodic flow field), whereas temporal evolution is the exponential decay of intensities from a non-uniform initial state with high variance toward a fully uniform state (with zero variance). The most-persistent spatial patterns governing the asymptotic scalar transport, so-called 'dominant eigenmodes', which in the limit of arbitrarily small diffusivity coincide with the 'strange eigenmodes', are the slowest decaying eigenmodes of the advection–diffusion operator and can be found by the decomposition of the linear operator into its eigenfunction–eigenvalue pairs without the necessity of solving the full advection–diffusion equation (ADE). In the case of an experimental approach, however, the information at hand is the data sequence rather than a mathematical model. Thus, a data processing method capable of capturing the dynamics is necessary to determine dominant eigenmodes and corresponding decay rates of the experimentally acquired time-resolved scalar fields. The dynamic mode decomposition (DMD) is a technique that extracts dynamic information by decomposing the data set into temporal and spatial components such that each mode corresponds to a complex-valued eigenvalue (Schmid, 2010, 2011). In the present work, the DMD method is employed to determine the eigenmodes and decay rates of both experimentally and numerically acquired scalar fields derived from time-periodic advection.

In contrast, heat transfer processes which necessitate high transfer rates in preferred directions require a Lagrangian approach rather than the use of traditional heat transfer analysis methods based on integrated quantities or empirical correlations. Such an approach enables in-depth analysis of the thermal topology of the heat transfer process and, in turn, optimization of thermal transport routes. The Lagrangian formalism introduced in the work by Speetjens (2012) provides a generalized Lagrangian framework for the analysis of heat transfer in which the impact of the fluid motion on the scalar distribution is determined. In this study, the formalism is demonstrated for the temperature field in a representative industrial mixer/heat exchanger, however, it can be applied to any advective-diffusive scalar field. The formalism is also combined with the eigenmode

analysis to show that two groups of processes (rapid thermal homogenization processes and heat transfer processes with high transfer rates in inhomogeneous directions) can be analyzed by the same spectral methods.

The main objective of the current study is to experimentally investigate and validate the fundamental eigenmode structure of scalar fields. For this purpose, the Rotated Arc Mixer (RAM) is adopted as the representative configuration for in-depth analysis of advective-diffusive transport of scalars in realistic inline mixers. An experimental setup representing simplified 2D RAM geometry is developed and temperature/concentration field measurements are conducted to observe the evolution of advective-diffusive or only-advective scalar fields. The advection–diffusion equation (ADE) is spectrally decomposed into its eigenmode–eigenvalue pairs and the most slowly decaying eigenmode, in other words, the dominant eigenmode is set as the benchmark for a comparative study between spectral, numerical and experimental analysis. The practicality of experimental, numerical and analytical tools for the in-depth analysis of mixing and heat transfer in the 2D RAM is also discussed to expose the advantages or limitations of these tools.

4.2. MODELING FLOW AND HEAT TRANSFER

4.2.1. CONFIGURATION AND GOVERNING EQUATIONS

The configuration is a time-periodic, laminar, incompressible flow field and its associated time-dependent advective-diffusive scalar field inside the 2D domain $\mathscr{D}$ representing the circular cross sectional area of the RAM. The governing non-dimensional mass, momentum and advection–diffusion equations are

$$\nabla \cdot \boldsymbol{u} = 0, \ \ Sr \, \frac{\partial \boldsymbol{u}}{\partial t^*} + Re \, \boldsymbol{u} \cdot \nabla \boldsymbol{u} = -\nabla P + \nabla^2 \boldsymbol{u}, \tag{4.1}$$

$$\frac{\partial C}{\partial t} + \boldsymbol{u} \cdot \nabla C = \frac{1}{Pe} \nabla^2 C, \ \ C(\boldsymbol{x}, 0) = C_0(\boldsymbol{x}), \tag{4.2}$$

where $\boldsymbol{u}$ is the fluid velocity, P the pressure and C the scalar field. Here, Sr, Re and Pe are the Strouhal, Reynolds and Péclet numbers, respectively, defined as

$$Sr = \frac{R^2}{\nu T^*}, \ \ Re = \frac{UR}{\nu}, \ \ Pe = \frac{UR}{\alpha}, \tag{4.3}$$

where U and R are the characteristic velocity of the flow field and the radius of the domain, respectively. ν is the kinematic viscosity, α the material (or thermal) diffusivity and T^* the reference time scale (i.e. the forcing period) for dimensionless variable t^*. The unsteady term in Eq.(4.2) is non-dimensionalized by the advection time scale $T_{\mathrm{a}} = R/U$, hence t^* relates to t by $t^* = t T^* U/R$. For the experiments it turns out that $Re \approx 0.1$ and $Pe \approx 10000$ (see Section 4.3.2 for the values of ν, α, U and R). The scalar concentration (or temperature) is made dimensionless according to $C = (\mathrm{C} - \min C_0(\boldsymbol{x}))/(\max C_0(\boldsymbol{x}) - \min C_0(\boldsymbol{x}))$, with C the dimensionful scalar, $\min C_0(\boldsymbol{x})$ and $\max C_0(\boldsymbol{x})$ the minimum and maximum value of the initial scalar field $C_0(\boldsymbol{x})$, respectively.

The response of the stagnant fluid to the impulsive start of a steady forcing is taken into account to assess the validity of piece-wise steady flow assumption for the case of interest.

The Strouhal number is then defined as the ratio of the viscous to the forcing time scale reading

$$Sr = \frac{T_v}{T_s} \tag{4.4}$$

with the viscous time scale $T_v = R^2/\nu$ and the dimensionful forcing period per motion step $T_s = T^*$. For the current configuration with $T_s = 625$ s we obtain $Sr \approx 0.01$, which is sufficiently small to neglect the acceleration stage and to assume that the flow is piecewise steady. Hence, Eq.(4.1) reduces to

$$\nabla \cdot \boldsymbol{u} = 0, \quad Re\, \boldsymbol{u} \cdot \nabla \boldsymbol{u} = -\nabla P + \nabla^2 \boldsymbol{u}. \tag{4.5}$$

These equations are also supplemented with no-slip velocity boundary conditions at the boundary of the domain $\Gamma = \partial \mathcal{D}$.

Thermal analysis concerns the configuration with heat transfer from a hot isothermal wall to an initially (homogeneous) cold fluid advected by a time-periodic piece-wise steady flow. The configuration for the concentration field analysis is the same except for the Péclet number. In the latter case, which corresponds to infinite-Pe limit (infinite-Pe implies zero-diffusivity), there is no scalar transport across the boundary and the evolution initializes with a non-homogeneous scalar field. The current setup of the 2D RAM holds two apertures facing each other ($\Theta = 180°$), with the aperture arc angle $\Delta = 45°$ (Figure 1.2 (right)). The time-periodic flow field is established by a sequential prescription of the tangentially moving wall condition at the apertures (Figure 4.1) with $\tau = T_s U/R$ the non-dimensional period of switching from one aperture to the consecutive one fixed at $\tau = 10$ (τ relates to the period of motion by $\tau = \mathcal{T}/p$ where $\mathcal{T}$ is the non-dimensional period of motion and m and p are integers satisfying $\Theta/2\pi = m/p$ and in this study $m = 1$ and $p = 2$). At any instant there is only one aperture activated, while the remaining part of the circular boundary is stationary.
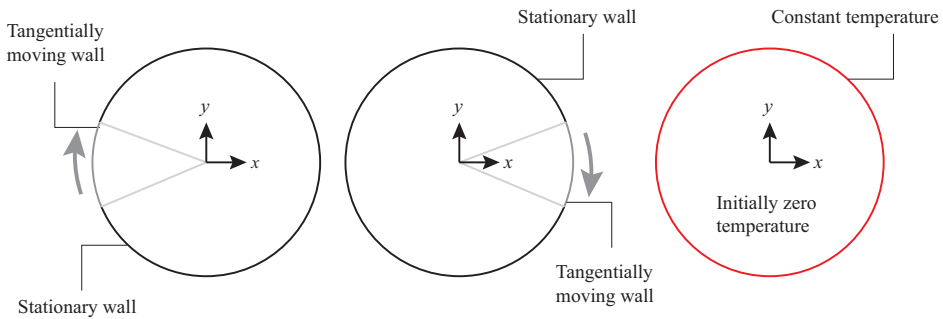

Figure 4.1: Schematic views of the 2D computational domain used for temperature evolution simulations: Configuration for the actuation of the left aperture in the first half of a period (left panel), the actuation of the right aperture in the second half of a period (mid panel), and finally the temperature field initial and boundary conditions (right panel).

4.2.2. EIGENMODE STRUCTURE OF SCALAR FIELDS

In scalar transport slowly decaying persistent patterns, known as the eigenmodes, are the fundamental solutions of the ADE. In time-periodic flow fields, these patterns are defined as the Floquet modes of the advection-diffusion operator $\mathscr{L}_2 = -\boldsymbol{u}\cdot\nabla + Pe^{-1}\nabla^2$ of Eq.(6.2). The scalar field $C(\boldsymbol{x}, n\mathscr{T})$, where $\mathscr{T} = p\tau$ is the non-dimensional period of motion and $n\mathscr{T}$ the integer multiples of $\mathscr{T}$, can be approximated as a finite sum of these modes, yielding

$$C(\boldsymbol{x}, n\mathscr{T}) = \sum_{k=0}^{K} \gamma_k \varphi_k(\boldsymbol{x})\lambda_k^n, \ \ \lambda_k = e^{\mu_k \mathscr{T}} \tag{4.6}$$

where the γ_k are the expansion coefficients based on initial conditions, the $\mathscr{H}_k(\boldsymbol{x}, n\mathscr{T}) = \varphi_k(\boldsymbol{x})\lambda_k^n$ Floquet modes, $\mu_k = \sigma_k + \mathrm{i}\omega_k$ with $\mathrm{i} = \sqrt{-1}$ Floquet exponents and the set $\{\varphi_k, \mu_k\}$ represent the corresponding eigenfunction-eigenvalue pairs governed by the eigenvalue problem

$$\mathscr{L}_2\varphi_k - \mu_k\varphi_k = 0. \tag{4.7}$$

In the case of finite-Pe, the real part of any Floquet exponent $\sigma_k < 0$ or equivalently any eigenvalue $|\lambda_k| < 1$ for non-uniform eigenmodes which means that these modes all decay exponentially in time. The slowest one is the dominant mode, and represented by the set $\{\varphi_0, \mu_0\}$, causing the evolution to quickly become governed by the reduced expansion

$$C(\boldsymbol{x}, n\mathscr{T}) = \gamma_0\varphi_0(\boldsymbol{x})e^{\mu_0 n\mathscr{T}} + C_\infty(\boldsymbol{x}). \tag{4.8}$$

For the current configuration with $C|_\Gamma = 1$, $C_\infty(\boldsymbol{x}) = C|_\Gamma$ is the trivial uniform eigenmode that corresponds to $\mu_k = 0$. Note that eigenmodes $\mathscr{H}_k$, typically are non-zero everywhere for finite-Pe (see Gorodetskyi et al. (2014); Metcalfe et al. (2012)).

In the limit of infinite-Pe, diffusion is negligible and therefore no scalar exchange with the wall happens. Transport then becomes equal to passive advection of a scalar. A fundamental difference with the finite-Pe case is that now only purely imaginary exponents (i.e. $\mu_k = \mathrm{i}\omega_k$) occur for all eigenmodes, meaning that none of the eigenmodes will decay. This has the fundamental implication that asymptotic states become non-uniform and quasi-periodic ($C_\infty(\boldsymbol{x}, n\mathscr{T}) = \sum_k \gamma_k\varphi_k(\boldsymbol{x})e^{\mathrm{i}\omega_k n\mathscr{T}}$). However, here eigenmodes become spatially arranged according to islands and chaotic regions (Speetjens et al., 2013). For periodic systems in the infinite-Pe limit, the eigenmodes become intimately related to the periodicity and multiplicity of the coherent structures in the Poincaré section and periodic eigenmodes (i.e. $\omega_k = 2\pi j/\mathscr{T}$) with "low" periodicity (i.e. $j = 1, 2$) dominate the behavior and in that sense act as the dominant eigenmodes. The reason for this dominance of lower-order eigenmodes is that higher-order structures are always embedded in lower-order structures. Lower-order structures therefore correspond with (global) larger-scale features, while higher-order structures correspond with (local) smaller-scale features (see Metcalfe et al. (2012)).

In this Chapter, the scalar field, $C(\boldsymbol{x}, t)$ is decomposed into its eigenmodes via Fourier-Bessel functions. The dominant eigenmode $\varphi_0(\boldsymbol{x}, t)$ and its decay rate (or Floquet exponent) μ_0 are determined for the aforementioned configuration in the 2D RAM. The reader is referred to the study by Lester et al. (2008) for the details of the calculation.

4.2.3. Convective heat transfer

Convective heat transfer in the simplified 2D RAM configuration is investigated by the Lagrangian heat transfer formalism proposed by Speetjens (2012). The main advantage of the formalism is its capability to isolate and to visualize the energy redistribution and energy fluxes induced by the flow. This facilitates a more direct description and analysis of convective heat transfer compared to conventional (integral) methods based on wall heat-transfer coefficients. The integrated values from conventional methods measure the gross amount of thermal energy that crosses the boundary, while the decomposition here is aimed at revealing thermal coherent structures and thermal transport routes inside the domain. This enables a heat transfer analysis at a greater level of detail.

The Lagrangian heat transfer formalism relies on the decomposition of the scalar field C into its conductive ($\widetilde{C}$) and convective (C') components following $C = \widetilde{C} + C'$. The evolution of the conductive and convective scalar fields are governed by

$$
\frac{\partial \widetilde{C}}{\partial t} = \frac{1}{Pe}\nabla^2 \widetilde{C},
$$
$$
\frac{\partial C'}{\partial t} + \nabla \cdot (\boldsymbol{u}C' - Pe^{-1}\nabla C') = -\boldsymbol{u} \cdot \nabla \widetilde{C},
$$

(4.9)

with the boundary conditions $\widetilde{C}|_\Gamma = 1$ and $C'|_\Gamma = 0$ and the initial conditions $\widetilde{C}(\boldsymbol{x},0) = 0$ and $C'(\boldsymbol{x},0) = 0$. The conductive component $\widetilde{C}$ is given by the analytical expression

$$
\widetilde{C}(r,t) = 1 - 2\sum_{m=1}^{\infty} \frac{J_0(\alpha_m r)}{\alpha_m J_1(\alpha_m)} e^{-\alpha_m^2 t},
$$

(4.10)

with $J_n(x)$ the nth Bessel function of the first kind and m the mth positive root of Bessel function $J_0(x)$. In this section, C represents the temperature field, yet the formalism can be applied to any advective-diffusive scalar field. The physical interpretation of the conductive and convective components is as follows:

- The conductive component $\widetilde{C}$ represents the temperature field without flow ($\boldsymbol{u} = 0$) and serves as a reference state for convective heat transfer. The governing transport equation for $\widetilde{C}$ in Eq.(4.9) represents then heat transfer by conduction only.

- The convective component C' comprises the impact of the fluid motion on the evolving temperature distribution. It meets the condition $\lim_{\boldsymbol{u}\to 0} C' = 0$ via the boundary condition $C'|_\Gamma = 0$. The quantity C' actually corresponds to the energy content of infinitesimal fluid parcels relative to the reference conductive state $\widetilde{C}$. The regions with positive convective component ($C' > 0$) have relatively higher energy content compared to the conductive state. These regions determine the so-called convective-heating zones. The regions with negative convective component ($C' < 0$) have relatively lower energy content than the conductive state and thus reveal convective-cooling zones.

The governing equation of C' (Eq.(4.9)) describes the energy transfer relative to the conductive state. Thus the proposed formalism specifically isolates the role of the fluid

flow (advection) in the total energy content, which is the main objective in many thermal-engineering problems (see Bejan (1995); Sunden and Shah (2007)). Essential in this context is that the reference state $\widetilde{C}$, as opposed to (in principle) arbitrary reference states for the total temperature C, is distinct and with a clear physical meaning. This renders C' (and any derived quantities) also physically unique and meaningful in thermal analysis.

The proposed decomposition admits further differentiation and interpretation. We can express the convective part in the generic transport form

$$\frac{\partial C'}{\partial t} + \nabla \cdot \boldsymbol{Q}' = F, \;\; \boldsymbol{Q}' = \boldsymbol{q}_c + \boldsymbol{q}', \;\; \boldsymbol{q}_c = \boldsymbol{u}C',$$

$$\boldsymbol{q}' = -\frac{1}{Pe}\nabla C', \;\; F = -\boldsymbol{u} \cdot \nabla \widetilde{C},$$

(4.11)

describing (changes in) the relative energy content C' of infinitesimal control volumes due to two fundamental thermal transport mechanisms: the internal energy generation/dissipation, denoted by F, and the energy exchange with the environment, denoted by the flux vector $\boldsymbol{Q}'$. Further physical interpretation of the quantities F and $\boldsymbol{Q}'$ is provided below.

The source F is the driving force for convective heat transfer, since a non-trivial C' can only be accomplished by non-zero F for given homogeneous initial/boundary conditions for C' (see Eq.(4.9)). This role of F is not specific to this particular case and naturally emerges from the decomposition for a whole range of practically relevant thermal boundary conditions, see Speetjens (2012) for details. Closed boundaries as in the 2D RAM case cause $\int_{\mathscr{D}} F dx dy = 0$. This implies zero net energy input by F, see Speetjens (2012). Net changes in the energy content are here induced indirectly through conduction along non-zero wall gradients: $\Delta q_{wall,flow} = q_{wall} - \widetilde{q}_{wall} = Pe^{-1}\partial C'/\partial r|_{\Gamma}$. The source F also relates to the conductive state $\widetilde{C}$, as can be seen as follows. Flow with temperature gradients $\nabla \widetilde{C}$ implies fluid parcels entering regions with relatively higher $\widetilde{C}$, signifying a relatively lower $C' = C - \widetilde{C}$ and, in consequence, a relative decrease in the convective energy content C'. Hence, the regions with higher $\widetilde{C}$ effectively act as heat sinks for the convective contribution C': $F = -\boldsymbol{u} \cdot \nabla \widetilde{C} < 0$. Conversely, flow against $\nabla \widetilde{C}$ effectively acts as a heat source for C': $F = -\boldsymbol{u} \cdot \nabla \widetilde{C} > 0$. Former and latter effects intimately relate to the before-mentioned convective cooling and heating processes, respectively.

The flux $\boldsymbol{Q}'$ represents the total redistribution of relative energy C' induced by the fluid motion and can be considered as a net convective flux. It becomes zero for stagnant fluid ($\boldsymbol{u} = 0$).

The flux $\boldsymbol{q}'$ constitutes the conductive component to $\boldsymbol{Q}'$ and accounts for the part of the total conductive heat flux $\boldsymbol{q} = -Pe^{-1}\nabla C = -Pe^{-1}(\nabla \widetilde{C} + \nabla C')$ due to gradients in the convective component C'. This involves the redistribution of energy C' over material regions by molecular diffusion.

The flux $\boldsymbol{q}_c$ constitutes the convective component to $\boldsymbol{Q}'$ and involves the redistribution of C' over flow regions by motion of fluid parcels (it thus represents a direct convective flux). Fluid parcels with $C' > 0$ increase the energy content at their momentary position relative to the conductive state and thus effectuate an energy influx (direct convective heating: $\boldsymbol{u} \cdot \boldsymbol{q}_c > 0$). Conversely, fluid parcels with $C' < 0$ locally decrease the relative energy content, resulting in an energy outflux (direct convective cooling: $\boldsymbol{u} \cdot \boldsymbol{q}_c < 0$).

4.3. Methodology

4.3.1. Numerical simulations

A finite element method (FEM) is used in Comsol Multiphysics 4.3b to solve 2D mass and momentum equations (Eq.(6.1)) and the advection-diffusion equation (Eq.(6.2)). An unstructured triangular grid is constructed with approximately 584000 nodes to maintain the numerical stability. The numerical convergence and accuracy is inspected by standard grid refinement tests. Integrations were performed with a second-order backward-difference scheme and implicit time-stepping. A relative tolerance of 10^{-3} is prescribed for the velocity components in the solver for the steady flow field, whereas an absolute tolerance of 10^{-3} (which corresponds to mK) is prescribed for the temperature field in the solver for the advection-diffusion equation.

Material curves in the limit of infinite Péclet number are determined by the tracking algorithms discussed by Malyuga et al. (2002). In the limit of infinite-Pe, the scalar transport is equivalent to passive advection so that the evolution of scalar fields can then be done by tracking only the iso-levels of scalar concentrations.

4.3.2. Experimental setup

A detailed description of the simplified RAM facility is given in Section 2.2. The current study utilizes both isothermal (for flow field measurements and dye experiments) and non-isothermal (for temperature field measurements) settings. The motor-driven belt systems are positioned oppositely on two apertures (offset angle $\Theta = 180°$) and aperture arc angle Δ is set to 45°. A time-periodic piecewise steady flow field is generated by sequential actuation of the two motor-belt systems (the belt velocity is fixed to 0.004 m/s) and τ is set to 10.

4.3.3. Measurement techniques

The main motivation of the experiments in this chapter is the investigation of the evolution of the flow field and scalar fields in time. This necessitates the implementation of three well-known optical visualization methods to the system: particle image velocimetry (PIV), infrared thermography (IRT) and dye visualization for the acquisition of the flow and scalar fields. The reader is referred to Section 2.4 for the implementation details of these methods.

4.3.4. Dynamic-mode decomposition analysis

Data processing and analysis is based on the dynamic mode decomposition (DMD). It is a mathematical method which aims to recover the actual eigenmode decomposition (Eq.(6.4)) from data at discrete time levels. It assumes that the subsequent time levels relate via a mapping:

$$\boldsymbol{c}_{n+1} = \mathscr{A}\,\boldsymbol{c}_n \tag{4.12}$$

where $\boldsymbol{c}_n$ denotes the scalar field in discrete partitions in the domain at time level $t_n = n\Delta t$ and $\mathscr{A}$ is a linear operator that maps a scalar field $\boldsymbol{c}_n$ to the consecutive one $\boldsymbol{c}_{n+1}$. The

eigenfunction-eigenvalue pairs of the mapping matrix $\mathscr{A}$ are the approximations for the eigenfunction-eigenvalue pairs $\{\varphi_k, \mu_k\}$ of the advection-diffusion operator $\mathscr{L}_2$. Moreover, DMD determines the approximate expansion coefficients γ_k. The details of the algorithm can be found in the studies by Schmid (2010, 2011).

4.4. COMPARATIVE ANALYSIS

In this section, results derived from the spectral analysis, experiments and numerical simulations are compared for a given set of parameters. The analysis concerns two fundamental cases of the configuration that is introduced in Section 4.2.1: a typical case at finite Péclet number (advective-diffusive transport) and the corresponding limit case at infinite Péclet number (advective transport). First, a qualitative comparison of the experimentally and numerically obtained flow fields is performed for the case of steady flow in the 2D RAM. Then, in the framework of the advective-diffusive transport case, the dominant eigenmode of the system is acquired by directly determining the eigenvalue-eigenfunction pairs of the advection-diffusion operator $\mathscr{L}_2$ using the method by Lester et al. (2008) which defines the benchmark solution for the analysis hereafter. Subsequently, DMD is applied on the experimental and numerical data to determine the dominant eigenmodes of the time-resolved data sets. For the infinite-Pe limit, in which diffusion is negligible, the experiments are done at isothermal conditions, i.e. the temperature field is replaced by a non-diffusive scalar field, and scalar transport is investigated in terms of the advection of material curves. Finally, convective heat transfer analysis is applied to the numerical data.

4.4.1. FLOW FIELD

This section contains a comparative analysis of numerical and experimental results from PIV measurements for the flow field of an isothermal fluid. This comparison gives insight in how well the flow field from numerical simulations agrees with experimentally obtained flow fields at the free surface of the shallow fluid layer. Additionally, it may shed light on possible inertial effects in the experiments and their relative importance. This analysis is performed for the steady flow driven by only one aperture. Before proceeding with the further analysis, it should be noted that the flow field from the numerical simulations is also compared with the analytic solution of the flow given in Hwu et al. (1997), which yields negligibly small differences between the two cases. Using Eq. 2.1 the deviation in the u-component, v-component and the magnitude of the flow field are found to be 0.0318, 0.0381 and 0.0242, respectively. The effect of the analytical versus numerical flow field on the temperature field is also analyzed and the results shows a good agreement (the deviation parameter given by Eq. 2.1 is 1.66×10^{-4}). Based on the insignificant differences between the numerical and analytical solutions, the temperature fields acquired from the analytical flow field are not shown in this chapter in order to avoid repetition of figures and for the sake of simplicity.

    The velocity fields and streamlines obtained experimentally via PIV measurements and computed numerically for the 2D flow problem are compared in Figure 4.2 and Figure 4.3. Figure 4.2 compares the contours of the velocity magnitude. Notwithstanding the small differences observed in velocity field contours, similar flow structures are captured both experimentally and numerically. The differences can be attributed to the presence

of weak inertia in the shallow fluid layer experiments and eventually weak 3D effects (although shown to be negligible in Section 2.2.1). The differences are particularly evident in the comparison of the streamlines (see Figure 4.3). However, the same structure composed of a stagnation point with concentric circular streamlines is observed in both cases. Hence, the streamline patterns are topologically equivalent.
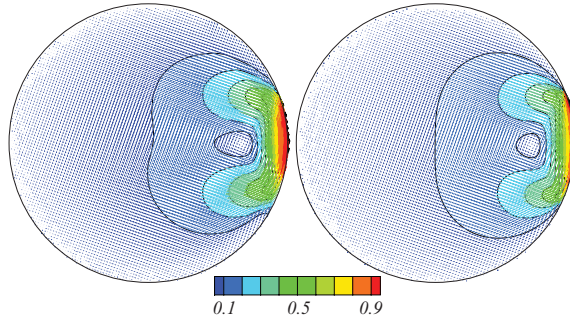

Figure 4.2: Dimensionless flow field generated by the right aperture is acquired experimentally (left panel) and numerically (right panel). The contours indicate the magnitude of the velocity.
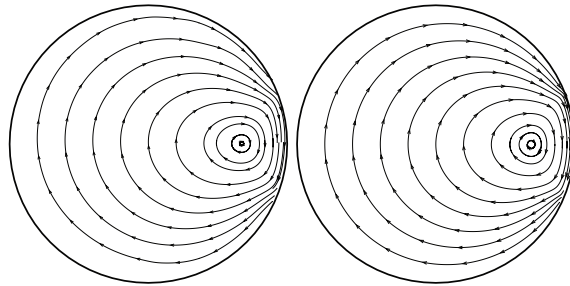

Figure 4.3: Streamlines obtained by the integration of the velocity field generated by the right aperture motion in experiments (left panel) and numerical simulations (right panel).
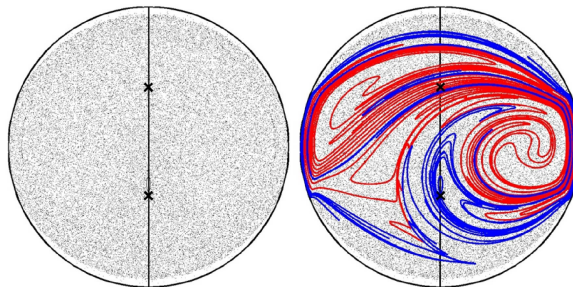

Figure 4.4: Poincaré section of two-window 2D RAM with period time $\mathcal{T} = 20$ including period-1 hyperbolic points (x) on the (black) symmetry axis (left) and unstable manifolds (red and blue curves are the unsteady manifolds of the upper and lower crosses, respectively) (right).

The advection properties of the simulated flow field for the configuration described in Section 4.2.1 is demonstrated by a Poincaré section in Figure 4.4 (left), which reveals global chaotic advection, except for a tiny island on the (black) symmetry axis. The crosses (x) on the symmetry axis are the hyperbolic period-1 points that return to their initial position after each period. The scalar transport is dominated by the unstable manifolds of these two hyperbolic period-1 points (red and blue curves in Figure 4.4 (right)). These manifolds delineate the asymptotic advection pattern of scalar fields in the infinite-Pe limit.

4.4.2. Advective-diffusive scalar transport at finite-Pe

The advective-diffusive transport at finite Péclet number is analyzed by experimental observations and numerical simulations for the configuration explained in Section 4.2.1. The ADE is numerically solved with Comsol for 100 periods to reach a fully homogeneous state. On the other hand, the experiment is performed for 50 periods beyond which the evolution of the temperature field is inherently terminated due to the heat balance in the tank. In the experiments, the evolution of the temperature field in the test section starts from an initially uniform distribution, and the data acquisition commences as heat is supplied at the lateral circular boundary. Within a few periods, the initially homogeneous temperature field transforms into a periodically persistent pattern and evolves self-similarly with increasing scalar intensities (Figure 4.5). The evolution of the temperature field in the numerical case is in close agreement with the evolution in experiments (see Figure 4.6). Significant differences occur only in the longer term in that the numerical field evolves into a homogeneous state, while the experimental field evolves into a non-uniform state due to the surface heat losses. The wall heat flux is strongest in the beginning and gradually diminishes over time due to the decaying temperature gradients at the wall. For $\tilde{\mathscr{T}} \gtrsim 10$ the wall heat flux then becomes too small to effectively compete against the adverse effect of the heat loss at the free surface (discussed in Section 2.2.1).

Figure 4.7 and Figure 4.8 illustrate the first few eigenmodes extracted via DMD from experimental and numerical time-resolved data sets, respectively. In the experimental case there are only two eigenmodes that can be extracted. The pattern in Figure 4.7 (left) is the dominant eigenmode of the experimental temperature field, which is consistent with the numerical dominant eigenmode (Figure 4.8 (top left)). The second dominant eigenmode of the experimental temperature field shows a great resemblance with the second dominant eigenmode of the numerical temperature field. However, when the magnitudes of the second dominant eigenmodes are compared to the magnitudes of the dominant eigenmodes, the second dominant eigenmode of the experimental temperature field is very weak to say that it is the experimental counterpart of the second dominant eigenmode of the numerical temperature field. This is due to the imperfections compared to 2D case (i.e. heat losses from the free surface) and the error in the infrared camera images.

For a comparative eigenmode analysis, the dominant eigenmode of the advection-diffusion operator $\mathscr{L}_2$ for $Pe = 10000$, $\tau = 10$, $\Theta = \pi$ is set as the benchmark solution and compared with the experimental and numerical eigenmodes. The application of the eigenmode analysis on the ADE allows us to obtain the long persistent pattern of the thermal evolution. Determination of the eigenvalue-eigenfunction pairs for $\mathscr{L}_2$ as explained in Section 6.2.2 reveals the persistent pattern in Figure 4.9 (left) as being the 'dominant eigenmode' with a non-dimensional exponential decay rate μ_0 of -0.00126 ± 0.00001 for
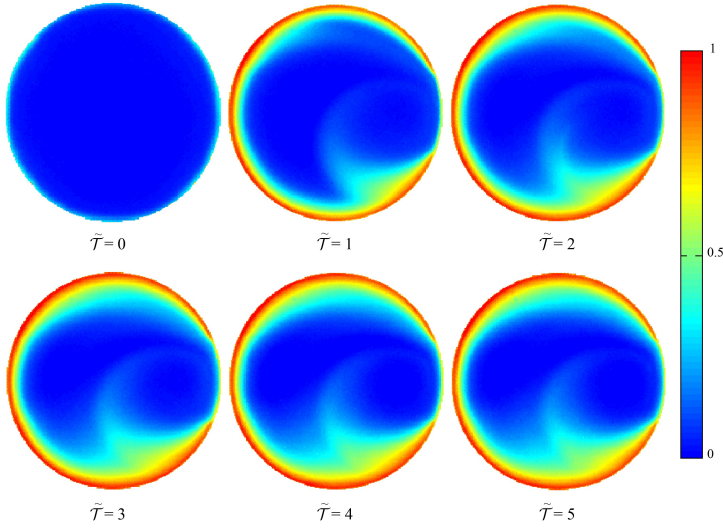
Figure 4.5: Snapshots of experimentally obtained temperature distributions at the free surface of the silicon oil. The color range from 0 to 1 (dimensionless temperature) is indicated from blue to red. The persistent thermal patterns are plotted for the dimensionless periods $\tilde{\mathcal{T}}$ from 0 to 5. One period represents 1250 s in the experiments, $Re = 0.1$, $Pe = 10000$, and $\tau = 10$.
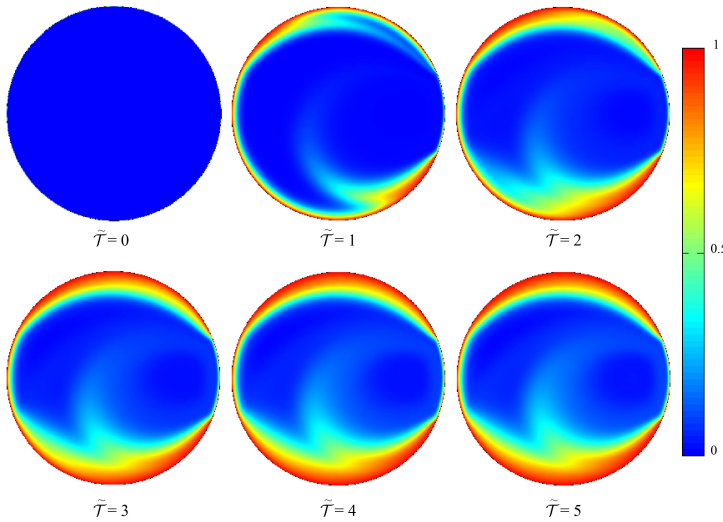

Figure 4.6: Snapshots of numerical temperature distributions. The color range from 0 to 1 (dimensionless temperature) is indicated from blue to red. The persistent thermal patterns are plotted for the dimensionless periods $\tilde{\mathcal{T}}$ from 0 to 5. $Re = 0$, $Pe = 10000$, and $\tau = 10$.

the case of interest. In all three results shown in Figure 4.9 similar spatial structures are observed where the spectral method unavoidably gives the highest degree of detail. Despite
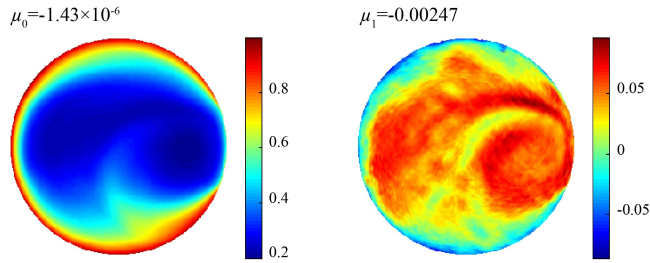
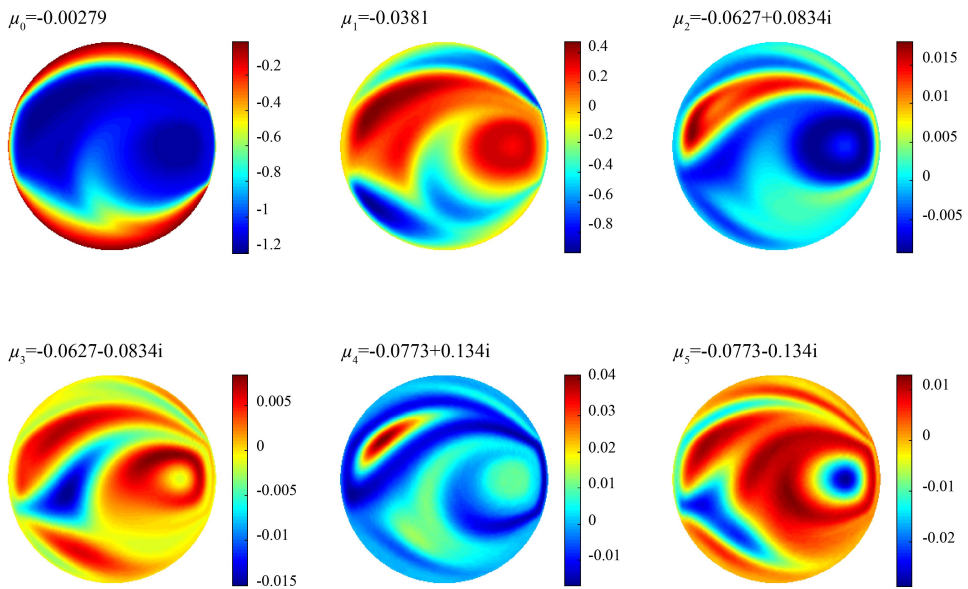Figure 4.7: Leading eigenmodes of the experimental data set for $Pe = 10000$, $\tau = 10$ and $Re = 0.1$.

Figure 4.8: Leading eigenmodes of the numerical data set for $Pe = 10000$, $\tau = 10$ and $Re = 0$.

the good agreement in the dominant eigenmodes, the exponential decay rates μ_0 of the different methods shows incongruity. Comparison of the decay rates found via simulation and spectral method shows that this is somewhat higher for the former. This is due to the fact that discretization introduces numerical diffusion and thus artificially increases the homogenization rate in the simulations. This numerical diffusion also smears out the fine structures in the scalar field, explaining why it reveals less detail compared to the spectral method. The decay rate of the experimental analysis is $\mu_0 = -1.43 \times 10^{-6}$ and differs substantially from those of the simulation and the spectral method. This is due to the fact that the steady-state eigenmode (corresponding to vanishing eigenvalue $\mu_k = 0$) of the experimental system is different from that for the ideal system described by the simulations

and the spectral method. The steady state of the ideal system corresponds to a trivial uniform eigenmode, meaning that eigenmode φ_0 is in fact the first non-decaying eigenmode (hence $\mu_0 < 0$). For the experimental system, on the other hand, weak surface heat losses cause eigenmode φ_0 to become the non-uniform steady state (hence $\mu_0 \approx 0$).
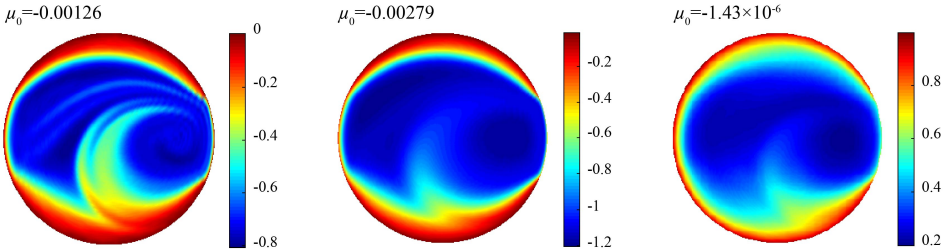

Figure 4.9: The theoretical dominant eigenmode acquired by the spectral analysis of the ADE (left), the dominant eigenmodes of the numerical simulations (middle) and the experiments (right) for the case with $Pe = 10000$, $\tau = 10$ and $Re = 0$ (in experiments $Re = 0.1$). The values on top of the figures are the decay rates μ_0. DMD is applied on numerical and experimental data sets to obtain the dominant eigenmodes.

The variance of the temperature distribution decreases exponentially in time as shown in Figure 4.10 (left) for the numerical experiment as the system works to reach a homogeneous temperature distribution eventually. However, the decay is different in the experimental case as depicted in Figure 4.10 (right) due to the fact that the heat loss in the system results in a different exponential decay rate (as explained above). The error bars are calculated based on the accuracy of the infrared camera.
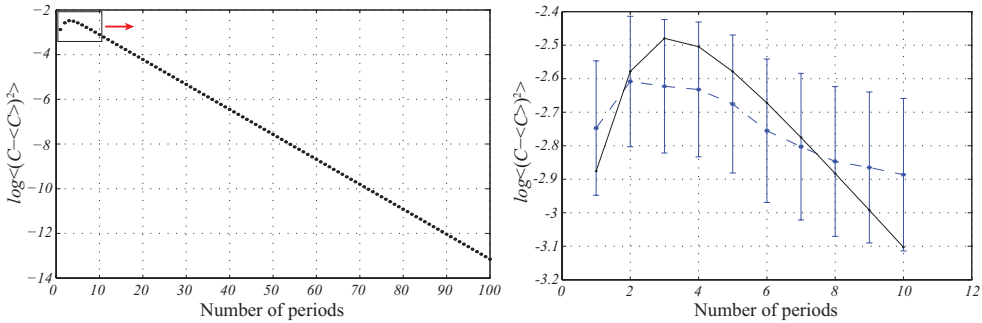

Figure 4.10: The change of the variance of the numerical temperature field with time: linearity in the logarithmic plot shows the exponential decay of the variance (left). An enlargement of the top-left part is shown in the right panel, together with the change of the variance of the experimental temperature distribution with time (blue dots). The error bars are calculated based on the accuracy of the infrared camera.

As discussed above, the dominant eigenmode is a period-1 eigenmode of a finite-Pe case (period-1 eigenmode implies that $\omega_0 = 0$ and finite-Pe causes $\mu_0 = \sigma_0 < 0$), where the spatial pattern namely decays self-similarly: $C(\boldsymbol{x}, (n+1)\mathscr{T})/C(\boldsymbol{x}, n\mathscr{T}) = e^{\mu_0 \mathscr{T}}$. In the case of infinite-Pe limit, however, the period-1 eigenmode does not decay anymore, i.e.

$C(\boldsymbol{x}, (n+1)\mathscr{T})/C(\boldsymbol{x}, n\mathscr{T})$
$= 1$, since $\mu_0 = \sigma_0 = 0$. The details of infinite-Pe case is discussed in the next section.

4.4.3. ADVECTIVE-DIFFUSIVE SCALAR TRANSPORT IN THE LIMIT OF INFINITE-PE

The evolution of the initially inhomogeneous scalar field toward an asymptotically mixed state is examined in the limit of infinite-Pe for $\tau = 10$ and $\Theta = \pi$ case, both numerically and experimentally. Initially, the domain is composed of two equally-sized regions colored in black and white. After a few stretching-folding cycles the scalar field evolves into a complex structure. The pattern as a whole remains fixed (as expected for period-1 structures) yet contains more detail.

This case is an example of global chaotic advection where the unstable manifolds of the hyperbolic period-1 points (Figure 4.4) determine the asymptotic mixing pattern corresponding with an eigenmode of period-1 which is non-decaying, i.e. $\mu_0 = 0$ (see Gorodetskyi et al. (2014)). The scalar field exponentially converges on this pattern independently of the initial distribution. Chaos causes a very complicated mixing pattern and thereby a very complicated spatial structure of the eigenmode. In other words, this pattern is a 'strange' eigenmode.

The numerical and experimental visualizations of advection of this scalar field (Figure 4.11 and Figure 4.12) show how the initial scalar concentration quickly approaches the asymptotic mixing pattern - and thereby the period-1 strange eigenmode. This reveals the quick emergence of a mixing pattern that closely correlates with the manifold structure in Figure 4.4. It is important to note that after only 2 periods, detailed features of the dye distributions and manifolds are in close agreement.
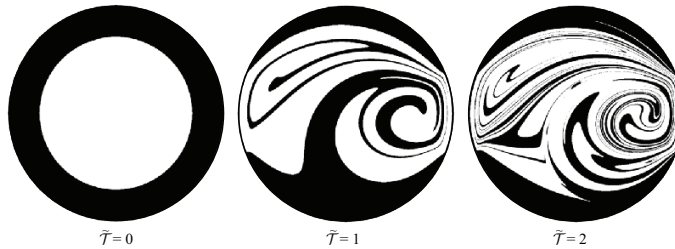

$\tilde{\mathscr{T}} = 0$ $\tilde{\mathscr{T}} = 1$ $\tilde{\mathscr{T}} = 2$

Figure 4.11: Simulated advection of initial disk of passive scalar for $\tau = 10$.

Numerical tracking of the dye for more than 2 periods is computationally extremely expensive. However, this is not a problem in the experiments, which indicates that there is a clear advantage of the experimental studies over numerical simulations for these particular aspects.

The experiments at some point always suffer from diffusion, no matter how weak, due to the extreme concentration gradients that develop over time. This causes gradual blurring and in the end vanishing of the details of the small-scale features, which is particularly visible at $\tilde{\mathscr{T}} = 20$ in Figure 4.12. Yet, the overall shape of the internal region (the black-white region made of stretched-folded material lines and enclosed by the black re-
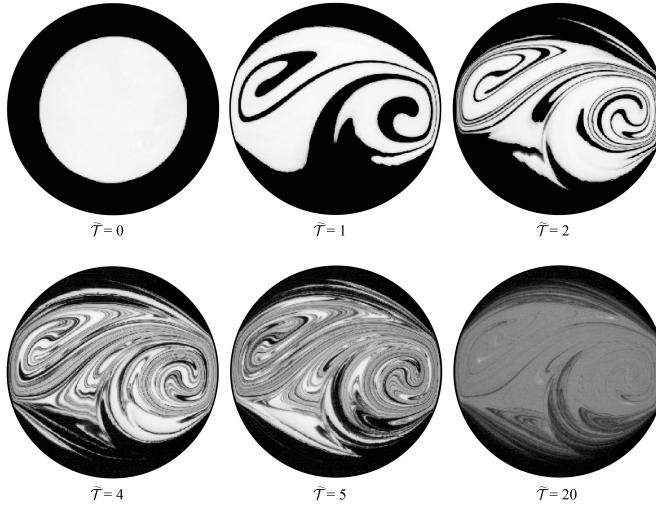
Figure 4.12: The evolution of scalar patterns in the limit of infinite-Pe. Parameter settings: $Re = 0.1$ and $\tau = 10$.

gion near to the stationary walls of the domain) remains intact and continues to correlate well with the distinction between red and blue regions in the finite-Pe dominant mode (Figure 4.6 and Figure 4.12). The longer-term dye patterns thus still have a physical meaning by in fact visualizing the finite-Pe dominant eigenmode for very high (yet finite) Pe. A similar case is studied by Gorodetskyi et al. (2014), where numerical diffusion is exploited to emulate diffusion at extreme Pe. The dominant mode of the finite-Pe case at more moderate Pe can therefore be seen as a smeared-out version of the infinite-Pe case. The lower the Péclet number is, the more blurred the features in the mixing pattern become.

The fact that the location and shape of the black regions in the dye patterns in all cases correlate well with the red regions in the finite-Pe mode has a clear physical message. It namely implies that transport in the black (red in finite-Pe case) region is basically independent of Pe, meaning that here advection is irrelevant, or conversely, that diffusion dominates. The primary effect of growing Pe on the dominant eigenmode is the greater spatial complexity that develops in the internal region enclosed by the diffusive (black) region near to the wall. The infinite-Pe limit of that internal structure is then the asymptotic mixing pattern due to the unstable manifolds. Conversely, the internal structure at finite-Pe is basically a smeared-out version of the asymptotic mixing pattern.

4.4.4. THERMAL ANALYSIS

For the analysis of the effect of fluid motion on the thermal process in the 2D RAM, the temperature field is decomposed into the conductive and convective contributions. The total temperature C is simulated using Comsol Multiphysics 4.3b (Section 4.3.1); the conductive component $\widetilde{C}$ is the axisymmetric analytical solution of 1D diffusion equation for a cylindrical domain given by Eq. 4.10. The difference between the total temperature field and the conductive component is the convective component C' that represents the effect
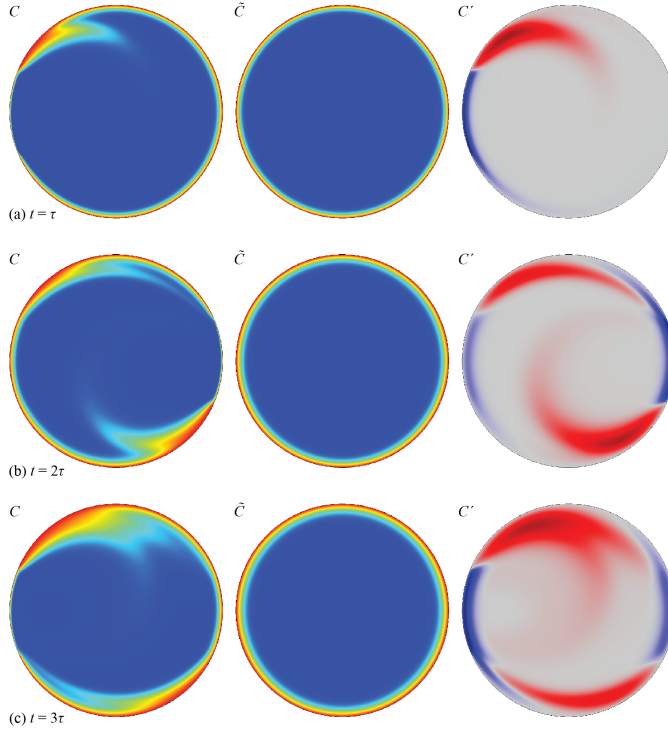
of fluid motion on the thermal energy content.

Figure 4.13: Temperature decomposition after the first three activations of the windows: left-right-left. Color code C and $\tilde{C}$: blue (0) - red (1); color code C': blue (min $C' < 0$) - gray ($C' = 0$) - red (max $C' > 0$).

The instantaneous temperature decomposition after the first three activations of the windows is shown in Figure 4.13. The sequence of window activation is left-right-left. The comparison of the total temperature field C (left) and the conductive component $\tilde{C}$ (middle) shows the influence of the advection on the temperature distribution. Warm fluid patterns (red in Figure 4.13 (right)) separate from the upper edge of the left window ($t = \tau$) and lower edge of the right window ($t = 2\tau$) during the subsequent activations of the apertures and enter the cold interior region (blue). Consecutive window activations arouse this window-wise plume formation in a manner analogous to a periodically kicked pendulum. The cold regions localized at the windows in the convective component C' (right) display the cold fluid parcels entering warm region. Thus C' exposes that the fluid motion indeed causes two simultaneous processes: the transport of relatively warmer fluid from the wall into the interior (convective heating) and the transport of relatively colder fluid from the interior toward the wall (convective cooling). Both processes contribute to the heat-transfer enhancement: the former increases the interior energy content far more rapidly than by conduction alone; the latter amplifies the heat influx from the wall by steepening the temperature gradient at the windows. The additional local influx (compared to the conductive state) is $q'|_\Gamma = -Pe^{-1}\partial C/\partial r < 0$ due to $C'|_\Gamma = 0$ and $C' < 0$ in the adjacent cold

region. The warm fluid parcel partially prevents the additional window influx by locally reducing the wall temperature gradient upstream of the windows. The flow nonetheless accomplishes a net energy increase and thus heat-transfer enhancement. The rapid heat take-up from the wall to the interior continues for a prolonged period of time until the interior has undergone a substantial temperature/energy increase. When the fluid drawn into the window regions becomes insufficiently sub-cooled for appreciable wall temperature gradients, the heat take-up from the wall decelerates. This causes gradual decay of the convective cooling zones, as demonstrated in Figure 4.14, and, in consequence, breakdown of heat-transfer enhancement.
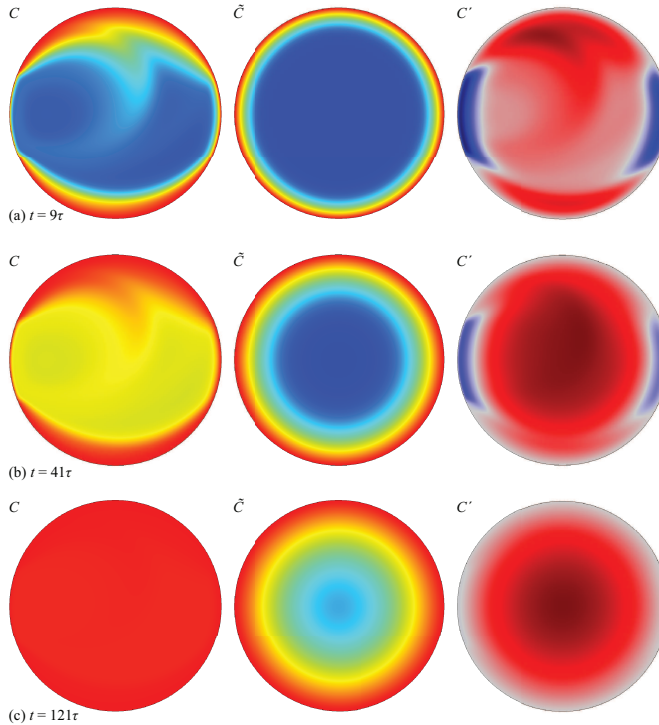

Figure 4.14: Temperature decomposition for typical time instances during the transient towards the homogeneous state. Color code C and $\widetilde{C}$: blue (0) - red (1); color code C': blue (min $C' < 0$) - gray ($C' = 0$) - red (max $C' > 0$).

In addition to the decomposition of the temperature field into its conductive and convective components, the convective component C' is decomposed into its eigenmodes to compare the spectrum of the scalar field C to the spectrum of the convective component C'. Figure 4.15 shows the eigenmode decomposition of the convective component C', where the top left pattern is the dominant eigenmode of C' and is consistent with the evolving pattern in Figure 4.13 and Figure 4.14 (right column). The dominant eigenmode of C (Figure 4.8 (top left)) also appears in the spectrum of C' as a decaying mode with the same decay rate. The reason is that the advection mode is the driving mode

μ_0=-0.000578 μ_1=-0.00279 μ_2=-0.00304

μ_3=-0.00747 μ_4=-0.0138 μ_5=-0.0221

μ_6=-0.0322 μ_7=-0.0381 μ_8=-0.0442

μ_9=-0.0576 μ_{10}=-0.0627+0.0834i μ_{11}=-0.0627-0.0834i
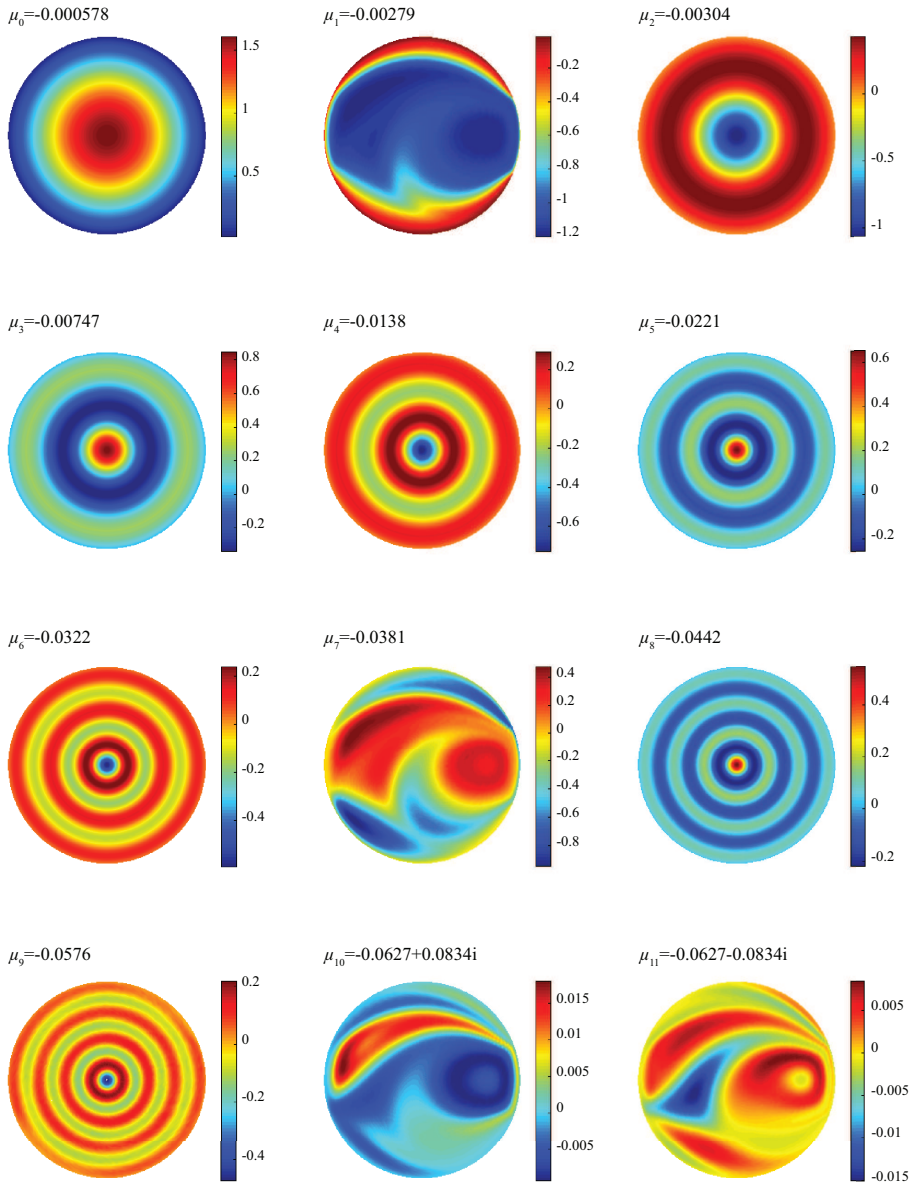
Figure 4.15: Leading eigenmodes of convective component C' for $Pe = 10000$, $\tau = 10$ and $Re = 0$.

for the displacement of the heat and the mode decays as the temperature field becomes homogeneous. The second, third and fourth dominant eigenmodes of C can be seen in the spectrum of C' with the same decay rates. The remaining axis-symmetric modes of

C' correspond with the modes of $\widetilde{C}$ due to the fact that $C' = \sum_m \gamma'_m \varphi'_m e^{\mu'_m \mathcal{T}} = C - \widetilde{C} = \sum_k \gamma_k \varphi_k e^{\mu_k \mathcal{T}} - \sum_n \widetilde{\gamma}_n \widetilde{\varphi}_n e^{\widetilde{\mu}_n \mathcal{T}}$, i.e. the spectrum of C' comprise both modes from C and $\widetilde{C}$ due to the superposition in $C' = C - \widetilde{C}$. Component C' namely after all represents the effect of fluid motion on the heat transfer and its modal structure may offer further insight into the fundamentals of convective heat transfer.

4.5. Conclusion

This study concerns a comparative analysis on the evolution of advective-diffusive scalar transport by experimental and numerical analysis in a simplified model of the RAM. Cross-sectional evolution of flow and temperature fields of the RAM was modeled in an experimental setup that consists of a circular test section with an annular hot water reservoir and alternatingly actuated belts at apertures positioned on the circumference of the test section (a configuration which is denoted as the 2D RAM). PIV was implemented to acquire time-resolved velocity fields and IRT was used to assess evolution of temperature fields in time. To visualize the evolution of a concentration field in the limit of infinite-Pe dye visualization experiments were conducted. Commercial multiphysics solver Comsol 4.2a was used to compute the velocity and temperature fields in a two-dimensional circular domain with appropriate initial and boundary conditions. A comparative analysis was performed on the velocity/scalar fields derived from experiments and numerical simulations. 3D inertial effects in experiments are mild so that similar flow/scalar field structures are observed.

The importance of the eigenmode analysis is its capability to reveal the persistent structures dominating the scalar field evolution. For a comparative eigenmode analysis, the ADE is spectrally decomposed into its eigenvalue-eigenfunction pairs and the dominant eigenmode with the slowest decay rate is set as the benchmark pattern. DMD is applied on the experimentally and numerically obtained temperature fields to obtain the dominant eigenmodes of the evolution. In general, a good agreement is observed between the dominant eigenmodes of the ADE and the DMD analysis on the experimental and numerical data sets. A quantitative analysis of the scalar field confirms that when diffusion is effective, self-similarly decaying patterns dominate the scalar field evolution and the evolution can be simplified to a spatial structure and a decay rate pair which has the slowest decay rate. The onset of the permanent pattern is due to the convergence of the scalar field to the dominant eigenmode of the advection-diffusion operator in closed flows. In the limit of zero-diffusivity the self-similarly decaying structure turns into a complex spatial structure with non-decaying gradients and increasing complexity. The methods and tools employed in this study validate the eigenmode approach and the results of different methods support each other. Nonetheless, each method has its own advantage(s) and restriction(s) which are summarized in Table 4.1.

The thermal analysis presented in the current study investigates convective heat transfer from an alternative perspective. The advantage of the analysis is its capability to explicitly isolate and visualize the energy redistribution and energy fluxes induced by the flow. This facilitates a more direct description and analysis compared to conventional methods based on integrated values and wall heat-transfer coefficients. The convective component C' directly exposes a key element of convective heat transfer: the formation of

	Advantages	Restrictions
Eigenmode analysis	Gives the highest degree of detail. Computationally cheaper than the numerical simulations at Pe=10000	In the limit of infinite-Pe it becomes computationally expensive.
Numerical simulations and contour line tracking	Easy setup of the model configuration Allows to study both ideal and physical configurations to assess the effects of non-ideal conditions (temperature-dependence of material properties, inertial flow effects, etc.)	The discretization smears out the fine structures and increases the homogenization rate.
Experimental observations	Reliable long-term experiments in the limit of infinite-Pe	Unavoidable heat losses Mild 3D effects

Table 4.1: The summary of the advantages and the restrictions of the methods used in the current study

so-called convective-cooling/heating zones inside the domain due to the transfer of relatively colder/warmer fluid into certain flow regions. These zones enhance heat transfer in two ways: heating zones increase the interior energy content far more rapidly than by conduction alone; cooling zones augment the heat influx from the wall by steepening the temperature gradient. This reveals that enhanced heat transfer is accomplished by a cyclic fluid exchange between convective-cooling zones (which form at specific segments of the hot wall) and the interior. The alternative approach employed here is in fact part of a larger framework, see Speetjens (2012).

The experimental methods and tools used in the current study are promising for further investigation of the mixing characteristics of the RAM for different configurations. Despite the heat losses in the temperature field experiments, the results of the concentration (dye) and temperature field experiments show similar characteristics: the evolution is dominated by a persistent pattern overall structure of which is the same in both cases. However, the dye (infinite-Pe limit) experiments give more detailed information on the complex spatial structure of the repeating pattern. Relying on the results obtained in the current study, in the next chapter, an experimental analysis on the mixing characteristics of the actual RAM is conducted via exploring the response of the simplified 2D RAM to changing parameters, i.e. a parameter-regime study of the 2D RAM that deepen insight into the mixing characteristics of the actual RAM, qualitatively.
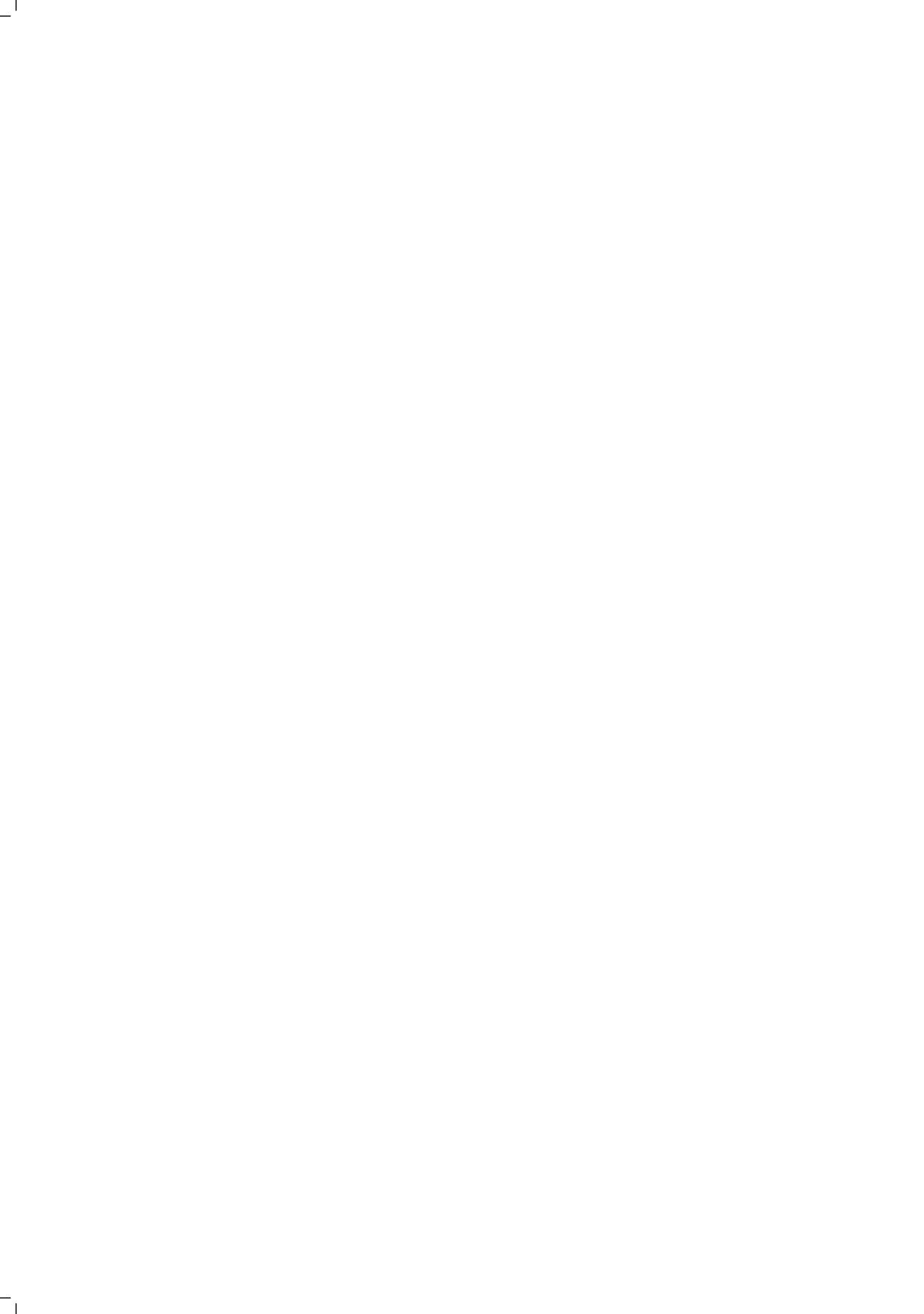
5

PARAMETRIC ANALYSIS OF A REORIENTED DUCT FLOW

This study concerns a coupled experimental-numerical analysis of scalar transport in reoriented duct flows found in industrial mixing processes. To this end the study adopts the Rotated Arc Mixer (RAM) as the representative configuration. The focus is on the effects of geometrical (i.e. reorientation angle Θ) and temporal (i.e. reorientation frequency τ) parameters of generic inline mixing devices on the Lagrangian particle dynamics and scalar field evolution. Lagrangian dynamics are investigated by constructing Poincaré sections from analytic flow solutions and stroboscopic measurements of particle positions in 2D RAM laboratory setup. In order to obtain the optimal mixing and homogenization of scalar fields, dye visualizations are performed for an extensive set of parameters. The mixing quality in parameter space is quantitatively evaluated by means of the intensity of segregation. These results are used to determine the optimum forcing protocol. The outcome of this study validates the qualitative agreement in mixing characteristics of 2D time-periodic and 3D spatially-periodic flows and confirms the good mixing performance found before for certain RAM configurations. Moreover, we demonstrate that even more efficient protocols can be devised by suitably tuning the sequence of the reorientation angle. This knowledge might eventually lead to optimized 3D reoriented duct flow mixers.

5.1. Introduction

Scalar advection in reoriented duct flows is an active area of research due to their particular relevance to continuous industrial mixers such as the Kenics mixer (Galaktionov et al., 2003; Thakur et al., 2003), SMX mixer (Thakur et al., 2003) and the Rotated Arc Mixer (Metcalfe et al., 2006), to microfluidic lab-on-a-chip diagnostic devices, and to the bulk manufacturing of fine chemicals. The flow in these configurations can be characterized by three common features: (i) a continuous throughflow; (ii) a transverse flow generated by internal elements or moving boundaries; (iii) systematic reorientation of the flow along the duct axis (Speetjens et al., 2006). The interplay between the axial and transverse flow, which is controlled by a set of parameters, determines the state of the mixing. In this respect, it is of importance to deepen insight into the effects of these control parameters on the mixing efficiency.

This study adopts a 2D simplified Rotated Arc Mixer (RAM) as a representative configuration. The simplification relies on the fact that the downstream progression of reoriented duct flows in axial direction is dynamically similar to evolution in time, implying 3D spatially-periodic flows can be well represented by 2D time-periodic flows. This approach is common in the analyses of reoriented duct flows (Gorodetskyi et al., 2014; Speetjens et al., 2006; Stroock and McGraw, 2004). Likewise, the 3D steady scalar transport in spatially-periodic systems can be transformed into 2D time-dependent systems assuming that the axial diffusion is negligible (Lester et al., 2014). In a practical context, the simplified cases retain the fundamental kinematic properties and deviate from the real 3D cases quantitatively, which validates the suitability of the simplified approaches for qualitative mixing analyses (Speetjens et al., 2014) (including parameter studies).

In this context, this chapter aims to investigate the influence of geometrical (i.e., reorientation angle) and temporal (i.e., reorientation frequency) parameters of the RAM on the evolution of advective-diffusive scalar transport and the flow topology. To achieve this, three different approaches are followed: (i) the Lagrangian flow topology is investigated by means of an analytical solution of the 2D RAM flow; (ii) experiments are performed to analyze the Lagrangian flow topology via direct measurements of Poincaré sections; (iii) transport of scalars is investigated experimentally via dye visualizations. The analytical solutions are used to assess the characteristics of the flow topology in a general manner in a wide parameter space and thus enables construction of a regime diagram. Two complementary methods, Poincaré sections and dye visualizations, are employed experimentally to deepen insight into the Lagrangian transport. The advantage of the experiments over the numerical simulations is that long-term evolution of the scalar fields can be investigated; numerically this is very challenging, if not impossible, due to the complex structure of the scalar field patterns. As 2D RAM has characteristics which are generic to all 3D reoriented duct flows, this parametric study provides valuable information regarding the optimization of the reorientation angle and frequency to enhance the mixing quality in actual systems.

5.2. PROBLEM DEFINITION

The geometrical control parameter of the 3D RAM is the offset angle Θ, whereas the temporal parameter is the ratio of axial to transversal time scales $\beta = \Omega L / U_{\mathrm{mean}}$, where Ω is the angular velocity of the rotating outer cylinder, L is the axial length of cells and U_{mean} the mean axial velocity. In the 2D case, β simplifies to $\tau = \Omega T = T/T_f$, where T is the dimensionful time of one aperture activation and $T_f = R/U$ the typical flow time scale with U the velocity of arcs and R the radius of the domain. In the current study, the experiments are performed for a total of eight Θ values and five τ values for each Θ case. 2D time-periodic flow is accomplished by successive activation of p arcs, resulting in $\mathcal{T} = p\tau$ as total period time, where offset Θ is chosen such that $p\Theta = m2\pi$ with m an integer. The full parameter set consist of parameters Θ, τ, $Pe = \Omega R^2/D$ and $Re = \Omega R^2/\nu$, where Pe is the Peclét number with D the material diffusivity and Re is the Reynolds number with ν the kinematic viscosity. However, investigation of the effects of Re and Pe are beyond the scope of this study which is limited to the flow regime at the Stokes limit ($Re = 0$) and the scalar transport in the advective limit ($Pe^{-1} \approx 0$). Theoretical studies of non-zero Re and finite Pe on the RAM flow are given in the works by Speetjens et al. (2014) and Lester et al. (2007), respectively.

5.3. EXPERIMENTAL PROCEDURE

A detailed description of the simplified RAM facility is given in Section 2.2. The current study utilizes the isothermal (for flow field measurements and dye experiments) settings. The experiments are performed with two different numbers of apertures but with all apertures having the same opening angle $\Delta = \pi/4$ (Fig. 5.1a and b). In the first setup, there are 4 apertures which allows the investigation of four different Θ cases (Table 5.1). This is achieved by changing the activation sequence of the apertures. For instance, activation $A1$-$A2$-$A3$-$A4$ results in $\Theta = \pi/2$, whereas $A1$-$A3$ gives $\Theta = \pi$. The second setup consists of five apertures that are also activated in different orders to generate another four Θ cases (Table 5.1). In all cases the aperture belts rotate in the positive θ (counterclockwise) direction, and so positive Θ means activating apertures (belts) in a counterclockwise sequence and negative Θ means activating apertures in a clockwise sequence. The measurements for each Θ case are performed for $\tau = 0.1, 1, 2, 5$ and 10.

Activation order	Offset angle Θ (rad)
$A1$	2π
$A1$-$A3$	π
$A1$-$A2$-$A3$-$A4$	$\pi/2$
$A1$-$A4$-$A3$-$A2$	$-\pi/2$
$B1$-$B2$-$B3$-$B4$-$B5$	$2\pi/5$
$B1$-$B5$-$B4$-$B3$-$B2$	$-2\pi/5$
$B1$-$B3$-$B5$-$B2$-$B4$	$4\pi/5$
$B1$-$B4$-$B2$-$B5$-$B3$	$-4\pi/5$

Table 5.1: Activation orders and corresponding angular offset values Θ for the two experimental RAM configurations. A stands for the configuration with 4 apertures, whereas B stands for the configuration with 5 apertures.
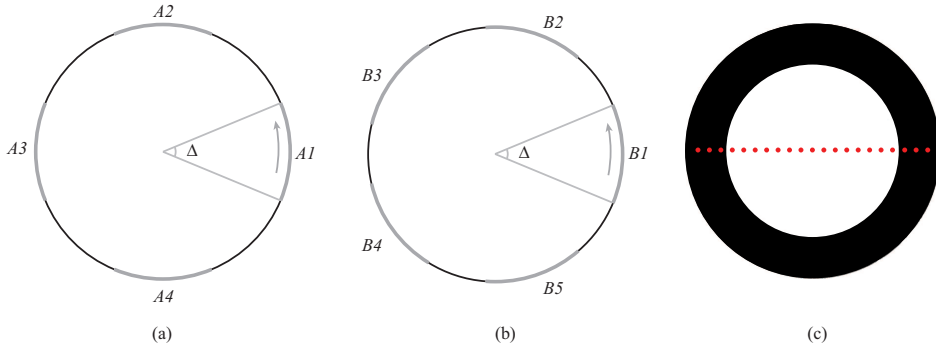
Figure 5.1: 2D RAM configurations: (a) the case with 4 apertures (gray), (b) the case with 5 apertures (gray); (c) initial condition for the scalar field (dye in black and white colors) and particle positions. Particle initial conditions are the centers of the red circles. Note that the actual tracer particles are much smaller than the circles.

For the scalar field experiments, the Peclét number is assumed to be in the limit of infinity. In a short term, the assumption of infinite-Pe holds, whereas in a long term, there may appear gray regions implying a finite-Pe albeit still having large values. This is due to the fact that as the scalar field evolves the order of striation thickness reduces exponentially at the rate of the Lyapunov number λ. Therefore, for any scale size a, the scale size starts to blur at a time $t_{\text{blur}}(a)$ that depends on a. Because the initial striation size is the same order as the tank size, we could express $t_{\text{blur}}(a) \sim \lambda^{-1} \ln[Pe/Pe_{\text{b}}(a)]$, where Pe is the usual Peclét number and $Pe_{\text{b}}(a)$ is a local Peclét number that uses the scale size a as the length. If Pe is really infinite, then t_{blur} is also infinite and no length scale no matter how small is ever blurred by diffusion. But if Pe is finite, no matter how large, then some maximum scale a will become blurred during the duration of the experiment. Over the duration of the experiments, diffusion exists yet it only affects smaller length scales justifying the assumption of infinite-Pe (for an illustration from the present experiments, see Fig. 5.11).

Scalar field and particle position measurements are performed concurrently to allow the assessment of the correlation between the Poincaré maps and scalar fields. For the analysis of scalar transport in the limit of infinite-Pe, dye visualization is utilized. For creation of the initial conditions (Fig. 5.1c), the tank is divided into two regions by placing a cylindrical tube concentrically in the circular tank. The radius R_{in} of the tube is chosen such that the inner and outer regions of the tube have the same area, thus $R_{\text{in}} = \frac{\sqrt{2}}{2} R$. The inner region of the tube is filled with silicone oil colored by white dye whereas the outer region is colored by black dye, which, after the removal of the cylindrical tube, serves as the initial condition for infinite-Pe experiments. The use of white dye together with black dye in the experiments improves the contrast of the images and allows having a proper calibration.

The evolution of the scalar patterns is captured by an AVT Pike F145B CCD camera placed above the test section. The 12-bit gray scale images have a resolution of 1388×1038 pixels and can distinguish $2^{12} = 4096$ gray levels. In order to obtain the relation between the camera intensity values and dye concentrations, a calibration is performed

before the measurements. To this end, six silicon oil samples are prepared by using various amount of white and black dye mixtures. Images of these samples are then recorded by the CCD camera (Fig. 5.2, top). A total of 100 images for each case are recorded and averaged to eliminate the effects of random noise on the resultant intensity values. Then, the mean of the averaged images is calculated to find the mean intensity value for each mixture. This is performed for three different shutter times of the CCD camera, viz., 2.5, 3 and 3.5 ms.
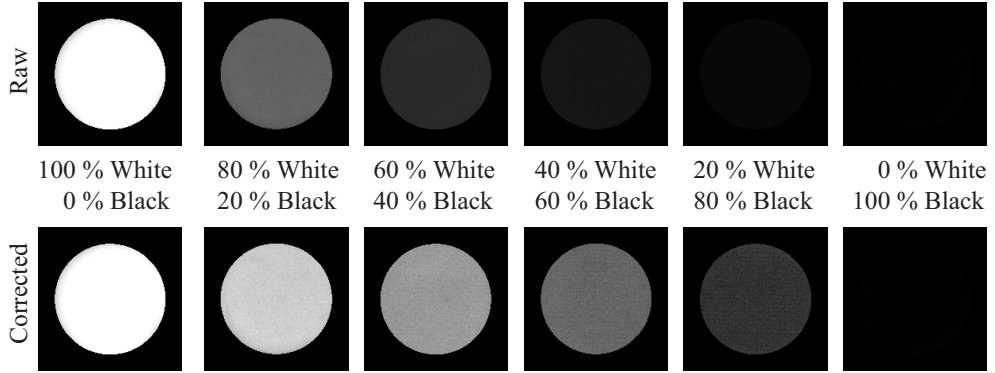
Figure 5.2: Camera images of mixtures with different white and black paint concentrations (top), images with corrected intensity values that vary linearly with the white paint concentration.

The mean intensity values for different concentrations of the dye mixture are plotted in Fig. 5.3. The intensity varies quadratically with increasing white dye percentage. Moreover, increasing camera exposure time results in the increase of intensity values for a given white dye percentage as expected. For the longest exposure time, the image is completely saturated for the case of 100 % white dye composition. For this reason, the images are recorded at a camera exposure time of 3 ms in the experiments. Subsequently, the intensity values of the images are corrected based on the calibration curve data to attain a linear relation between the dye composition and intensity values. In this way, the regions with low white dye concentration are better resolved and visualized (see Fig. 5.2, bottom).

The dye transport can be considered as non-diffusive, in the limit of infinite-Pe, however, due to stretching-folding and shear mechanisms, very fine-scale filaments and extreme concentration gradients may form in the course of time which promotes molecular diffusion. This causes gradual blurring and in the end vanishing of the small-scale features.

Direct measurement of the Poincaré sections is achieved by combining the successive positions of tracer particles in exactly the same way as numerical Poincaré sections are attained. To this end polystyrene foam particles (diameter $d_p = 1.5$ mm and density $\rho_p = 500$ kg/m^3) are released on the free surface of the top layer at the beginning of the experiment as shown in Fig. 5.1(c) ($\rho_p < \rho_{\text{silicon oil}} = 970$ kg/m^3 ensures they remain floating throughout the experiment). The typical response time of particles to changes in velocity is estimated at $\tau_p = d_p^2 \rho_p / 18 \rho \nu = 6.4$ μs, which is negligible compared to the typical flow time scale $T_f = R/U = \Omega^{-1} = 50$ s, meaning they are indeed passively advected by the flow. In total 21 particles are positioned equidistantly along the diameter aligned with the mid-
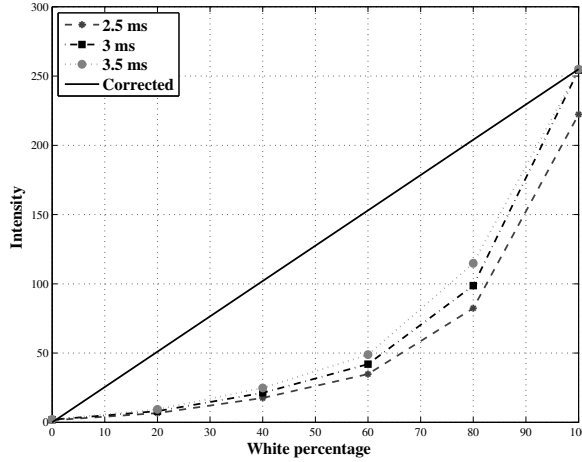
Figure 5.3: Variation of mean camera intensity values with respect to white paint concentration of the mixture for different camera exposure times and the resultant corrected variation that changes linearly with the white paint percentage (black line).

point of the aperture $A1$ or $B1$ (this is done right after the preparation of the initial condition for scalar field experiments) and their subsequent positions (together with scalar patterns) after each period are recorded by the CCD camera. The particle positions are determined from the imagery to sub-pixel accuracy by a dedicated particle-detection code implemented in the high-level programming language MATLAB and combined into experimental Poincaré sections. Note that detection of particles suffices to construct Poincaré sections; actual tracking of individual particles is unnecessary. One pixel corresponds to approximately 0.5×0.5 mm^2, meaning that an individual particle covers about 3×3 pixels^2, which ensures reliable detection of the particle location. Experiments are run for 250 periods in all cases.

5.4. Poincaré sections: results of numerical simulations

This section discusses the Lagrangian topology of the 2D RAM for a set of control parameters Θ and τ via Poincaré sections. The general 2D kinematic equation is simulated using the 2D flow field by Hwu et al. (1997). Similar to the experiments explained above, 21 particles in total are positioned equidistantly along the diameter aligned with the mid-point of the moving wall. The particles are tracked for 1000 periods. The flow topology visualized via numerical Poincaré sections gives the total picture of the phase diagram and serves as a benchmark for the discussions on the experimental results given in Sec. 5.5.

First, the analytical solution is used to assess the compatibility between the Lagrangian topologies of the 2D time-dependent RAM flow and the 3D spatially periodic RAM flow. Poincaré sections of the 3D RAM flow are adapted from the theoretical-numerical study by Speetjens et al. (2014), in which the calculations are performed for the cases of $\Theta = 2\pi/3$

and $\beta = \tau = 0.1$, 1, 5 and 11. Accordingly, numerical Poincaré sections of the 2D RAM flow are obtained for the same set of parameters, yet the experimental counterparts are not in the scope of the current study. The Poincaré sections depicted in Fig. 5.4 show a good agreement for $\beta = \tau = 0.1$ and 1, however this accordance deteriorates with stronger transverse forcing, i.e., stronger β, mainly because the axial flow in 3D case is a Poiseuille flow while for a one-to-one comparison one need a uniform axial flow. Both flows nonetheless are topologically equivalent (see Ref. (Speetjens et al., 2014)). Another reason is the formation of transition zones occurring between consecutive mixing cells, which expand with increasing β (Speetjens et al., 2014). Furthermore, 3D effects may even cause development of axial back-flow (local upstream flow) beyond a certain transverse forcing level β. Consequently, the discrepancy between the Poincaré sections of the 2D and 3D case increases with increasing β. Although the maps do not display one-to-one correspondence, the topology is the same in terms of mixing and non-mixing zones, which is consistent with the generic link between 3D steady RAM and 2D time-periodic RAM (Speetjens et al., 2014). This verifies the use of simplified 2D approach for qualitative analysis of mixing quality in 3D reoriented duct flows.
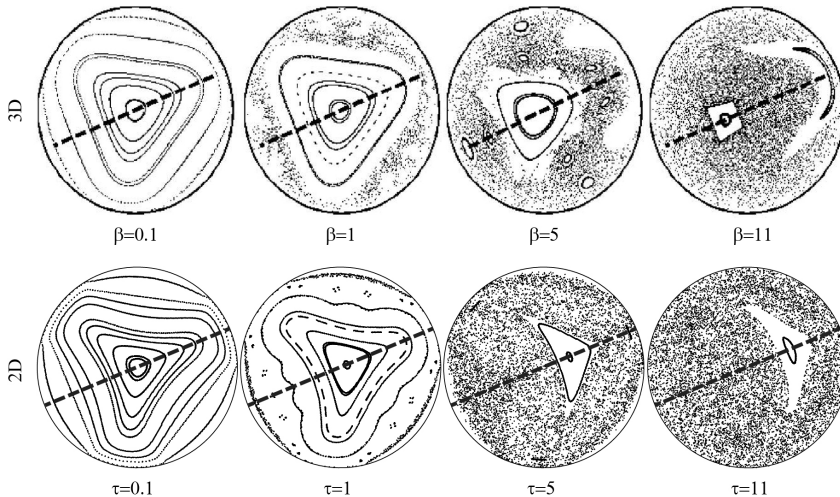

Figure 5.4: Numerical Poincaré sections for the offset angle $\Theta = 2\pi/3$ and for the temporal parameters $\beta = \tau = 0.1$, 1, 5 and 11 for the 3D steady RAM flow (top row) adapted from the study by Speetjens et al. (2014) and 2D time-periodic RAM flow (bottom row).

Figure 5.5 and Figure 5.6 show the numerical Poincaré sections computed for different values of Θ and τ. When τ is in the limit of zero, all cases are topological circles and the piecewise steady time-periodic nature of the flow coincides with the time-averaged steady flow case, i.e., it becomes identical to the case of all apertures running simultaneously (Speetjens et al., 2014). This is the reason why all particles are trapped in the trajectories defined by the flow streamlines. All cases with $\tau = 0.1$ correspond to a near integrable state of the Hamiltonian system (Speetjens et al., 2014). Regular particle trajectories result in an integral island and no fluid exchange occurs through the isolines of the island. Moreover, for non-zero Θ the main islands show p-fold symmetry where p is the number of steps per

period (see Sec. 3.2). For the cases with 2, 4 and 5 apertures in one period of motion, p is equal to 2 and 4 and 5, respectively.
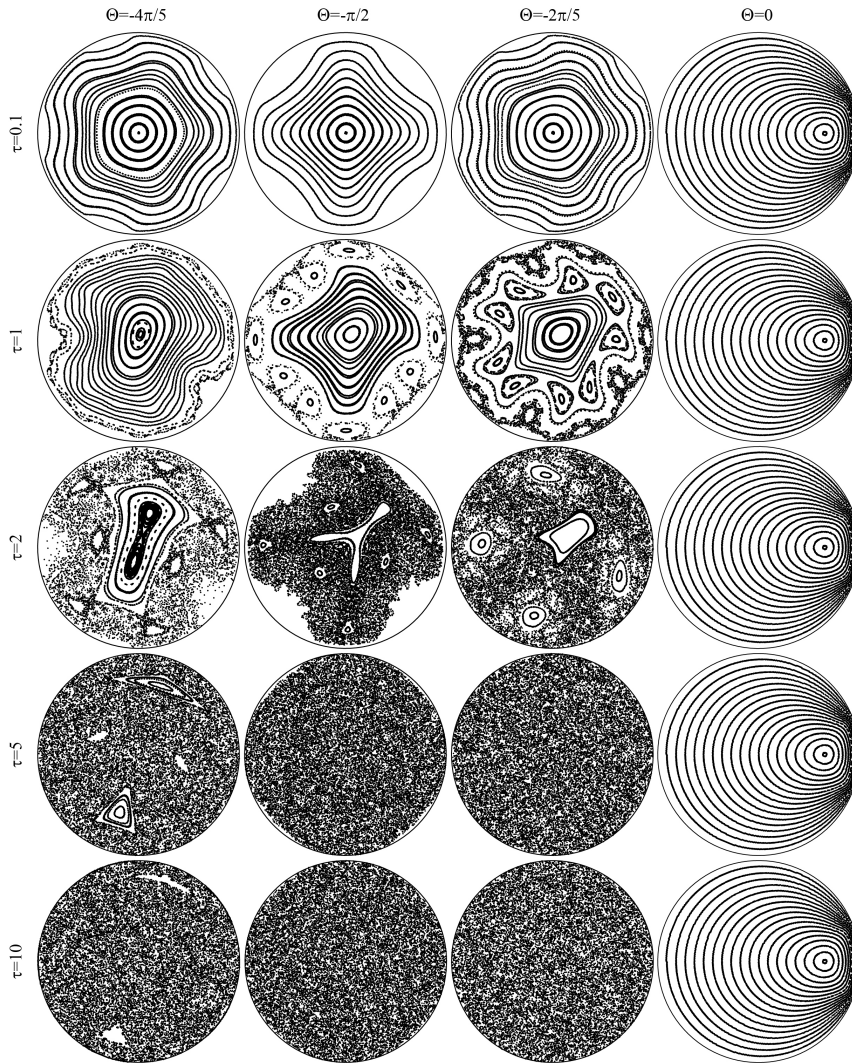

Figure 5.5: Numerical Poincaré sections for the offset angles of $\Theta = -4\pi/5, -\pi/2, -2\pi/5, 0$ and aperture activation time values of $\tau = 0.1, 1, 2, 5$ and 10.

For all cases except those with $\Theta = 0$ and π, as τ increases the regions of chaos form first near the apertures, then in the center region. In the case of $\Theta = \pi$, however, the chaos form first in the center region then in the outer region, which is similar to the flow topology observed in the blinking vortex flow (Aref, 1984). When τ is large enough, the chaotic region occupies the entire region (Fig. 5.5). Yet, the critical value of τ at which the globally chaotic
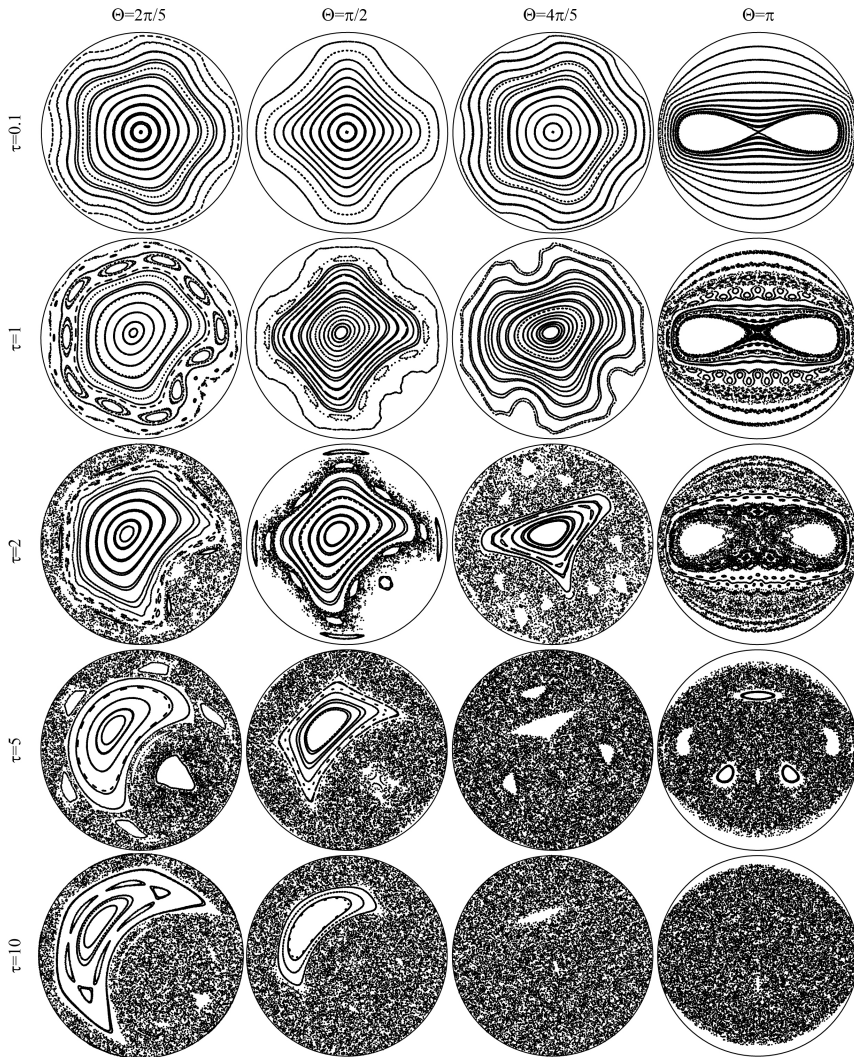
Figure 5.6: Numerical Poincaré sections for the offset angles of $\Theta = 2\pi/5, \pi/2, 4\pi/5, \pi$ and aperture activation time values of $\tau = 0.1, 1, 2, 5$ and 10.

state is achieved is highly dependent on Θ. The case with $\Theta = 0$ corresponds to the steady case with one aperture, where the particle trajectories coincides with the streamlines of the flow field. Evidently, integrable particle motion results in inefficient mixing.

At moderate τ values, chaotic regions coexist with regular islands. If the tracers are initially within a regular (elliptic) island, they remain inside forever, whereas the tracers initially inside the chaotic region travel the whole chaotic region. The boundaries of these islands, formed by Kolmogorov-Arnold-Moser (KAM) tori, act as barriers between chaotic

and regular regions. Near the boundary between these regions, there may exist a chain of islands of regular flow (see Fig. 5.5 and Fig. 5.6), where each island contains an elliptic periodic point and there exists a hyperbolic point between each island. This can be explained by the Poincaré-Hopf theorem, which states that for any vector field on a surface with finitely many critical points, the sum of indices of critical points is equal to the Euler characteristic of the surface (Ueno et al., 2005). For our particular case, where the surface is a disk and the vector field is the flow field, the Euler characteristic which is equal to the Poincaré index of the center elliptic point of the flow field is +1. In order to keep the Euler characteristic fixed, initial break up of a KAM line has to occur as pairs of hyperbolic and elliptic points, which have Poincaré indices -1 and +1, respectively.

The elliptic point, in systems with a time-periodic Hamiltonian, is a periodic point which returns to its initial position after certain (integer) number of periods and its presence in the flow topology is an indication of poor mixing. Increasing τ may shrink the size of the elliptic islands (Fig. 5.5), yet it does not guarantee the breakdown of the elliptic point even for large τ (see Fig. 5.6). The sign of the geometrical parameter Θ, on the other hand, determines if the flow can achieve global chaos (Speetjens et al., 2006). For instance, when $\Theta = -2\pi/5$ the flow becomes fully chaotic beyond a certain value of τ whereas for the case of $\Theta = 2\pi/5$, the elliptical island remains intact, independently of the change in τ. This is due to the fact that for $\Theta > 0$ the elliptic point of the main island does not undergo a bifurcation for any τ due to symmetry, whereas for $\Theta < 0$ there exists a critical τ beyond which the elliptic point becomes unstable through a period-doubling bifurcation (Speetjens et al., 2006). Period-doubling bifurcation is clearly visible in Fig. 5.5 for $\Theta = -4\pi/5$ and $\tau = 2$ by the break-up of the core of the central island into 2 smaller islands. The case with $\Theta = \pi$, on the other hand, shows different characteristics since the $\tau = 0$ limit is composed of a hyperbolic point at the center of the domain and two elliptic islands (Fig. 5.6). As τ increases the chaos onset in the region of the hyperbolic point and the size of the elliptic islands shrink similar to the transition to chaos in the van der Pol flow, which is the prototypical example of transition to chaos around a homoclinic connection (Morozov and Kostromina, 2014).

5.5. Experimental results

In this section, the results of the experiments are presented. First, in order to explore the state of the Lagrangian tracer dynamics, we construct Poincaré sections. The discussion largely proceeds by comparison between experimental and numerical Poincaré sections. Subsequently, characteristics of scalar patterns for varying experimental parameters are analyzed by means of dye pattern visualizations. These scalar patterns can also be obtained by the eigenfunctions of the advection diffusion equation, yet it is computationally expensive (especially for high-Pe cases). The variation of intensity is then used to quantify the mixing efficiency.

5.5.1. Poincaré sections

This section investigates the Lagrangian topology of the 2D RAM flow for varying control parameters Θ and τ by experiments. In Chapter 3 global Hamiltonian progression of the Lagrangian flow topology is already discussed for parameter set $\Theta = -\pi/2$ and $\tau = 0, 1, 2$

and 2.5. In this section, this analysis is extended in order to investigate the effect of the sign of Θ.

The experimental and numerical Poincaré sections for increasing τ at $\Theta = -2\pi/5$ are shown in Fig. 5.7. As discussed in detail in Sec. 3.4, for comparison with the computational results, the experimental τ needs to be adjusted to account for a slow-down of the flow due to friction with the lower fluid layer. The two cases compares well once $\tau_{\text{analytic}}/\tau_{\text{experiment}}$ is taken as 0.86, see Sec. 3.4.
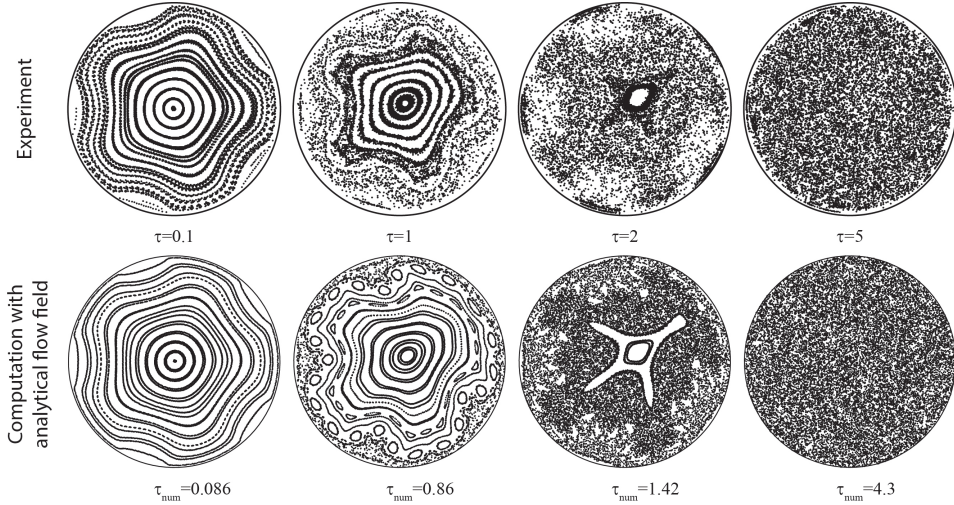
Figure 5.7: Poincaré sections for the cases of $\tau = 0.1, 1, 2$ and 5 for $\Theta = -2\pi/5$: experiments (top row) and computations (bottom row).

It is clear that the central island of the progression undergoes Hamiltonian breakdown from the integrable state (the leftmost) to a globally chaotic state (the rightmost). For the lowest τ, as mentioned above, the particles follow nested trajectories that act like impenetrable barriers and form the central island. The integrity of the central island deteriorates starting from the outer radial regions, yielding an intact island in a chaotic sea. The elliptic island disintegrates and becomes smaller as τ increases; also, constellations of smaller islands form due to break-up of resonant orbits that appear in the experiments as relatively less dense regions in the vicinity of the walls. Eventually, the system reaches fully chaotic state at $\tau = 5$. A much slower progression in terms of disintegration of the elliptic island occurs for $\Theta = 2\pi/5$, see also Fig. 5.8, so that fully chaotic state is not yet reached at the highest τ value. The initial central island always survives yet it changes in size and in shape with changing τ. This results in a poor mixing of the scalar which is also evidenced in Fig. 5.10. The results presented in this chapter bear similarities with those of the topological mixing studies in 3D reoriented duct flows in the literature (Speetjens et al., 2006, 2014) in the sense that a fully chaotic state is attained for negative Θ, whereas the cases of positive Θ contains non-mixed regions. This strict separation in behavior for negative and positive Θ holds true for the non-inertial case ($Re = 0$). Speetjens et al. (2014) demonstrated that the 3D non-inertial case has the same time-reversal symmetry and therefore displays the same bifurcation behavior as the 2D case. However, for 3D inertial flow ($Re > 0$) the
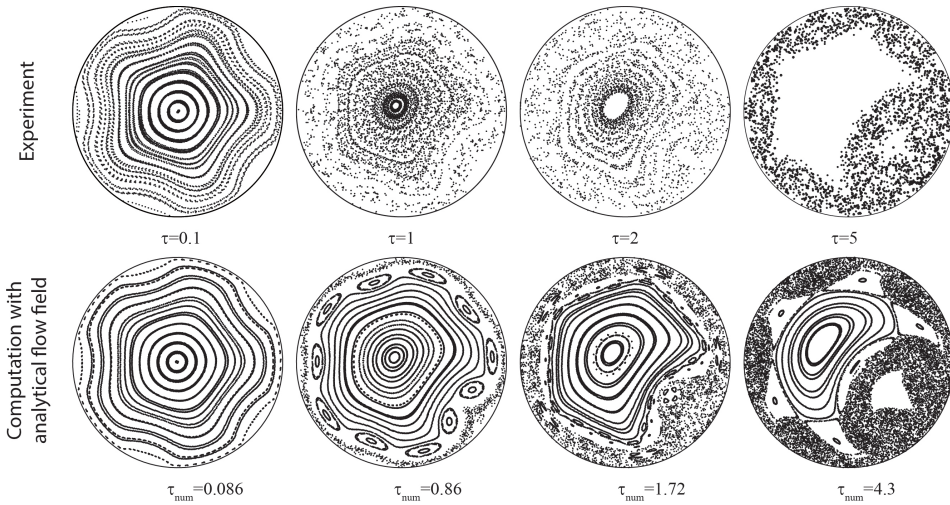
Figure 5.8: Poincaré sections for the cases of $\tau = 0.1, 2, 5$ and 10 for $\Theta = 2\pi/5$: experiments (top row) and computations (bottom row).

strict separation between negative and positive Θ is lost. Nonetheless, for $Re > 0$ period-doubling remains the only route to chaos.

The Poincaré sections computed from the analytical velocity field and those acquired in the experiments display excellent agreement for different Θ and τ values. This confirms the validity of the experiment for the study of Lagrangian transport under parametric variation and the applicability of the KAM and Poincaré-Birkhoff theorems to real fluid flows.

5.5.2. SCALAR PATTERNS IN THE LIMIT OF INFINITE-PE

Figure 5.9 shows scalar dye patterns after 20 periods for the offset angles of $\Theta = -4\pi/5$, $-\pi/2$, $-2\pi/5$ and 0 for increasing switching times ($0.1 \leq \tau \leq 10$). The scalar patterns for positive Θ are shown in Fig. 5.10. The $\Theta = 0$ case is a steady flow case with only one aperture activated and running continuously. Therefore, patterns for increasing τ values are simply the snapshots of the steady evolution. In this case, one continuously rotating single aperture generates a circulation region with a radial shear flow, that stretches the white-colored oil linearly forming a spiral shape. This case shows that shear flow is a very inefficient way to achieve mixing and the resultant field does not reach a globally mixed state.

It is clear that for the shortest switching time ($\tau = 0.1$), the scalar fields consist of a large intact island for all Θ values. In this regard, the patterns for non-zero Θ shown in the first row demonstrate a near-integrable state. The islands are p-fold rotationally symmetric, i.e. $\Theta = \pm 2\pi/5$ and $\Theta = \pm 4\pi/5$ gives 5-fold symmetry (the same also holds for the 4-fold symmetric islands of $\Theta = \pm\pi/2$), which shows a very good agreement with the corresponding numerical Poincaré sections shown in Fig. 5.5 and Fig. 5.6. This can be attributed to relatively short switching time value for the smallest τ so that the scalar transport only 'feels' the average flow for small τ. In an actual steady 3D RAM case, this is equivalent to

Figure 5.9: Experimental scalar patterns for the offset angles of $\Theta = -4\pi/5, -\pi/2, -2\pi/5, 0$ and aperture activation time values of $\tau = 0.1, 1, 2, 5$ and 10 visualized after 20τ.

the limit of very slow rotation of the outer cylinder (see Speetjens et al. (2006)).

For increasing τ, except for $\Theta = \pi$, the patterns become more complex particularly at the outer radial regions and thus especially for the cases of $\tau = 1$ and 2. This is due to the chaotic behavior in that region, which increases the stretching rate in the vicinity of the apertures, bringing about formation of filament-like extensions. Despite the generation of these filaments, the core of the pattern still stays undisturbed. The intact patterns in the scalar fields correspond to the central islands in the numerical Poincaré sections in

Figure 5.10: Experimental scalar patterns for the offset angles of $\Theta = 2\pi/5, \pi/2, 4\pi/5, 2\pi$ and aperture activation time values of $\tau = 0.1$, 1, 2, 5 and 10 visualized after 20τ.

Sec. 5.4, whereas the filament-like structures correspond to the chaotic regions. The dye patterns shown in Fig. 5.9 and Fig. 5.10 are in a good agreement with the Poincaré sections shown in Sec. 5.4. Yet, the experimental dye patterns reveal far more detail than the simulated patterns. This is a major advantage of the experiments over the computations.

The snapshots at later periods with $\Theta = -2\pi/5$ and $\tau = 2$ are shown in Fig. 5.11. In time, the shape of the dye pattern converges to a slightly distorted four-point star, however the surrounding filaments lose their sharpness due to mixing with the black-colored fluid. The
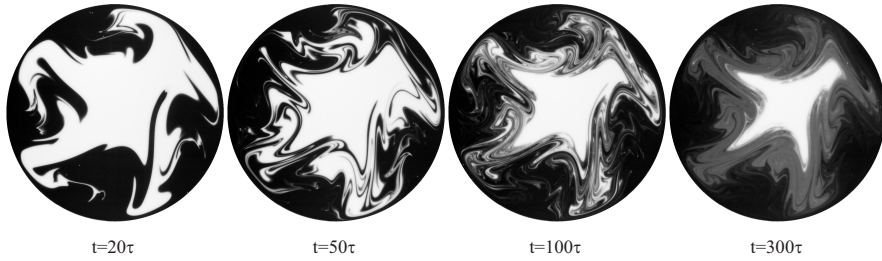
Figure 5.11: Scalar patterns at the non-dimensional time instants of $t = 20\tau$, 50τ, 100τ and 300τ for the case of $\Theta = -2\pi/5$ and $\tau = 2$.

mixing occurs by stretching and folding, which results in very fine filament structures. Due to the presence of diffusion, even though it is very weak, the image intensity values in the region surrounding the main island appear as gray in the snapshots.
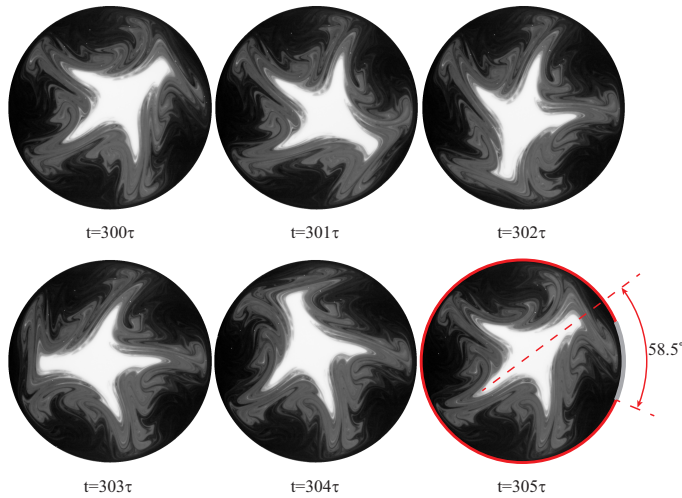

Figure 5.12: Scalar patterns at the non-dimensional time instants of $t = 300\tau$, 301τ, 302τ, 303τ, 304τ and 305τ for the case of $\Theta = -2\pi/5$ and $\tau = 2$.

The behavior of the core of the dye pattern within one period is illustrated in Fig. 5.12. The core of the dye pattern behaves roughly like a solid body and rotates and completes one full rotation during the period. The scalar field is symmetric about the axis at $\theta = (\Delta - \Theta)/2$ relative to the starting angle of the first window (Speetjens et al., 2006, 2014). This is shown in Fig. 5.12 (bottom right) for the case $\Theta = -2\pi/5$, where the symmetry line is at $\theta = 58.5°$ with respect to the starting angle of the first aperture. Speetjens et al. (2006, 2014) showed that symmetry imparted by the periodic reorientation and transverse forcing is the key factor in the attainment of unrestricted chaos and hence good mixing. The experimental results of the current study substantiate this decisive role of symmetry.

As mentioned previously, scalar field and particle position measurements are performed concurrently to allow the assessment of the correlation between the Poincaré

maps and scalar fields. As an example, the scalar field at $t = 200\tau$ is overlaid with the corresponding Poincaré sections for the case of $\Theta = -4\pi/5$ with varying τ values and shown in Fig. 5.13. The correlation between the dye pattern and Poincaré maps in terms of formation of coherent structures is verified by means of these experiments. The islands are formed where the particle trajectories are regular. On the other hand, the dye patterns become mixed when the particle behavior is chaotic. It is also clear that the resolution of the Poincaré sections is good enough to capture larger coherent structures. However, small-scale structures, e.g., the period-2 islands shown in the rightmost map in Fig. 5.13, are difficult resolve by experimental Poincaré sections, because this depends strongly on initial placement of particles inside the structure.

$\tau = 0.1$ $\tau = 1$

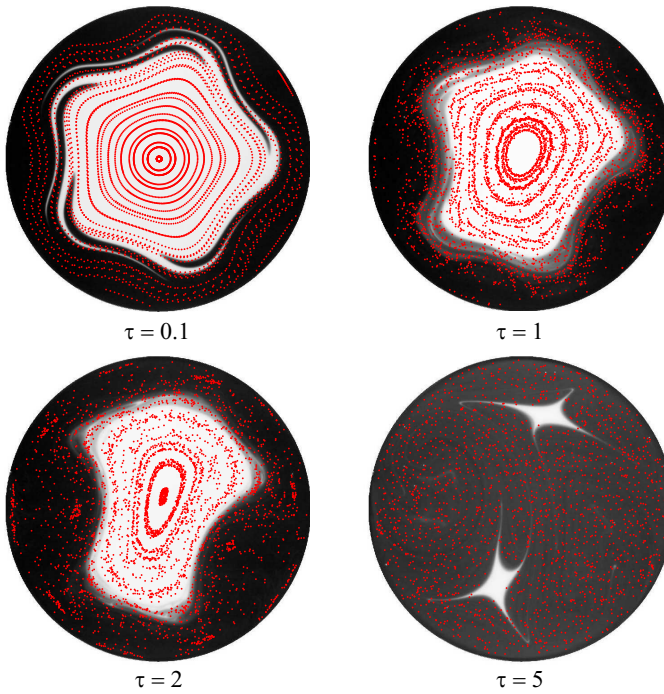$\tau = 2$ $\tau = 5$

Figure 5.13: Experimental Poincaré sections overlaid on the scalar fields, which are visualized at $t = 200\tau$ for the cases of $\Theta = -4\pi/5$ and $\tau = 0.1, 1, 2, 5$.

5.5.3. QUANTIFICATION OF MIXING EFFICIENCY

The intensity of segregation I_s (Danckwerts, 1952) is one of the statistical tools that enables quantifying the homogeneity of an initially segregated mixture and it has already been employed to quantify mixing in a theoretical study of the RAM parametric variation by Singh et al. Singh et al. (2008) The intensity of segregation is defined by:

$$I_s = \frac{\langle (I - \langle I \rangle)^2 \rangle}{\langle I \rangle \, (1 - \langle I \rangle)} \tag{5.1}$$

where I is the normalized corrected intensity of the scalar field ($0 \leq I \leq 1$) and $\langle \rangle$ the linear averaging operator. The intensity of segregation refers to the variation of the intensities in the mixture and it tends to zero for perfect mixing.
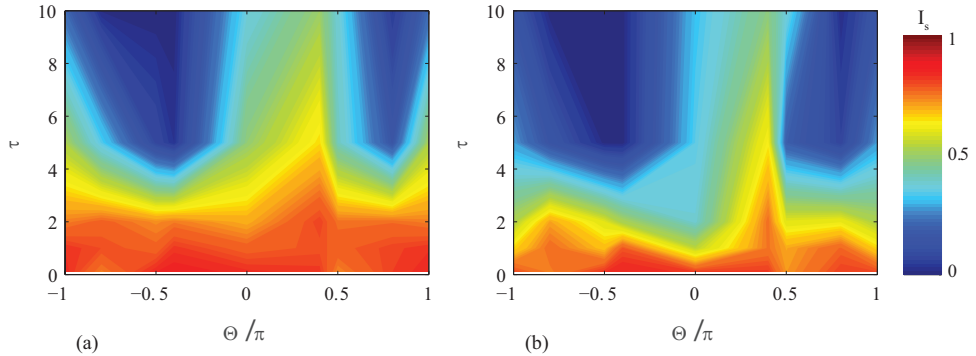

Figure 5.14: Contour plots of intensity of segregation I_s for varying offset angle Θ and switching period τ parameters over full domain after (a) $t = 20\tau$ and (b) $t = 80\tau$.

Contour plots of I_s are plotted for varying Θ and τ parameters of the RAM flow after non-dimensional time of $t = 20\tau$ and $t = 80\tau$ in Fig. 5.14. In these contour plots, blue indicates good mixing, whereas red indicates poor mixing. In the red regions, the scalar field is not mixed well and there are generally intact islands of non-mixed colored fluid present in the scalar field as discussed in the previous section.

For time span $t = 20\tau$ (Fig. 5.14a), roughly for $\tau \lesssim 2$, all positive and negative Θ cases have a poor mixing performance. The evidence for this is the large elliptic islands and intact dye patterns shown in Sec. 5.4 and Sec. 5.5.2. In general, increase of τ improves the mixing efficiency yet the region bounded by $0 < \Theta < \pi/2$ displays rather poor mixing due to the existence of persistent islands in the scalar patterns. Negative Θ cases achieve better mixing (blue in Fig. 5.14), which is in agreement with the dye visualizations and numerical Poincaré sections. In time, the mixing efficiency increases (Fig. 5.14b). The blue regions (good mixing) expand for both positive and negative values of Θ. However, the region between $\Theta = 0$ and $\Theta = \pi/2$ still has poor mixing performance, which is in accordance with the persistence of the large dye patterns and lack of global mixing for these cases as demonstrated in Figs. 5.9 and 5.10.

The implications of this parametric study can also be interpreted in the context of 3D reoriented duct flows. The parameter τ in the 2D configuration formally corresponds to the transversal forcing parameter β in the 3D flow case, as explained in Sec. 3.2. In the experiments, τ increases with increasing activation time of one window for a fixed angular velocity Ω, which is analogous to decreasing axial flow velocity U_{mean} or increasing aperture length L in 3D RAM flow. Therefore, in order to enhance the mixing quality in the actual 3D RAM for a given Θ and Ω, it is required to increase the relative strength of the transversal forcing by either slowing down the axial flow or increasing the axial extent L of

one cell in the 3D RAM based on the fact that the mixing quality increases with increasing τ. However, in many industrial applications, it is desired to attain a good mixing quality over a short length of a mixer, which implies that it is more favorable to reach a fully mixed state at the smallest possible τ. On the other hand, regarding the reorientation angle Θ, it is clear that negative values (i.e., counter rotation of the outer cylinder with respect to the reorientation direction of the apertures in 3D RAM) works better in terms of attainment of globally chaotic regime (see Fig. 5.5 in comparison to 5.6) and good mixing (see Fig. 5.9 in comparison to Fig. 5.10). Therefore, the best strategy for practical applications is searching for the negative offset angle which can achieve a fully chaotic state at the least possible value of β.

Among the parameters of this study, the $\Theta = -2\pi/5$ configuration shows the best mixing performance for $\tau \geq 5$, as evidenced by the Poincaré sections (Fig. 5.5), the dye patterns (Fig. 5.9) and the intensity of segregation (Fig. 5.14). The outcome of this parametric study in terms of the relation between the flow topologies and the control parameters can also be utilized to define varying-Θ protocols by which a high-quality mixing even at smaller τ can be achieved. For instance, it is shown in the Poincaré maps (Fig. 5.6) and also in the dye visualizations (Fig. 5.10) that for $\Theta = \pi$ the onset of chaos occurs in the center of the circular domain. On the other hand, in all other non-zero Θ cases, the chaos emerges in the proximity of the circular wall of the domain. Based on these observations, protocols with different Θ can be combined to enhance the mixing quality. A period of a varying-Θ protocol is composed of two main stages: (1) a period of $\Theta_1 = \pi$ protocol for which $A1$ and $A3$ are activated sequentially; (2) a period of other non-zero Θ_2 protocols. For instance, when $\Theta_2 = -\pi/2$, the activation sequence of the apertures in a period of motion is $A1 - A3 - A1 - A4 - A3 - A2$. This approach leans on some earlier reported ideas. For example, varying mixing protocols to break symmetry and enhance mixing has already been studied by Franjione and coworkers theoretically (Franjione and Ottino, 1992; Franjione et al., 1989), yet the protocols they studied cannot be implemented in experiments. Moreover, in the work by Metcalfe et al. (2006) the Θ sequence is manipulated to break up islands earlier in τ.

The simulated Poincaré sections for the varying-Θ protocols are shown in Fig. 5.15 and 5.16 for Θ_2 protocols formed by five-window and four-window activations, respectively. In general, the varying-Θ protocols a reach fully chaotic state at smaller τ than non-varying Θ cases discussed above. Even for the combinations that employ positive Θ_2 protocols, a fully chaotic state is achievable in contrast to non-varying positive Θ cases. This is due to the fact that the varying angles result in symmetry breaking. One consequence of this is that the central elliptic island of the integrable state must not necessarily persist for positive offset. Instead, it may now completely break down for positive offset. Moreover, the already good superior performance of the non-varying negative Θ cases is further improved as a result of the combination with $\Theta_1 = \pi$ such that a globally chaotic state is attained at even smaller τ. The comparison between the Poincaré sections for different Θ_2 cases reveals that the combination case with $\Theta_2 = -2\pi/5$ shows the best performance.
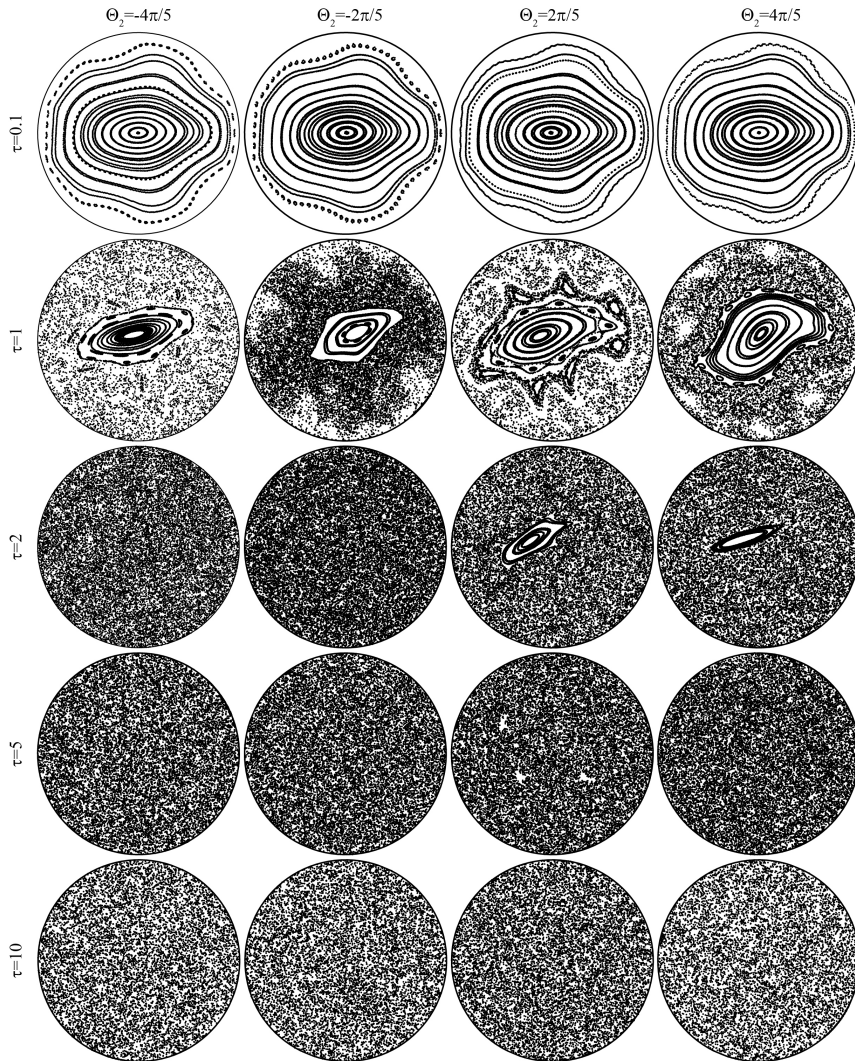
Figure 5.15: Numerical Poincaré sections for the varying-Θ protocols of $\Theta_1 = \pi/2$ combined with $\Theta_2 = -4\pi/5$, $-2\pi/5$, $2\pi/5$ and $4\pi/5$ for aperture activation time values of $\tau = 0.1, 1, 2, 5$ and 10.

5.6. CONCLUSION

The results of this chapter show that the comparison of the numerical Poincaré sections for 2D time-periodic RAM and 3D spatially-periodic RAM flows reveals a good qualitative agreement in terms of the features indicative of mixed and non-mixed regions, which substantiates the suitability of 2D time-dependent RAM flows for the qualitative analysis of mixing in 3D reoriented duct flows. Furthermore, the experimental Poincaré sections
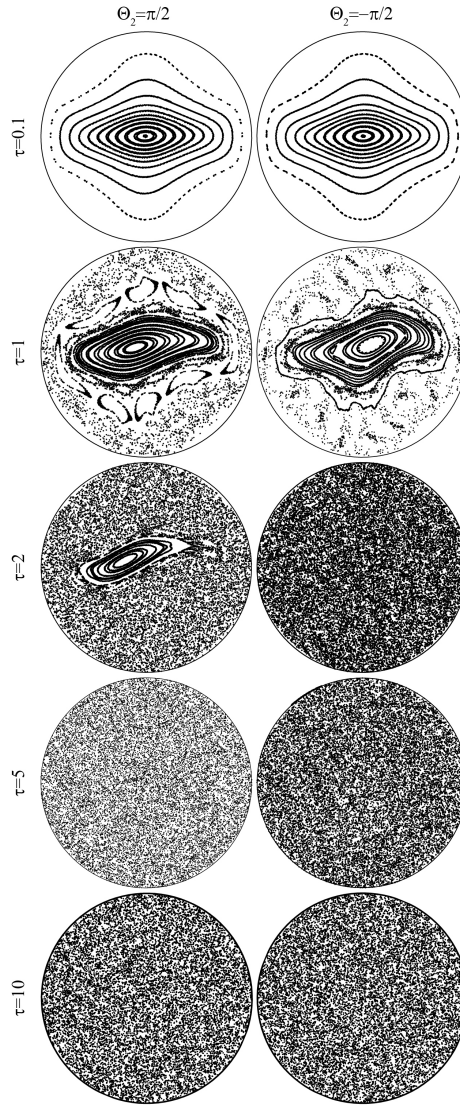
Figure 5.16: Numerical Poincaré sections for the varying-Θ protocols of $\Theta_1 = \pi/2$ combined with $\Theta_2 = -\pi/2$ and $\pi/2$ for aperture activation time values of $\tau = 0.1, 1, 2, 5$ and 10.

validates their numerical counterparts by confirming the effect of the sign of Θ on reaching a globally chaotic state: positive Θ cases need much longer τ to achieve a fully chaotic state. Moreover, the overall agreement between the experimental and numerical results confirms the validity of the experimental facility for realizing 2D time-dependent RAM flow and performing reliable mixing studies.

The dye visualizations performed for the parametric analysis of the scalar fields, which

is very challenging for such a low diffusivity if analyzed numerically, allow for a comparative analysis between the Lagrangian dynamics presented by the Poincaré maps and the scalar patterns. Moreover, the quantification of the mixing efficiency further validates that the cases with negative offset and relatively long switching time ($\tau > 5$) achieve good mixing, whereas the performance is poor for $\tau < 2$, regardless of the Θ value. There is a region in the parameter space bounded by $0 < \Theta < \pi/2$, which displays poor mixing characteristics even after a long time ($t = 80\tau$).

Varying-Θ protocols, when defined systematically, enhances the mixing efficiency. We combined the $\Theta = \pi$ case, where chaos emerges in the center of the circular domain, with other non-zero Θ cases, for which the chaotic state is initially reached in the vicinity of the walls. This combination strategy increases the mixing efficiency by lowering τ needed for a globally chaotic state for a given Θ. Even for the positive Θ cases, combination with the $\Theta = \pi$ protocol dramatically reduces τ that accomplishes a fully chaotic state. The success of the combined forcing strategy implies that flow topologies and scalar field evolutions acquired for systematically varying control parameters can be utilized to design an efficient mixing flow. As a future work, varying-Θ protocols different than the ones discussed in this chapter can be investigated to find the optimum forcing protocol that achieves global mixing with the least possible effort.

The results presented in this chapter is qualitatively relevant to generic 3D reoriented duct flows. The Kenics mixers, for instance, also have temporal and geometrical parameters that affect the mixing efficiency of the mixer in a way similar to the parameters of the RAM. Therefore, the outcomes of the current work is useful in determining the optimal control parameters of a reoriented duct flow that can accomplish an efficient mixing.

5

6

ADVECTIVE-DIFFUSIVE SCALAR TRANSPORT IN 3D SPATIALLY-PERIODIC SYSTEMS

Spatially persisting patterns form during the downstream evolution of passive scalars in three-dimensional (3D) spatially-periodic flows due to the coupled effect of stretching-folding and mechanisms of the flow field. This has been investigated in many computational and theoretical studies in 2D time-periodic and 3D spatially-periodic flow fields; however, experimental studies, to date, have mainly focused on flow visualizations with streaks of dye rather than fully 3D scalar field measurements. Our study employs state-of-the-art experimental methods to analyze the evolution of 3D scalar fields and the correlation between the coherent flow/scalar field structures in a representative inline mixer, the Quatro static mixer. The experimental setup consists of an optically accessible test section with transparent internal elements, accommodating a pressure-driven pipe flow. The 3D flow and scalar fields are measured by 3D particle tracking velocimetry and 3D laser-induced fluorescence, respectively. The results show a good agreement with those reported in the literature. The experimental analysis performed in this study has been proven to be suitable for exploratory mixing studies of a variety of mixing devices.

6.1. INTRODUCTION

Advective-diffusive scalar transport in periodic laminar flows is of practical relevance to various industrial thermo-fluid processes that employ the inline mixing principle. Two important practical categories are the blending of highly-viscous fluids (e.g., polymers, food, etc.) and micro-fluidics (e.g. lab-on-a-chip technologies, bio-medical devices, etc.). Today's technology in inline mixing systems is based on empirical knowledge. However, further advancement is feasible if fundamental transport mechanisms are well-understood. In the past few decades the fundamentals and applications of mass/scalar transport in spatially-periodic laminar flows have been studied in numerous theoretical and numerical investigations (Galaktionov et al., 2002; Gorodetskyi et al., 2014; Kumar et al., 2008; Meleshko et al., 1999; Ottino, 1990; Speetjens et al., 2006, 2014; Thakur et al., 2003). Nevertheless, a complete understanding is not achieved yet. Particularly, experimental studies are scarce and usually restricted to highly-idealized flow geometries or allowing only partial access to the flow domain with (optical) diagnostic tools (Castelain et al., 2001; Kusch and Ottino, 1992; Metcalfe et al., 2006; Ottino, 1990; Pust et al., 2006). The work presented here aims to fill this gap via laboratory experiments in a real mixer geometry.

The current study adopts the Quatro mixer (Primix BV, Mijdrecht, The Netherlands), which is shown in Fig. 6.1, as representative inline mixer for in-depth analysis of advective-diffusive transport of scalars in industrial processes. The main objective is to experimentally investigate and validate downstream evolution of a scalar field under the action of spatially-periodic laminar flow field. For this purpose, an experimental setup mimicking the realistic (industrial) flow conditions and holding a transparent replica of the Quatro mixer geometry is realized. The flow and concentration field measurements are performed to investigate the downstream evolution of advective-diffusive or only-advective scalar fields.
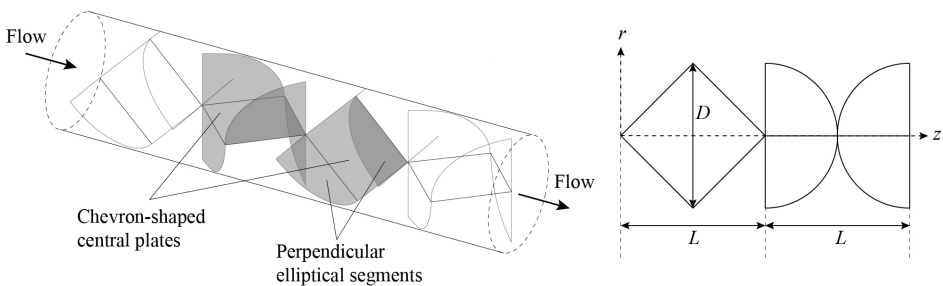

Figure 6.1: A schematic of the Quatro mixer. The left panel shows the geometry of the Quatro mixer with the chevron-shaped central plates, perpendicular elliptical segments extending to the cylinder wall and the axial throughflow. The right panel shows the r-axis and z-axis of the cylindrical coordinate system, the cylinder diameter and the diagonal D and the element length L.

6.2. Modeling flow and Scalar transport

6.2.1. Configuration and governing equations

The configuration is a steady, laminar, incompressible flow field and its related steady advective-diffusive scalar field inside the 3D domain $\mathscr{D}$ representing the mixer geometry. The governing non-dimensional mass, momentum and advection-diffusion equations are

$$\nabla \cdot \boldsymbol{u} = 0, \ \ Re \, \boldsymbol{u} \cdot \nabla \boldsymbol{u} = -\nabla P + \nabla^2 \boldsymbol{u}, \tag{6.1}$$

$$\boldsymbol{u} \cdot \nabla C = \frac{1}{Pe} \nabla^2 C, \ \ C|_{z=0} = \begin{cases} 1, & \text{if } y \geq 0 \\ 0, & \text{if } y < 0 \end{cases} \tag{6.2}$$

where $\boldsymbol{u}$ is the fluid velocity, P the pressure and C the scalar field. These equations are also supplemented with no-slip conditions at the walls. Poiseuille flow is prescribed at the inlet, whereas a constant pressure boundary condition is set at the oulet. The 3D coordinate system is defined in such a way that (x, y)-plane corresponds to the transverse direction, whereas z-direction corresponds to the axial direction, see Fig. 1.3. In Eq.(6.1) and (6.2), Re and Pe are the Reynolds and Péclet numbers, respectively, defined as

$$Re = \frac{UR}{\nu}, \ \ Pe = \frac{UR}{\alpha}, \tag{6.3}$$

where U and R are the characteristic velocity of the flow field (i.e. mean velocity U_{mean}) and the radius of the mixer, respectively, ν is the kinematic viscosity and α the material diffusivity. The geometrical parameter $\Lambda = L/D$ (see Fig. 1.3) is set to 1 in the current configuration. For the experiments it turns out that $Re \approx 3.5$ in the flow field measurements, whereas $Re \approx 0.5$ and Pe is in the limit of infinity (assuming $\alpha \approx 0$) in the concentration field measurements (see Section 6.3.2 for the values of ν, U_{mean} and R). The difference in Re is due to the restrictions imposed by practical issues. The concentration field is made dimensionless according to $C' = (C - \min C_0(\boldsymbol{x}))/(\max C_0(\boldsymbol{x}) - \min C_0(\boldsymbol{x}))$, with C being the dimensionful scalar, $\min C_0(\boldsymbol{x})$ and $\max C_0(\boldsymbol{x})$ the minimum and maximum value of the initial scalar field $C_0(\boldsymbol{x})$, respectively. The prime indicating the non-dimensional concentration is dropped hereafter.

Scalar field analysis concerns purely advective transport (i.e. infinite Pe) in the Quatro mixer, which is an industrially-relevant case that is representative of more generic cases. This can be achieved in the experiments by use of a dyed fluid with a low diffusivity ($\alpha \approx 0$). However, in the simulations, accurate computations are possible only up to about $Pe = 1000$ due to the restriction imposed by the numerical resolution. This is a disadvantage of the simulations compared to the experiments and implies the importance of the experimental studies on this type of problems, which is a strong motivation for the current study. Therefore, the study focuses on the features that agree in both cases (e.g. larger-scale structures and general correlation with the flow field) rather than one-to-one comparison between experiments and simulations.

In both cases, an inflow boundary condition is prescribed for the scalar field such that at the inlet of the mixer (z=0) the scalar distribution (pattern) is segregated i.e. half of cross-sectional area is covered with soluted fluid (C=1) while the remaining part is filled with plain fluid (C=0).

6.2.2. Eigenmode structure of scalar fields

In 3D spatially-periodic flow fields, assuming that the axial flow component is unidirectional, the downstream evolution of the scalar field is dynamically similar to an evolution in time in an equivalent 2D time-periodic flow field. In both cases, the scalar transport is governed by the linear advection–diffusion equations and can be mathematically analyzed in terms of the fundamental solutions, i.e. the eigenmodes, of the advection–diffusion operator. The scalar field $C(x, y, nZ)$, where Z is the non-dimensional period length and nZ the integer multiples of Z, can be approximated as a finite sum of these modes, yielding

$$C(x, y, nZ) = \sum_{k=0}^{K} \gamma_k \varphi_k(x, y) \lambda_k^n, \ \ \lambda_k = e^{\mu_k Z}, \tag{6.4}$$

where the γ_k are the expansion coefficients based on initial conditions, the $\mathcal{H}_k(x, y, nZ) = \varphi_k(x, y) \lambda_k^n$ Floquet modes, $\mu_k = \sigma_k + i\omega_k$ with $i = \sqrt{-1}$ Floquet exponents and the set $\{\varphi_k, \mu_k\}$ represent the corresponding eigenfunction-eigenvalue pairs governed by the eigenvalue problem

$$\mathcal{L}\varphi_k - \mu_k \varphi_k = 0, \tag{6.5}$$

where $\mathcal{L}$ is the advection–diffusion operator.

In the case of finite-Pe, the real part of any Floquet exponent $\sigma_k < 0$ or equivalently any eigenvalue $|\lambda_k| < 1$ for non-uniform eigenmodes, which means that these modes all decay exponentially in time. The slowest one is the dominant mode, and represented by the set $\{\varphi_1, \mu_1\}$, causing the evolution to quickly become governed by the reduced expansion

$$C(x, y, nZ) = \gamma_1 \varphi_1(x, y) e^{\mu_1 nZ} + C_\infty, \tag{6.6}$$

where C_∞ is the trivial homogeneous eigenmode φ_0 that corresponds to $\mu_0 = 0$.

In the limit of infinite-Pe, the transport is equal to the passive advection of a scalar since the diffusion is negligible. The fundamental difference with the finite-Pe case is that now only purely imaginary exponents (i.e. $\mu_k = i\omega_k$) occur for all eigenmodes, meaning that none of the eigenmodes will decay. This has the fundamental implication that the evolution becomes of the form

$$C(x, y, nZ) = \sum_k \gamma_k \varphi_k(x, y) e^{i\omega_k nZ} + C_\infty \tag{6.7}$$

where eigenmodes become spatially arranged according to islands and chaotic regions (Speetjens et al., 2013). For periodic systems in the infinite-Pe limit, the eigenmodes become intimately related to the periodicity and multiplicity of the coherent structures in the Poincaré section and periodic eigenmodes (i.e. $\omega_k = 2\pi j/Z$) with "low" periodicity (i.e. $j = 1, 2$) dominating the behavior and in that sense act as the dominant eigenmodes. The reason for this dominance of lower-order eigenmodes is that higher-order structures are always embedded in lower-order structures. Lower-order structures therefore correspond to (global) larger-scale features, while higher-order structures correspond to (local) smaller-scale features (Singh et al., 2009).

In this chapter, the eigenmode analysis is restricted to the finite-Pe case due to complex nature of the scalar patterns in infinite-Pe case. The experimental scalar fields given

in Sec. 6.5 reveal the growing complexity of the cross-sectional scalar fields in the flow direction and imply that the scalar patterns will continue to grow more complex as the number of mixing elements increase. Yet, the experimental setup has only 7 periodic mixing elements (Sec. 2.4.5), meaning that the information at hand is only a part of a full evolution. Hence, more periodic elements are needed to fully capture the evolution from initial to final state. The numerical simulations, on the other hand, already cover basically the entire evolution from initial to final state with the same number of periodic elements, meaning that here all relevant info for a reliable spectral analysis is available. A further complicating factor regarding spectral analysis of the experimental data is that the transport shows all signs of being chaotic, which implies a far richer spectrum for the experimental high-Pe case compared to the numerical moderate-Pe case. Well-defined larger-scale periodic structures with a low periodicity (e.g. isolated islands or island chains) are completely absent here, meaning that even upon convergence, clear dominance by a discrete set of lower-order modes is not to be expected. Instead, a full and noisy spectrum throughout the entire wavenumber range is to be expected.

6.3. METHODOLOGY

6.3.1. NUMERICAL SIMULATIONS

A finite element method (FEM) is used in Comsol Multiphysics 4.3b to solve 3D mass and momentum equations (Eq.(6.1)) and the advection-diffusion equation (Eq.(6.2)). A mixer model with 10 periods (20 mixing elements) is built in Comsol and an unstructured tetrahedral grid is constructed with approximately 30 million elements to maintain the numerical stability. The numerical convergence and accuracy are inspected by standard grid refinement tests. Integrations were performed with a second-order backward-difference scheme. A relative tolerance of 10^{-3} is prescribed for the velocity components of the steady flow field and the steady scalar field in the solver.

6.3.2. EXPERIMENTAL FACILITIES AND MEASUREMENT TECHNIQUES

Detailed descriptions of the Quatro mixer facilities are given in Section 2.3. Two state-of-the-art optical measurement methods will be employed: 3D particle tracking velocimetry (3D PTV) and 3D laser induced fluorescence (3D LIF). The reader is referred to Section 2.4 for the details of these methods.

6.3.3. DATA PROCESSING AND ANALYSIS

Data processing and analysis of scalar transport is based on the dynamic mode decomposition (DMD). The mathematical background of the method is closely following the eigenvalue algorithms (i.e. Arnoldi algorithm) in numerical linear algebra and the method aims to recover the actual eigenmode decomposition (Eq.(6.4)) from data at discrete temporal/spatial levels. It assumes that the subsequent levels relate via a mapping:

$$\boldsymbol{c}_{n+1} = \mathscr{A}\,\boldsymbol{c}_n \tag{6.8}$$

where c_n denotes the scalar field in discrete partitions in the domain at level $z_n = n\Delta z$ and $\mathscr{A}$ is a linear operator that maps a scalar field c_n to the consecutive one c_{n+1}. The eigenfunction–eigenvalue pairs of the mapping matrix $\mathscr{A}$ are the approximations for the eigenfunction-eigenvalue pairs $\{\varphi_k, \mu_k\}$ of the advection–diffusion operator $\mathscr{L}$. The details of the algorithm can be found in Schmid (2010, 2011).

6.4. Velocity field analysis

In this section, a comparative analysis between experimental and numerical flow fields is performed. Compared to analysis given in the work by Jilisen et al. (2013), this study presents more accurate flow/streamline measurements by an enhanced calibration and a post-processing algorithm and explicitly analyzes the effect of the inlet conditions on the periodicity of the flow. Refer to Section 2.4.4 for the details of the modification in the calibration and the post-processing. An error analysis is also presented there.

6.4.1. Periodicity of the flow field

In fluid processing industries, inline mixers constitute a part of a piping system and can be placed at any location regardless of local flow conditions. This alters the inlet conditions of the flow field inside the mixer (i.e. inlet condition deviates from Poiseuille flow profile). However, the flow quickly settles on a periodic state, regardless of inlet conditions, which is demonstrated below.

In order to investigate the effect of altered inlet conditions on the periodicity of the flow inside the mixer and to check if the periodic flow assumption holds true, two different blockage conditions are prescribed at the inlet ($z = 0$) of the mixer in simulations. However, in the experiments, only one blockage condition is implemented. The numerical flow field of the 2nd periodic element without inlet blockage is set as the benchmark case. The comparative analysis is performed on more than 18,000 data points, the positions of which are taken from the experimental data set and the corresponding data points in numerical simulations are calculated by a cubic interpolation, and the deviation is quantified via $\epsilon(\mathrm{u}) \equiv |\mathrm{u}_b - \mathrm{u}_c|/|\mathrm{u}_{b,\max}|$ where u can be the velocity components u, v, w and magnitude $\|\boldsymbol{u}\|$. Here, b and c stand for the benchmark case and any other case, respectively.

Figure 6.2 shows the experimental and numerical deviations from the benchmark case when the inlet is blocked by two different shapes (i.e. by a tightly-fitting square and a quarter circle blocking one-fourth of the cross-sectional area). The deviations in the numerical cases is below 3 %, which can be attributed to the interpolation errors. The experimental statistics are consistent with the error estimated in Section 2.4.4. Any disturbance, generally speaking, at the inlet vanishes within the first element and all cases converge to the same benchmark case. Therefore, it is plausible to conclude that the flow field at $Re = 3.5$ is basically independent of inlet conditions — an important fundamental characteristic of the flow — and quickly settles for one and the same periodic state. Here, this happens already after one mixing element, meaning that periodic flow can be assumed from the second element onwards.
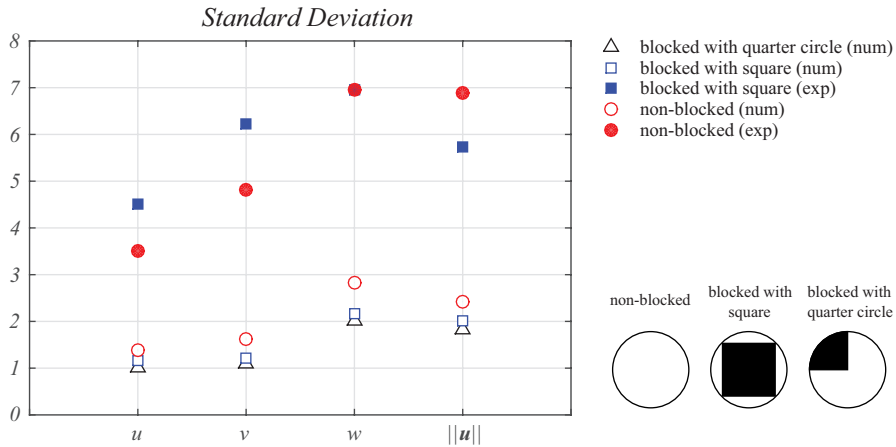
Figure 6.2: Standard deviation of the differences between experimental and periodic numerical data (open symbols: numerical data, filled symbols: experimental data). The values are in percentage. The experiments are only conducted with one (tightly-fitting square) blockage condition.

6.4.2. VELOCITY FIELD

The computed velocity fields at five axial positions along a periodic segment of the mixer (where z' is the axial position within a periodic segment) are shown in Fig. 6.3. The columns from left to right show the plots of non-dimensional velocity magnitude $\|\boldsymbol{u}\|$, azimuthal velocity component $u_{\text{azi}} = (u, v)$ and axial velocity component w. As mentioned earlier, the second element of a periodic segment is the reflected and rotated version of the first one. The effect of this configuration is clearly visible in the flow fields for all velocity components. The flow field pattern at $z' = L$ is essentially a mirrored version of that at $z' = 0$, while the pattern at $z' = 3L/2$ is a rotated form of the flow field at $z' = L/2$. As expected, the velocity pattern repeats itself at $z' = 2L$ in accordance with the periodic configuration of the geometry. In general, the axial flow component is dominant, whereas the azimuthal flow component is marginal particularly at the inlet/outlet regions. Stronger azimuthal velocity component at the mid-plane (compared to the inlet/outlet planes) indicates that the flow has a higher circulation in this region.

Figure 6.4 shows the contour plots of the velocity magnitude at the inlet and the mid-plane of the first element obtained via 3D PTV experiments and computed numerically. Despite the differences observed, similar flow structures emerge in both cases. There are two main reasons for the poorer data quality in experimental plots: the optical obstruction by the edges of the mixing elements and the tendency of the tracer particles to stay distant from the walls. The effect of the former is well visible in the top left plot of Fig. 6.4. As the cameras are positioned in the region where $y > 0$ (less optical obstruction in this region), the top half of the plot ($y > 0$) shows a better agreement compared to the bottom half ($y < 0$) of the plot. The effect of the latter can also be clearly seen in the experimental results. In the close proximity of the walls and mixing elements, the particles trajectories do not exist. Hence, the determination of the velocity field in these regions is possible
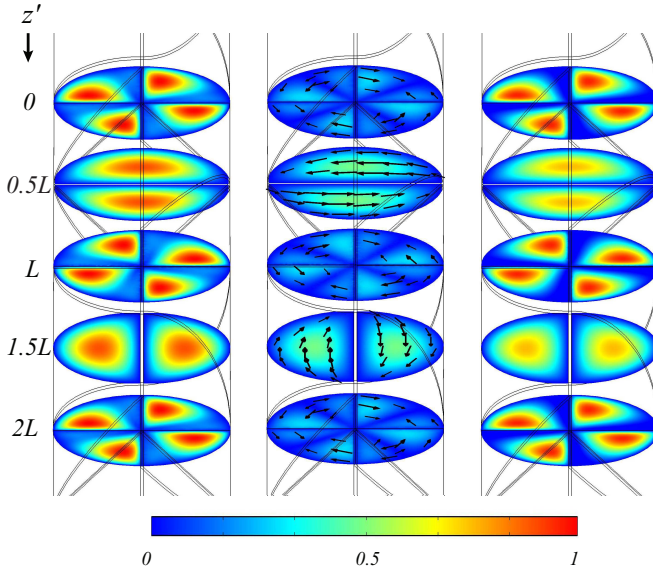
Figure 6.3: Cross-sectional evolution of velocity field inside Quatro mixer at Re=3.5 within a periodic segment (which is composed of two mixing elements). The contour plots from left to right show velocity magnitude $\|u\|$, azimuthal velocity component $u_{azi} = (u, v)$ and axial velocity component w. All values are non-dimensionalized with U_{mean}. 1st, 3rd and 5th rows indicate the inlet-outlet planes of the elements, whereas 2nd and 4th rows refer to the mid-planes of the elements.

only by interpolation of the neighboring data points. This explains why the zero-velocity regions do not appear in the results even though they physically exist in the experiments. However, overall, the comparison reveals a good agreement between the experiments and the simulations.

6.4.3. STREAMLINES

This section includes a comparative analysis of transport properties on the basis of large-scale coherent flow structures of the experimental and numerical flow fields. The reason for analyzing the flow field in terms of the coherent structures rather than individual streamlines is the chaotic nature of the mixing flows. In chaotic flows the individual streamlines have very sensitive dependence on initial conditions and a small shift in the initial position of a fluid particle may cause a completely different fluid path (Ott, 2002; Ottino, 1989). Owing to the fact that the uncertainty in flow measurements (via 3D PTV) leads to (small) deviations in particle positions, a comparative (experimental and numerical) analysis on the basis of individual streamlines is ineffective for the current study (Jilisen et al., 2013). However, coherent structures formed by streamlines are robust and therefore insensitive to such deviation.

Figure 6.5 shows the 3D experimental (blue) and numerical (red) streamlines in a periodic segment of the Quatro mixer at Re =3.5 and exposes a large scale coherence in the
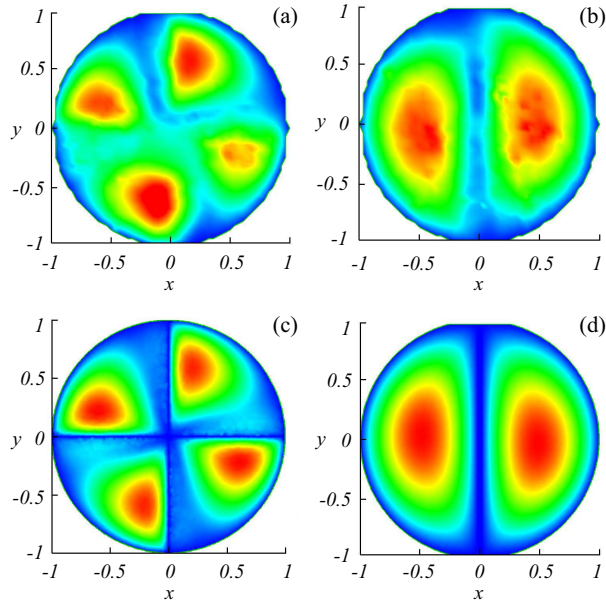
Figure 6.4: Dimensionless velocity magnitude at the inlet (left column) and the mid-plane (right column) acquired experimentally (top row) and numerically (bottom row) at *Re*=3.5. Color code: blue (0) - green (0.5) - red (1).

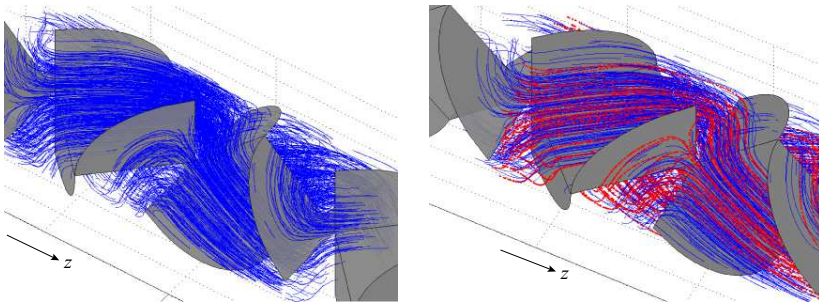
Figure 6.5: Measured (blue) and simulated (red) 3-D streamlines in a periodic segment of the Quatro mixer for *Re*=3.5.

streamline pattern. At the inlet of the geometry the throughflow is divided into two adjacent streams by the elliptical upstream parts. Within the first element, each stream is subjected to a lateral deflection due to the enforcement of the geometric boundaries. Then, parts of these adjacent streams confluence in the close proximity of the elliptical segments of the upstream element. The division and the confluence of streams proceed till the outlet of the mixing geometry. This reveals larger-scale coherence in the streamline pattern,

yet does not resolve small-scale coherent structures (e.g. stream tubes). Overall, the experimental and numerical coherent structures exhibit a good qualitative agreement.

6.5. ADVECTIVE-DIFFUSIVE SCALAR TRANSPORT ANALYSIS

This section presents a comparative analysis between experimental observations and numerical simulations on the cross-sectional evolution of the 3D scalar field in the Quatro mixer. The experiments concerns the scalar transport in the limit of infinite-Pe, yet in the numerical simulations accurate computations are possible only up to $Pe = 1000$ due to the restriction imposed by the numerical resolution. An extensive eigenmode analysis is conducted on the downstream evolution of the numerical scalar field via DMD algorithm and the isosurfaces of the period-wise evolution are used to visualize the stretching-folding mechanisms of the scalar transport. The results are given below.

The advective-diffusive scalar transport is investigated for the configuration given in Section 6.2.1. The model of the mixer consists of 10 periodic segments (7 periodic segments in the experiments) each of which is composed of two mixing elements. In experimental data processing, the 2D cross-sectional scalar distributions representing the downstream evolution are extracted from the 3D data set at the mid-plane of every second mixer element rather than the inlet/outlet planes of the periodic elements. This is due to the fact that in the experiments the edges of the mixer elements deteriorate the image quality and the selected cross-sections are the ones which suffer the least from the disturbance by the edges of the elements. The same procedure is also applied to the numerical scalar fields to be consistent.

Figure 6.6 shows the numerical (top, color) and experimental (bottom, gray scale) downstream evolution of an initially non-uniform scalar field in the Quatro mixer. The inflow is composed of two scalar concentration levels (i.e. $C|_{\text{inlet}} = 1$ for $y > 0$ and $C|_{\text{inlet}} = 0$ for $y < 0$). As the flow passes through the mixing elements, initially segregated concentration field breaks into smaller-scale structures by the effect of stretching-cutting processes and, the diffusion, in the case of finite-Pe, smooths the high-gradient regions. Here, the downstream evolution is dynamically similar to the temporal evolution in 2D time-periodic systems: the concentration field at the inlet transforms into persistent patterns and evolves self-similarly with decreasing variance, as shown in Fig. 6.6. Comparison between experimental and numerical scalar fields reveals that the overall patterns (especially for the earlier periods) agree well. The primary difference is that the experimental evolution continues to develop into ever finer structures while the simulated evolution fairly quickly becomes (nearly) homogeneous. This is due to the substantial difference in Pe and thus the far greater dominance of advection in the experimental case. Moreover, the experimental pattern clearly reveals a continuous process of stretching and cutting of material, which is an experimental evidence of chaotic advection. Finer structures emerging in the experiments show that the experiments in fact outperform the simulations by revealing far greater detail.

On the basis of symmetry in the geometry and the flow field, there exist a clear anti-symmetry in cross-sectional scalar patterns, which is shown in Fig. 6.7. This anti-symmetry property is very accurately present in the numerical results, yet it is less pronounced in the experiments due to imperfections in the facility. The anti-symmetry anal-
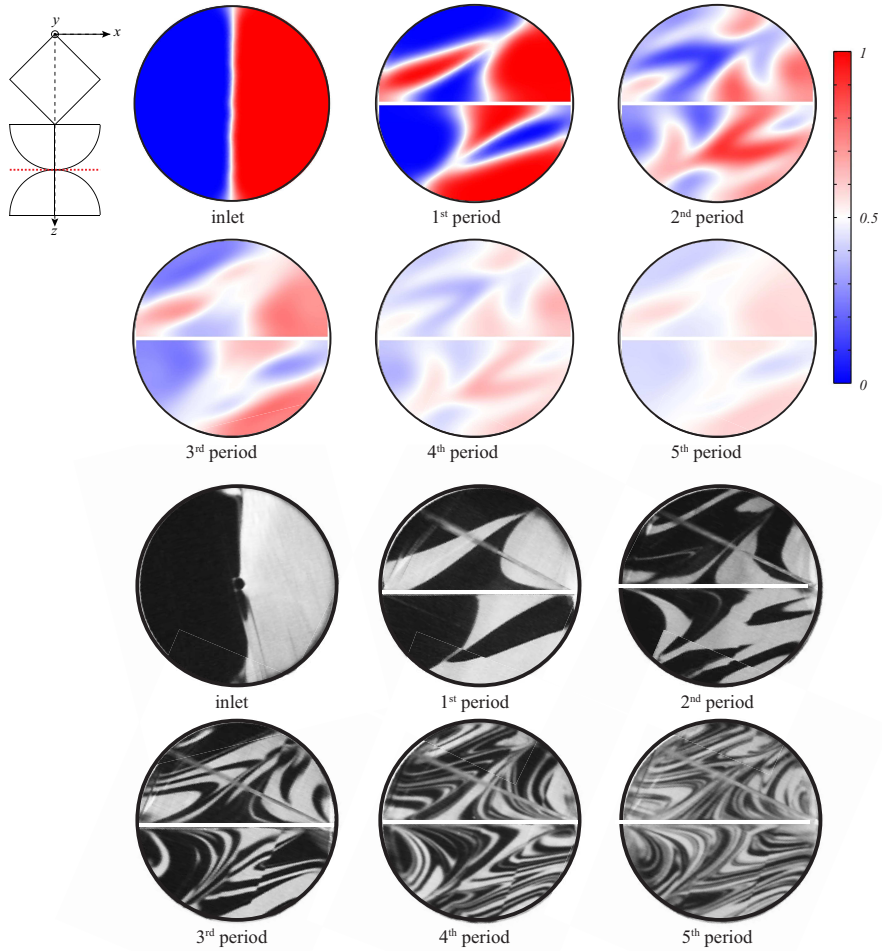
Figure 6.6: Cross-sectional contour plots of numerical (colored) and experimental (gray scale) scalar distributions. The color range from 0 to 1 (dimensionless scalar field) is indicated from blue to red in the numerical results and black to white in the experimental results. The patterns are plotted for the dimensionless periods from 0 to 5. $Re = 3.5$ and $Pe = 1000$. Red dashed line on the leftmost figure indicates the cross-sectional plane that the data is extracted.

ysis is only shown for the first two patterns of the evolution, since for higher n values the comparisons are not very clear anymore due to the very fine structures in the experimental scalar fields.

The normalized numerical scalar fields in Fig. 6.8 reveal a period-2 behavior, implying that the evolution is dominated by period-2 eigenmodes $\varphi_1(x, y)$ and $\varphi_2(x, y)$. The corresponding eigenvalues are in the form of $\lambda_j = |\lambda| e^{2\pi i j/p}$ where $j = 0, 1$ and the periodicity p is 2. Here, the magnitude of the exponential decay rate $|\lambda| = e^{\sigma}$ with $\sigma = \sigma_1 = \sigma_2 < 0$. This
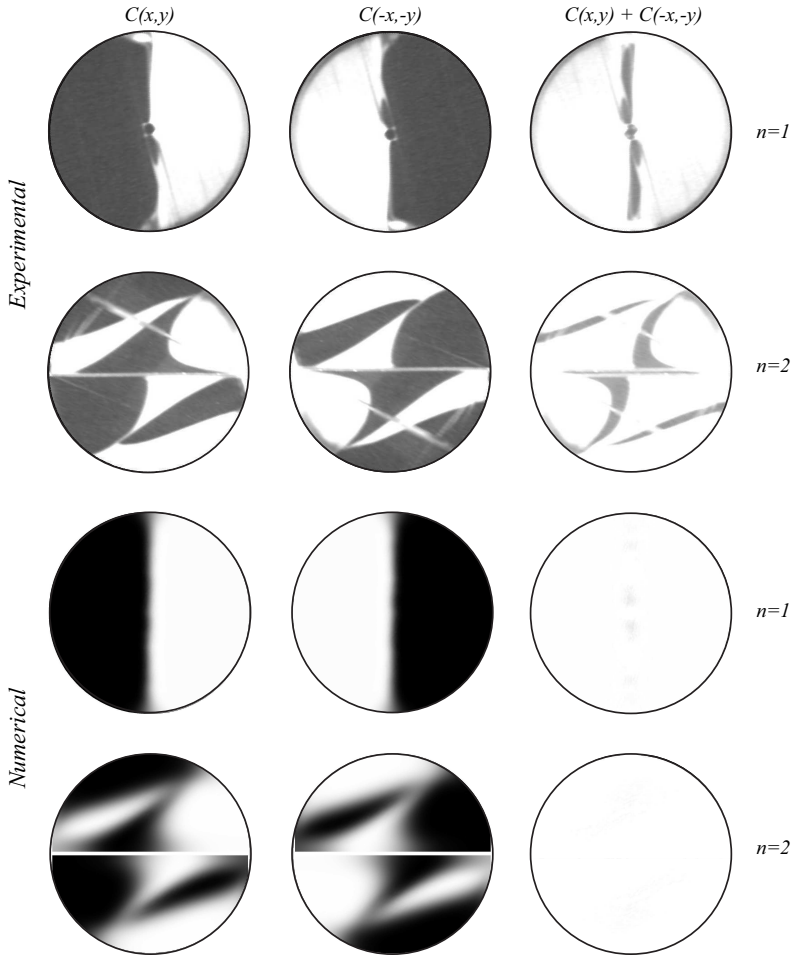
Figure 6.7: Anti-symmetry in the scalar field for the first two patterns of the evolution, where $n = 1, 2$. Top two row: experiments, bottom two raw: numerics.

leads to period-2 eigenvalues which can be written as $\mu_1 = \sigma$ and $\mu_2 = \sigma + i\pi$ and implies that both eigenmodes $\varphi_1(x, y)$ and $\varphi_2(x, y)$ decay with the same rate e^{σ}. The imaginary component of μ_2, that is $\omega_2 = \pi$, acts as an identity operator for $\varphi_2(x, y)$ for time spans of 2 periods (i.e. $e^{\pi i n} = (-1)^n$). Hence, the evolution of the concentration can be defined by the reduced expansion

$$C(x, y, nZ) = \sum_{k=1}^{2} \gamma_k \varphi_k(x, y) e^{\mu_k nZ} + C_{\infty}. \tag{6.9}$$

where C_{∞} is the homogeneous state where $C_{\infty} = 0.5$.

Eigenmode decomposition (Eq. 6.9) is verified by performance of DMD on simulated data. This gives the decomposition as shown in Fig. 6.9. The eigenvalues calculated by
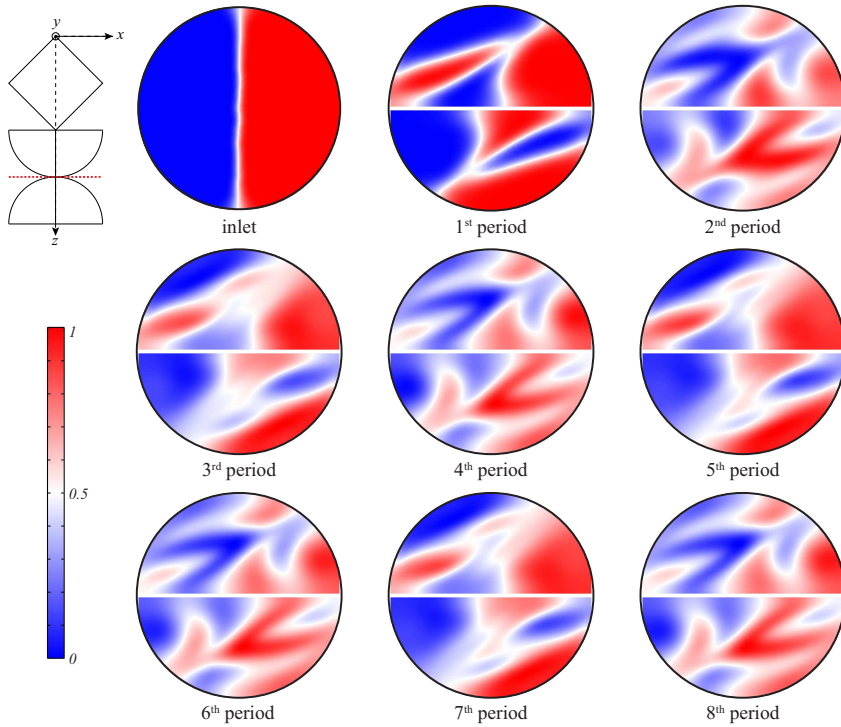
Figure 6.8: The normalized evolution of the numerical concentration field (each contour plot is normalized by its own maximum and minimum values). The color range from 0 to 1 (dimensionless scalar field) is indicated from blue to red. The patterns are plotted for the dimensionless periods from 0 to 8. $Re = 3.5$ and $Pe = 1000$. Red dashed line on the leftmost figure indicates the cross-sectional plane that the data is extracted.
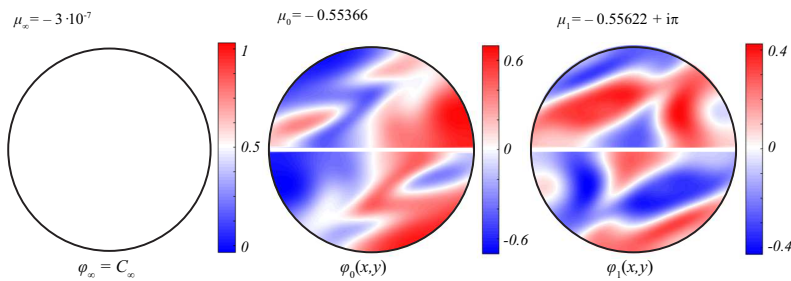

Figure 6.9: The first three dominant eigenmodes of the numerical simulation for the case Pe=1000, Re=3.5 and Λ=1. DMD is applied on the numerical data set to obtain the dominant eigenmodes.

DMD is in accordance with the theory, such that the real part of the eigenvalues is the same (i.e., $\sigma_1 = \sigma_2 = \sigma \approx -0.55$) and the imaginary parts are $w_1 = 0$ and $w_2 = \pi$ as given by the theory (Singh et al., 2009).

As mentioned above, the evolution is dominated by the eigenmodes, which are shown in Fig. 6.9, such that the linear combination of these two eigenmodes gives the repeating
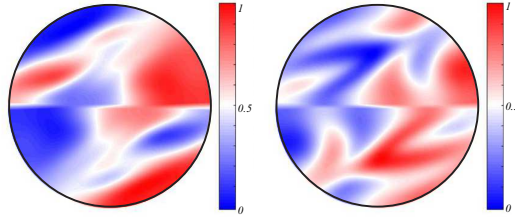
Figure 6.10: Linear combination of the dominant eigenmodes: $\varphi_0 + \varphi_1$ (left), $\varphi_0 - \varphi_1$ (right)

patterns of the evolution (Fig. 6.8): for even values of n, the repeating pattern is given by $\varphi_1 + \varphi_2$ (Fig 6.10, left) and for odd values of n, the pattern is calculated as $\varphi_1 - \varphi_2$ (Fig 6.10, right).

In addition to the eigenmode analysis, 3D isosurfaces of the normalized scalar field is visualized and supported by 2D cross-sectional scalar fields to investigate the behavior of the 3D scalar field under the effect of stretching and folding mechanisms. Since the scalar fields in Figure 6.11 are normalized (it is the only way to visualize continuous patterns from the inlet to the outlet of the mixing geometry), the structures should not be interpreted as the non-mixing tubes. The discussion becomes clearer when the isosurfaces given in Fig. 6.11(a) and (b) are analyzed together with the 2D normalized scalar patterns shown in Fig. 6.11(c). Owing to the fact that the scalar fields are anti-symmetric, only the regions shown by red will be discussed hereafter. At $z' = 0$ the scalar field has 4 red regions, which are tagged by the numbers (only the regions tagged by *1* and *2* are shown in isosurface plots). When $z' = L/2$ the region *1* and *2* are split into two (stretching and cutting) by the leading edge of the next element (*1-1*, *1-2* and *2-1*, *2-2*) and region *4* confluence with region *2-1* (folding). Till $z' = 3L/2$ the isosurfaces follow the mixing geometry and at $z' = 3L/2$ the regions *2-1* and *1-2* are divided into two again, which increases the interface between red and blue regions. Just after $z' = 3L/2$, two regions *1-1* and *2-1-1* merge, creating a new region *5*, which can clearly be seen in Fig. 6.11(a). Stretching, cutting and folding continues till the end of the geometry. The last pattern of the evolution is the same as the first pattern, yet the compositions of the patterns occupying the same region (i.e. region *1* at $z' = 0$ and region *5-2-2* at $z' = 4L$) are not the same after several stretching, cutting and folding cycles, which implies that the mixing in the Quatro mixing is efficient.

The intensity of segregation is also calculated at the cross-sections used for the eigenmode analysis. Figure 6.12 shows that the intensity of segregation decays exponentially similar to the decay of eigenmodes. The oscillatory behavior of the decay in the intensity of segregation also confirms the alternating behavior of the system between two repeating patterns.

6.6. CONCLUSION

This chapter has shown that the application of an advanced calibration procedure (see Chapter 2) together with a moving-average low-pass filter improved the accuracy of the 3D PTV measurements by decreasing the uncertainty in the measurement of particle positions from 10-15 % (Jilisen et al., 2013) to the range of 3-7 %. Moreover, this study has con-
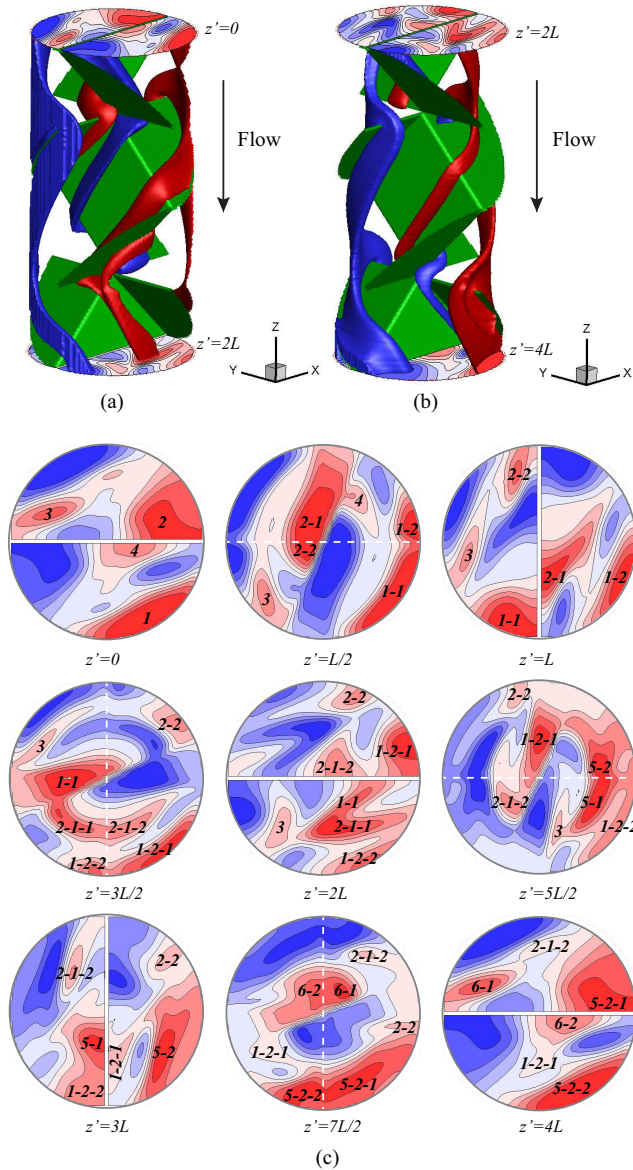
Figure 6.11: Isosurfaces and cross-sectional patterns of the normalized scalar field for two periodic elements: (a) isosurfaces for the 4th period of evolution ($C = 0.1$ (blue) and $C = 0.9$ (red)), (b) isosurfaces for the 5th period of evolution ($C = 0.1$ (blue) and $C = 0.9$ (red)) and (c) cross-sectional scalar patterns of the evolution for two periodic elements (from $z' = 0$ to $z' = 4L$). Red regions are tagged in the 2D patterns to make the track of the merging-splitting isosurfaces easier. The dashed lines indicate the leading edge of the elliptical segments of the downstream elements.

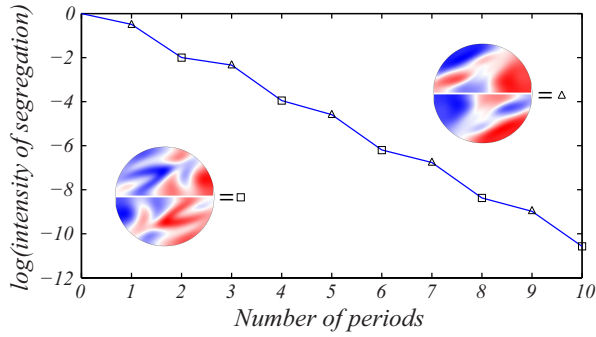firmed that the periodic flow assumption holds true for the flows inside spatially-periodic inline mixers at low-Re.

Figure 6.12: Logarithmic decay of intensity of segregation for the case *Pe*=1000, *Re*=3.5 and Λ=1.

The results of this chapter show that CFD modeling of 3D mixing is not yet powerful enough to reveal fine scale structures in high-*Pe* transport. To do this properly, one requires careful experimentation as we demonstrate with the Quatro mixer study. On the other hand, even with its limitations CFD can still be used to obtain the dominant eigenmodes of the scalar field evolution.

Overall, this study verifies the fidelity of both experimental setups for further studies in different complex mixing geometries.

7

CONCLUSIONS AND RECOMMENDATIONS

7.1. Conclusions

The work presented in this thesis deepens insight into the fundamentals of advective-diffusive scalar transport in inline mixing systems via laboratory experiments and numerical simulations. The study concerns the scalar transport in both 2D time-periodic and 3D steady spatially-periodic flows, and adopts the Rotated Arc Mixer (RAM) and the Quatro static mixer as the representative configurations. In Chapter 1, a brief introduction to scalar transport in laminar flows from both Lagrangian and Eulerian point of view is given. The scalar transport in inline mixing flows is summarized and the representative case studies are introduced. The research objectives of the present investigation are also given in this chapter. Chapter 2 gives an overview of the experimental facilities and techniques developed and employed in the current study. In Chapter 3, the entire Hamiltonian progression of the Lagrangian dynamics from integrable to chaotic state is investigated experimentally in the 2D time-periodic RAM via Poincaré sections and the experimental results are compared with the numerical counterparts. Chapter 4 broadens the analysis in Chapter 3 by a coupled experimental and computational study on the eigenmodes of the scalar transport in the simplified RAM. This is investigated for both only-advective and advective-diffusive cases. Chapter 5 expands on the analysis in Chapter 4 by presenting a parametric study on advective-diffusive scalar transport in the 2D time-periodic RAM and discusses the influence of geometrical (i.e. reorientation angle) and temporal (i.e. reorientation frequency) parameters on the mixing quality. This is also a comparative experimental-computational analysis. Chapter 6 reveals a coupled experimental and numerical analysis on the downstream evolution of 3D flow and scalar fields in the Quatro mixer. As a general conclusion, the experimental results agree well with the numerical counterparts and especially in the advective limit (i.e. in the limit of infinite-Pe) the experiments reveal far more details in the scalar fields compared to the numerical simulations, which promotes that the experimental methods and tools used in the current study are promising for further investigation of the mixing characteristics of inline mixing systems at different flow conditions. More specific conclusions are presented as follows:

The global Hamiltonian progression of Lagrangian dynamics from integrable to chaotic state in 2D time-periodic flows

The experimental investigation of the Lagrangian dynamics of passive tracers in 2D time-periodic RAM flow validates the assumption that Hamiltonian mechanisms rule over the Lagrangian dynamics of passive tracers in the considered flow class. The experimental investigation in Chapter 3 corroborates, via direct measurement of Poincaré sections, the hypothesis that a 2D time-periodic flow system is identical to time-dependent one degree-of-freedom Hamiltonian system: the Lagrangian flow topologies in the limit of steady flow comprise isolated flow regions and an increase in the flow period causes the disintegration of the Hamiltonian into regular (non-mixed) and chaotic (mixed) regions. Further increase in the flow period shrinks the size of the non-mixed regions. The experimental Poincaré section technique gives good results and can be used in any other similar flow.

THE EIGENMODES OF THE ADVECTIVE-DIFFUSIVE SCALAR TRANSPORT IN 2D TIME-PERIODIC FLOWS

The results of this chapter show that there is a good agreement between the dominant eigenmodes of the ADE and the DMD analysis on the experimental and numerical data sets. A quantitative analysis of the scalar field confirms that when diffusion is effective, self-similarly decaying patterns dominate the scalar field evolution and the evolution can be simplified to a spatial structure and a decay rate pair which has the slowest decay rate, which is consistent with the literature. In the limit of zero-diffusivity, however, the self-similarly decaying structure turns into a complex spatial structure with non-decaying gradients and increasing complexity. The methods and tools employed in this study validate the eigenmode approach and the results of different methods support each other.

Despite the imperfections in the experimental facility, such as heat losses in the temperature field experiments, the results of the concentration (dye) and temperature field experiments show similar characteristics: the evolution is dominated by a persistent pattern, the overall structure of which is the same in both cases. The dye experiments give more detailed information on the complex spatial structure of the repeating pattern.

THE EFFECT OF GEOMETRICAL AND TEMPORAL PARAMETERS ON THE EVOLUTION OF SCALAR PATTERNS IN 2D TIME-PERIODIC FLOWS

The comparison of the numerical Poincaré sections for 2D time-periodic RAM and 3D spatially-periodic RAM flows validates that despite the differences in the size and orientation of topological structures, the two case share similar features indicative of mixed and non-mixed regions, which substantiates the suitability of 2D time-dependent RAM flow for the qualitative analysis of mixing in 3D duct flows.

The numerical Poincaré sections are used to obtain the regime diagram in the parameter space of $-4\pi/5 \le \Theta \le \pi$ and $0.1 \le \tau \le 10$. In general, negative Θ cases reach a globally chaotic state with increasing τ. On the other hand, the non-mixed regions persist in the scalar fields for positive Θ. These observations are in accordance with the findings in the literature. The overall agreement in numerical and experimental outcomes concludes that the setup can be further used to determine the most efficient protocols.

The dye visualizations provide greater level of details for changing Θ and τ parameters in relation to Lagrangian dynamics presented by the Poincaré maps. Quantitative analysis of the mixing quality based on the intensity of segregation reveals the effects of control parameters on the mixing efficiency. It is clearly shown that negative Θ and relatively high switching period ($\tau > 5$) achieve a good mixing, whereas the mixing efficiency is low for $\tau < 2$, independent of Θ. There is a region in the parameter space bounded by $0 < \Theta < \pi/2$, which indicates poor mixing performance even after a long time ($t^* = 80\tau$).

Varying-Θ protocols combine the $\Theta = \pi$ case, where the chaos emerges in the center of the circular domain, with other non-zero Θ cases, for which the chaotic state is initially reached in the vicinity of the walls and, as a result, enhances the mixing efficiency. This varying-Θ strategy lowers the value of τ at which globally chaotic state is attained for a given non-varying Θ. Disintegrating effect of $\Theta = \pi$ protocol paves the way for achieving a fully chaotic state even for positive Θ_2 cases, which otherwise accommodates an elliptical island in the flow topology. The success of the combined forcing strategy implies that flow

topologies and scalar field evolutions acquired for systematically varying control parameters can be used to define an optimum set of parameters to achieve an improved mixing quality in generic 3D reoriented duct flows.

Scalar transport in 3D spatially-periodic systems

The results of this chapter show that the scalar field evolution in the Quatro mixer is dominated by a pair of exponentially decaying period-2 eigenmodes. In the limit of infinite-Pe, the evolution is governed by the non-decaying eigenmodes. However, this case can not be verified by the experimental results due to (1) highly complex structure of the scalar patterns; (2) insufficient number of cross-sectional scalar fields.

The results of the concentration field measurements show that the 3D LIF measurements are capable of revealing greater level of details in scalar patterns compared to the numerical simulations which suffer from the fact that accurate computations are possible only up to $Pe \approx 1000$ due to the restriction imposed by the numerical resolution. Fine details in the numerical results are smeared out by diffusion. Moreover, experimental data displays the effects of stretching and cutting mechanisms on the scalar fields.

7.2. Recommendations

The work presented in this thesis is limited to the cases where the mixing occurs between rheologically-equivalent (e.g. the density and viscosity of the mixing fluids are the same) and Newtonian fluids. However, based on the fact that mixing of rheologically-equivalent flows is only a part of the industrial mixing processes, studying the effects of non-equivalent fluid properties on the mixing qualities might expand the knowledge in fluid mixing processes. Implementation of non-equivalent fluid properties in current theoretical/numerical research tools may increase the complexity, yet it can easily be handled in the current experimental facilities/tools and can be studied comprehensively. The only thing that needs to be done, by keeping in mind the optical properties of the system such as refractive index, is the replacement of the working fluid (i.e. silicone oil) with the new one that meets the requirements. This may lead to further modifications in the experimental facility, such as replacement of the pumps, yet it should not be a problem. Here, it should be highlighted that the present study opens the ways to investigate more complex mixing problems from an experimental point of view and it opens a whole application area.

In addition to the effect of non-equivalent fluid properties on the mixing quality, the effect of inertia (Re>0) on the mixing qualities has not been considered in this thesis. There are numerical studies focusing on the flow and mixing behavior in inertial flows, yet the experimental work in this topic is scarce. The next step might be the investigation of the response of scalar fields to varying Re values. For this purpose, both the simplified RAM and the Quatro mixer facilities can be employed with slight changes in the settings. One may consider the use of silicone oils with different viscosities.

The last but not the least, the effect of different mixing protocols with varying-Θ (different than the ones discussed in this thesis) can be studied to find the optimum mixing protocol that achieves global mixing with the smallest possible τ. The experimental work presented in thesis only considers the non-varying Θ cases, yet with the simplified RAM

facility it is possible to study the effects of varying Θ on the mixing efficiency experimentally. Therefore, as a future work an experimental parametric analysis on varying Θ can be performed in the simplified RAM facility.

BIBLIOGRAPHY

Adrover A, Cerbelli S, Giona M (2001) On the interplay between advection and diffusion in closed laminar chatic flows. J Phys Chem A 105:4908

Akkermans RAD, Kamp LPJ, Clercx HJH, van Heijst GJF (2008) Intrinsic three-dimensionality in electromagnetically driven shallow flows. EPL 83:24,001

Akkermans RAD, Kamp LPJ, Clercx HJH, van Heijst GJF (2010) Three-dimensional flow in electromagnetically driven shallow two-layer fluids. Phys Rev E 82:026,314

Alvarez MM, Guzmán A, Elías M (2005) Experimental visualization of mixing pathologies in laminar stirred tank bioreactors. Chemical engineering science 60(8):2449–2457

Antonsen Jr TM, Fan Z, Ott E, Garcia-Lopez E (1996) The role of chaotic orbits in the determination of power spectra of passive scalars. Physics of Fluids 8(11):3094–3104

Aref H (1984) Stirring by chaotic advection. Journal of Fluid Mechanics 143:1–21

Aref H (2002) The development of chaotic advection. Physics of Fluids 14(4):1315–1325

Aref H, Balachandar S (1986) Chaotic advection in a Stokes flow. Physics of Fluids 29(11):3515–3521

Aref H, Blake JR, Budišić M, Cartwright JH, Clercx HJ, Feudel U, Golestanian R, Gouillart E, Guer YL, van Heijst GF, et al. (2014) Frontiers of chaotic advection. arXiv preprint arXiv:14032953

Arratia PE, Shinbrot T, Alvarez MM, Muzzio FJ (2005) Mixing of non-Newtonian fluids in steadily forced systems. Physical review letters 94(8):084,501

Avalosse T, Crochet MJ (1997) Finite-element three-dimensional simulation of mixing: 2. flow through a Kenics mixer. AIChE J 43:588

Bajer K (1994) Hamiltonian formulation of the equations of streamlines in three-dimensional steady flows. Chaos, Solitons & Fractals 4(6):895–911

Bajer K, Moffatt HK (1990) On a class of steady confined Stokes flows with chaotic streamlines. Journal of Fluid Mechanics 212:337–363

Baskan O, Speetjens MFM, Metcalfe G, Clercx HJH (2015) Experimental and computational study of scalar modes in a periodic laminar flow. International Journal of Thermal Sciences 96:102–118

Becht S, Franke R, elmann AG, Hahn H (2007) Micro process technology as a means of process intensification. Chem Eng Technol 30:295

Beebe DJ, Mensing GA, Walker GM (2002) Physics and applications of microfluidics in biology. Rev Biomed Engng 4:261

Bejan A (1995) Convection Heat Transfer. Wiley

Bertsch A, Heimgartner S, Cousseau P, Renaud P (2001) Static micromixers based on large-scale industrial mixer geometry. Lab Chip 1:56

Boyland PL, Aref H, Stremler MA (2000) Topological fluid mechanics of stirring. Journal of Fluid Mechanics 403:277–304

Budwig R (1994) Refractive index matching methods for liquid flow investigations. Experiments in Fluids 17(5):350–355

Byrde O, Sawley ML (1999) Optimization of a Kenics static mixer for non-creeping flow conditions. Chem Engng J 72:163

Cartwright JHE, Feingold M, Piro O (1996) Chaotic advection in three-dimensional unsteady incompressible laminar flow. Journal of Fluid Mechanics 316:259–284

Castelain C, Mokrani A, Guer YL, Peerhossaini H (2001) Experimental study of chaotic advection regime in a twisted duct flow. European Journal of Mechanics - B/Fluids 20(2):205–232

Chagny C, Castelain C, Peerhossaini H (2000) Chaotic heat transfer for heat exchanger design and comparison with a regular regime for a large range of Reynolds numbers. Appl Thermal Engng 20:1615

Chaiken J, Chevray R, Tabor M, Tan QM (1986) Experimental study of Lagrangian turbulence in a Stokes flow. Proceedings of the Royal Society of London A Mathematical and Physical Sciences 408(1834):165–174

Cheng CQ, Sun YS (1989) Existence of invariant tori in three-dimensional measure-preserving mappings. Celestial Mechanics and Dynamical Astronomy 47(3):275–292

Cheng Y, Diez FJ (2011) A 4D imaging tool for Lagrangian particle tracking in stirred tanks. AIChE Journal 57(8):1983–1996

Chien W, Rising H, Ottino JM (1986) Laminar mixing and chaotic mixing in several cavity flows. Journal of Fluid Mechanics 170:355–377

Christov IC, Ottino JM, Lueptow RM (2010) Chaotic mixing via streamline jumping in quasi-two-dimensional tumbled granular flows. Chaos: An Interdisciplinary Journal of Nonlinear Science 20(2):023,102

Cisar SE, Umbanhowar PB, Ottino JM (2006) Radial granular segregation under chaotic flow in two-dimensional tumblers. Physical Review E 74(5):051,305

Danckwerts P (1952) The definition and measurement of some characteristics of mixtures. Applied Scientific Research, Section A 3(4):279–296

DeMartini BE, Butterfield HE, Moehlis J, Turner KL (2007) Chaos for a microelectromechanical oscillator governed by the nonlinear Mathieu equation. Microelectromechanical Systems, Journal of 16(6):1314–1323

Dombre T, Frisch U, Greene JM, Hénon M, Mehr A, Soward AM (1986) Chaotic streamlines in the ABC flows. J Fluid Mech 167:353–391

Fiedor SJ, Ottino JM (2005) Mixing and segregation of granular matter: multi-lobe formation in time-periodic flows. Journal of Fluid Mechanics 533:223–236

Finn MD, Thiffeault JL, Gouillart E (2006) Topological chaos in spatially periodic mixers. Phys D 221:92–100

Fogleman MA, Fawcett MJ, Solomon TH (2001) Lagrangian chaos and correlated Lévy flights in a non-Beltrami flow: Transient versus long-term transport. Physical Review E 63(2):020,101

Fountain GO, Khakhar DV, Ottino JM (1998) Visualization of three-dimensional chaos. Science 281:683

Fountain GO, Khakhar DV, Mezic I, Ottino JM (2000) Chaotic mixing in a bounded three-dimensional flow. Journal of Fluid Mechanics 417:265–301

Franjione JG, Ottino JM (1992) Symmetry concepts for the geometric analysis of mixing flows. Philosophical Transactions of the Royal Society of London A: Mathematical, Physical and Engineering Sciences 338(1650):301–323

Franjione JG, Leong CW, Ottino JM (1989) Symmetries within chaos: a route to effective mixing. Physics of Fluids A: Fluid Dynamics) 1(11):1772–1783

Galaktionov OS, Anderson PD, Peters GWM, Meijer HEH (2002) Morphology development in Kenics static mixers (application of the extended mapping method). The Canadian Journal of Chemical Engineering 80(4):604–613

Galaktionov OS, Anderson PD, Peters GWM, Meijer HEH (2003) Analysis and optimization of Kenics static mixers. International Polymer Processing 18(2):138–150

Gorodetskyi O, Speetjens MFM, Anderson PD, Giona M (2014) Analysis of the advection-diffusion mixing by the mapping method formalism in 3D open-flow devices. AIChE Journal: Chemical Engineering Research and Development 60(1):387–407

Gottwald JA, Virgin LN, Dowell EH (1992) Experimental mimicry of Duffing's equation. Journal of Sound and Vibration 158(3):447–467

Gouillart E, Thiffeault JL, Finn MD (2006) Topological mixing with ghost rods. Phys Rev E 73:036,311

Gouillart E, Kuncio N, Dauchot O, Dubrulle B, Roux S, Thiffeault J (2007) Walls inhibit chaotic mixing. Physical review letters 99(11):114,501

Gouillart E, Dauchot O, Dubrulle B, Roux S, Thiffeault JL (2008) Slow decay of concentration variance due to no-slip walls in chaotic mixing. Phys Rev E 78:026,211

Hackborn WW, Ulucakli ME, Yuster T (1997) A theoretical and experimental study of hyperbolic and degenerate mixing regions in a chaotic Stokes flow. Journal of Fluid Mechanics 346:23–48

Haller G (2015) Lagrangian coherent structures. Annu Rev Fluid Mech 47:137

Hirech K, Arhaliass A, Legrand J (2003) Experimental investigation of flow regimes in an SMX Sulzer static mixer. Ind Eng Chem Res 42:1478

Hwu T, Young D, Chen Y (1997) Chaotic advections for Stokes flows in circular cavity. J Eng Mech 123(8):774–782

Jaffer SA, Wood PE (1998) Quantification of laminar mixing in the Kenics static mixer: an experimental study. Can J Chem Eng 76:516

Jaluria Y (2003) Thermal processing of materials: from basic research to engineering. ASME J Heat Transfer 125:957

Jana SC, Metcalfe G, Ottino JM (1994a) Experimental and computational studies of mixing in complex Stokes flows: the vortex mixing flow and multicellular cavity flows. Journal of Fluid Mechanics 269:199–246

Jana SC, Tjahjadi M, Ottino JM (1994b) Chaotic mixing of viscous fluids by periodic changes in geometry: baffled cavity flow. AIChE journal 40(11):1769–1781

Jilisen RTM (2011) Development of a 3D flow measurement system for industrial mixing processes. Master's thesis, Eindhoven University of Technology

Jilisen RTM, Bloemen PR, Speetjens MFM (2013) Three-dimensional flow measurements in a static mixer. AIChE Journal: Chemical Engineering Research and Development 159(5):1746–1761

Khakhar DV, McCarthy JJ, Gilchrist JF, Ottino JM (1999) Chaotic mixing of granular materials in two-dimensional tumbling mixers. Chaos: An Interdisciplinary Journal of Nonlinear Science 9(1):195–205

Krasnopolskaya TS, Meleshko VV, Peters GWM, Meijer HEH (1999) Mixing in Stokes flow in an annular wedge cavity. European Journal of Mechanics-B/Fluids 18(5):793–822

Kumar V, Shirke V, Nigam KDP (2008) Performance of Kenics static mixer over a wide range of Reynolds number. Chemical Engineering Journal 139(2):284–295

Kundu PK, Cohen IM (1990) Fluid Mechanics. Academic Press

Kusch HA, Ottino JM (1992) Experiments on mixing in continuous chaotic flows. Journal of Fluid Mechanics 236:319–348

Leong CW, Ottino JM (1989) Experiments on mixing due to chaotic advection in a cavity. Journal of Fluid Mechanics 209:463–499

Lester DR, Metcalfe G, Rudman M (2007) Complete parametric scalar dispersion. In: Microelectronics, MEMS, and Nanotechnology, International Society for Optics and Photonics, pp 68,020J–68,020J

Lester DR, Rudman M, Metcalfe G, Blackburn HM (2008) Global parametric solutions of scalar transport. J Comput Phys 227:3032

Lester DR, Rudman M, Metcalfe G (2009) Low Reynolds number scalar transport enhancement in viscous and non-Newtonian fluids. Int J Heat Mass Transfer 52:655

Lester DR, Metcalfe G, Rudman M (2014) Control mechanisms for the global structure of scalar dispersion in chaotic flows. Physical Review E 90(2):022,908

Li HZ, Fasol C (1997) Pressure drop of newtonian and non-newtonian fluids across a Sulzer SMX static mixer. Trans IChemE 75:792

Liu W, Haller G (2004) Strange eigenmodes and decay of variance in the mixing of diffusive tracers. Physica D: Nonlinear Phenomena 188(1):1–39

Lüthi B, Tsinober A, Kinzelbach W (2005) Lagrangian measurement of vorticity dynamics in turbulent flow. Journal of Fluid mechanics 528:87–118

Malyuga VS, Meleshko VV, Speetjens MFM, Clercx HJH, van Heist GJF (2002) Mixing in the stokes flow in a cylindrical container. Proceedings of the Royal Society of London Series A 458(2024):1867–1885

Meagher RJ, Hatch AV, Renzi R, Singh AK (2008) An integrated microfluidic platform for sensitive and rapid detection of biological toxins. Lab Chip 8:2046

Meier SW, Lueptow RM, Ottino JM (2007) A dynamical systems approach to mixing and segregation of granular materials in tumblers. Advances in Physics 56(5):757–827

Meleshko V, Galaktionov O, Peters G, Meijer H (1999) Three-dimensional mixing in Stokes flow: the partitioned pipe mixer problem revisited. European Journal of Mechanics - B/Fluids 18(5):783–792

Meleshko VV, Peters GWM (1996) Periodic points for two-dimensional stokes flow in a rectangular cavity. Physics Letters A 216:87–96

Metcalfe G, Rudman M, Brydon A, Graham LJW, Hamilton R (2006) Composing chaos: an experimental and numerical study of an open duct mixing flow. AIChE journal 52(1):9–28

Metcalfe G, Speetjens MFM, Lester DR, Clercx HJH (2012) Beyond passive : chaotic transport in stirred fluids. Advances in Applied Mechanics 45:109–188

Mezic I (2013) Analysis of fluid flows via spectral properties of the Koopman operator. Annu Rev Fluid Mech 45:357–378

Mezić I, Wiggins S (1994) On the integrability and perturbation of three-dimensional fluid flows with symmetry. Journal of Nonlinear Science 4(1):157–194

Miles KC, Nagarajan B, Zumbrunen DA (1995) Three-dimensional chaotic mixing of fluids in a cylindrical cavity. Journal of Fluids Engineering 117(4):582–588

Mills PL, Quiram DJ, Ryley JF (2000) Microreactor technology and process miniaturization for catalytic reactions. A perspective on recent developments and emerging technologies. Chem Engng Sci 62:6992

Moon FC, Holmes PJ (1979) A magnetoelastic strange attractor. Journal of Sound and Vibration 65(2):275–296

Moon FC, Holmes WT (1985) Double Poincaré sections of a quasi-periodically forced, chaotic attractor. Physics Letters A 111(4):157–160

Moon FC, Li GX (1985) The fractal dimension of the two-well potential strange attractor. Physica D: Nonlinear Phenomena 17(1):99–108

Morozov AD, Kostromina OS (2014) On periodic perturbations of asymmetric Duffing–Van-der-Pol equation. International Journal of Bifurcation and Chaos 24(05):1450,061

Nguyen N, Wu Z (2005) Micromixers—a review. Journal of Micromechanics and Microengineering 15(2):R1

Nishio S, Murata S (2003) A numerical approach to the evaluation of error vector appearence possibility in PIV. In: Proceedings of 5th international symposium on particle image velocimetry, pp 3321.1–3321.9

Okamoto K, Nishio S, Saga T, Kobayashi T (2000) Standard images for particle image velocimetry. J Meas Sci Technol 11:685–691

Ott E (2002) Chaos in dynamical systems. Cambridge University Press

Ottino JM (1989) The kinematics of mixing: stretching, chaos, and transport, vol 3. Cambridge University Press

Ottino JM (1990) Mixing, chaotic advection and turbulence. Annual Review of Fluid Mechanics 22:207–253

Ottino JM, Leong CW, Rising H, Swanson PD (1988) Morphological structures produced by mixing in chaotic flows. Nature 333:419–425

Ottino JM, Jana SC, Chakravarthy VS (1994) From Reynolds's stretching and folding to mixing studies using horseshoe maps. Physics of Fluids 6:685–699

Otto F, Riegler EK, Voth GA (2008) Measurements of the steady streaming flow around oscillating spheres using three dimensional particle tracking velocimetry. Physics of Fluids 20(9):093,304

Pierrehumbert RT (1994) Tracer microstructure in the large-eddy dominated regime. Chaos, Solution Fractals 4:774

Pikovsky A, Popovych O (2003) Persistent patterns in deterministic mixing flows. Europhys Lett 61:625–631

Piro O, Feingold M (1988) Diffusion in three-dimensional Liouvillian maps. Phys Rev Lett 61:1799

Popovych OV, Pikovsky A, Eckhardt B (2007) Abnormal mixing of passive scalars in chaotic flows. Physical Review E 75(3):036,308

Pust O, Tyson S, Mathys P, Rütti A (2006) Quantification of laminar mixing performance using laser-induced fluorescence. In: 13th Int Symp on Applications of Laser Techniques to Fluid Mechanics, Lisbon, Portugal

Raffel M, Willert C, Wereley S, Kompenhans J (1998) Particle Image Velocimetry: A Practical Guide. Springer

Rajaei H (2013) Experimental and numerical investigation of flow field in a static mixer at low Reynolds number regime. Master's thesis, Eindhoven University of Technology

Reynolds O (1883) An experimental investigation of the circumstances which determine whether the motion of water shall be direct or sinuous, and of the law of resistance in parallel channels. Proceedings of the royal society of London 35(224–226):84–99

Rothstein D, Henry E, Gollub JP (1999) Persistent patterns in transient chaotic fluid mixing. Nature (London) 401:770

Roy PK, Basuray A (2003) A high frequency chaotic signal generator: A demonstration experiment. American Journal of Physics 71(1):34–37

Rulkov NF (1996) Images of synchronized chaos: Experiments with circuits. Chaos: An Interdisciplinary Journal of Nonlinear Science 6(3):262–279

Samelson RM, Wiggins S (2006) Lagrangian transport in geophysical jets and waves: the dynamical systems approach, vol 31. Springer Science & Business Media

Schmid PJ (2010) Dynamic mode decomposition of numerical and experimental data. J Fluid Mech 656:5–28

Schmid PJ (2011) Application of dynamic mode decomposition to experimental data. Exp Fluids 50:1123–1130

Shadden SC, Lekien F, Marsden JE (2005) Definition and properties of Lagrangian coherent structures from finite-time Lyapunov exponents in two-dimensional aperiodic flows. Phys D 212:271

Shinbrot T, Alvarez MM, Zalc JM, Muzzio FJ (2001) Attraction of minute particles to invariant regions of volume preserving flows by transients. Physical review letters 86(7):1207

Shivamoggi BK (2014) Nonlinear dynamics and chaotic phenomena: an introduction, vol 103. Springer

Siahmakoun A, French VA, Patterson J (1997) Nonlinear dynamics of a sinusoidally driven pendulum in a repulsive magnetic field. American Journal of Physics 65(5):393–400

Singh MK, Anderson PD, Speetjens MFM, Meijer HEH (2008) Optimizing the rotated arc mixer. AIChE J 54:2809–2822

Singh MK, Speetjens MFM, Anderson PD (2009) Eigenmode analysis of scalar transport in distributive mixing. Physics of Fluids 21(9):–

Solomon TH, Gollub JP (1988) Chaotic particle transport in time-dependent Rayleigh-Benard convection. Physical Review A 38(12):6280

Solomon TH, Weeks ER, Swinney HL (1993) Observation of anomalous diffusion and Lévy flights in a two-dimensional rotating flow. Physical Review Letters 71(24):3975

Solomon TH, Weeks ER, Swinney HL (1994) Chaotic advection in a two-dimensional flow: Lévy flights and anomalous diffusion. Physica D: Nonlinear Phenomena 76(1):70–84

Solomon TH, Tomas S, Warner JL (1996) Role of lobes in chaotic mixing of miscible and immiscible impurities. Physical review letters 77(13):2682

Solomon TH, Wallace BR, Miller NS, Spohn CJ (2003) Lagrangian chaos and multiphase processes in vortex flows. Communications in Nonlinear Science and Numerical Simulation 8(3):239–252

Sotiropoulos F, Webster DR, Lackey TC (2002) Experiments on Lagrangian transport in steady vortex-breakdown bubbles in a confined swirling flow. Journal of Fluid Mechanics 466:215–248

Speetjens MFM (2012) A generalised Lagrangian formalism for thermal analysis of laminar convective heat transfer. International Journal of Thermal Sciences 61:79–93

Speetjens MFM, Clercx HJH (2013) Formation of coherent structures in a class of realistic 3D unsteady flows. In: Klapp J, Medina A, Cros A, Vargas C (eds) Fluid Dynamics in Physics, Engineering and Environmental Applications, Part 1, Springer, pp 139–157

Speetjens MFM, van Steenhoven AA (2010) Visualisation of heat transfer in 3D unsteady flows. Int J Therm Sci 49:1103

Speetjens MFM, Clercx HJH, Heijst GJFV (2004) A numerical and experimental study on advection in three-dimensional stokes flows. Journal of Fluid Mechanics 514:77–105

Speetjens MFM, Metcalfe G, Rudman M (2006) Topological mixing study of non-Newtonian duct flows. Phys Fluids 18:103,103–1–103,103–11

Speetjens MFM, Lauret M, Nijmeijer H, Anderson PD (2013) Footprints of Lagrangian flow structures in Eulerian concentration distributions in periodic mixing flows. Physica D : Nonlinear Phenomena 250:20–33

Speetjens MFM, Demissie EA, Metcalfe G, Clercx HJH (2014) Lagrangian transport characteristics of a class of three-dimensional inline-mixing flows with fluid inertia. Physics of Fluids 26(11):113601

Stone HA, Stroock AD, Ajdari A (2004) Engineering flows in small devices: microfluidics toward a lab-on-a-chip. Annu Rev Fluid Mech 36:381

Strang G (1976) Linear algebra and its applications, (Harcourt Brace Jovanovich, San Diego)

Stremler MA, Chen J (2007) Generating topological chaos in lid-driven cavity flow. Physics of Fluids 19(10):103,602

Stremler MA, Ross SD, Grover P, Kumar P (2011) Topological chaos and periodic braiding of almost-cyclic sets. Phys Rev Lett 106:114,101

Stroock AD, McGraw GJ (2004) Investigation of the staggered herringbone mixer with a simple analytical model. Philos Trans R Soc Lond 362:971–

Sukhatme J, Pierrehumbert RT (2002) The decay of passive scalars under the action of single scale smooth velocity fields in bounded 2d domains: From non self similar pdf's to self similar eigenmodes. arXiv preprint nlin/0207012

Sunden B, Shah RK (2007) Advances in Compact Heat Exchangers. Edwards

Swanson PD, Ottino JM (1990) A comparative computational and experimental study of chaotic mixing of viscous fluids. Journal of Fluid Mechanics 213:227–249

Tel T, Károlyi G, Péntek A, Scheuring I, Toroczkai Z, Grebogi C, Kadtke J (2000) Chaotic advection, diffusion, and reactions in open flows. Chaos: An Interdisciplinary Journal of Nonlinear Science 10(1):89–98

Thakur RK, Vial C, Nigam KDP, Nauman EB, Djelveh G (2003) Static mixers in the process industries - A review. Chemical Engineering Research and Design 81(7):787–826

ThermaCAM^{TM} (2006) S65 HS User's Manual. FLIR Systems

Thiffeault JL, Finn MD (2006) Topology, braids, and mixing in fluids. Trans Royal Soc A 364:3251–3266

Ueno K, Shiga K, Sunada T, Morita S (2005) A mathematical gift: the interplay between topology, functions, geometry, and algebra, vol 3. American Mathematical Soc.

Voth GA, Haller G, Gollub JP (2002) Experimental measurements of stretching fields in fluid mixing. Physical review letters 88(25):254,501

Voth GA, Saint TC, Dobler G, Gollub JP (2003) Mixing rates and symmetry breaking in two-dimensional chaotic flow. Phys Fluids 15:2560

Wacker (2002) Silicone Fluids AK. Amber Composites

Weeks ER, Urbach JS, Swinney HL (1996) Anomalous diffusion in asymmetric random walks with a quasi-geostrophic flow example. Physica D: Nonlinear Phenomena 97(1):291–310

Weigl B, Labarre G, Domingo P, Gerlach J (2008) Towards non- and minimally instrumented, microfluidics-based diagnostic devices. Lab Chip 8:1999

Wiggins S (2005) The dynamical systems approach to Lagrangian transport in oceanic flows. Annu Rev Fluid Mech 37:295–328

Wiggins S, Ottino JM (2004) Foundations of chaotic mixing. Phil Trans R Soc Lond 362:937

Willneff J (2003) A spatio-temporal matching algorithm for 3D particle tracking velocimetry. PhD thesis, ETH Zurich

Wu F, Speetjens MFM, Vainchtein DL, Trieling RR, Clercx HJH (2014) Comparative numerical-experimental analysis of the universal impact of arbitrary perturbations on transport in three-dimensional unsteady flows. Phys Rev E 90:063,002

Yang HC (2007) Mixing characteristics of motionless mixers. J Visualization 10:83–89

Yi M, Qian S, Bau HH (2002) A magnetohydrodynamic chaotic stirrer. Journal of Fluid Mechanics 468:153–177

Znaien J, Speetjens MFM, Trieling RR, Clercx HJH (2012) Observability of periodic lines in three-dimensional lid-driven cylindrical cavity flows. Phys Rev E 85:066,320

LIST OF PUBLICATIONS

JOURNAL ARTICLES

- **O. Baskan**, M. F. M. Speetjens, G. Metcalfe, H. J. H. Clercx, *Experimental and computational study of scalar modes in a periodic laminar flow*, International Journal of Thermal Sciences **96**, 102–118, 2015.

- **O. Baskan**, M. F. M. Speetjens, G. Metcalfe, H. J. H. Clercx, *Direct experimental visualization of the global Hamiltonian progression of two-dimensional Lagrangian flow topologies from integrable to chaotic state, submitted to Chaos: An Interdisciplinary Journal of Nonlinear Science.*

- **O. Baskan**, M. F. M. Speetjens, G. Metcalfe, H. J. H. Clercx, *Experimental and numerical parametric analysis of a reoriented duct flow, submitted to EJMB/Fluids..*

- **O. Baskan**, H. Rajaei, M. F. M. Speetjens, H. J. H. Clercx, *Experimental and numerical investigation of scalar transport in an inline mixer, to be submitted to AIChE Journal.*

CONFERENCE PUBLICATIONS AND CONTRIBUTIONS

- **O. Baskan**, M. F. M. Speetjens, H. J. H. Clercx, *Experimental investigation of spatially-periodic scalar patterns in an inline mixer*, 67th Annual Meeting of the APS Division of Fluid Dynamics, San Francisco, California, the USA, November 23–25, 2014.

- **O. Baskan**, M. F. M. Speetjens, H. J. H. Clercx, *Experimental investigation of spatially-periodic scalar patterns in an inline mixer*, 10th European Fluid Mechanics Conference, Copenhagen, Denmark, September 14–18, 2014.

- M. F. M. Speetjens, **O. Baskan**, G. Metcalfe, H. J. H. Clercx, *Unravelling convective heat transfer in the rotated arc mixer*, Proceedings of the 15th International Heat Transfer Conference, Kyoto, Japan, August 10–15, 2014.

- **O. Baskan**, M. F. M. Speetjens, G. Metcalfe, H. J. H. Clercx, *Parametric Study on the Evolution of Thermal Patterns and Coherent Flow Structures in the Rotated Arc Mixer*, 66th Annual Meeting of the APS Division of Fluid Dynamics, Pittsburgh, Pennsylvania, the USA, November 24–26, 2013.

- H. Rajaei, **O. Baskan**, M. F. M. Speetjens, H. J. H. Clercx, *Experimental Investigation of Scalar Patterns in a Spatially Periodic Flow Field*, 66th Annual Meeting of the APS Division of Fluid Dynamics, Pittsburgh, Pennsylvania, the USA, November 24–26, 2013.

- **O. Baskan**, M. F. M. Speetjens, G. Metcalfe, H. J. H. Clercx, *Experimental Investigation of Flow and Thermal Patterns in the Rotated Arc Mixer*, 65th Annual Meeting of the APS Division of Fluid Dynamics, San Diego, California, the USA, November 18–20, 2012.

- R. T. M. Jilisen, P. R. Bloemen, **O. Baskan**, M. F. M. Speetjens, *Three-dimensional measurement of laminar flow inside a static mixer*, 9th European Fluid Mechanics Conference, Rome, Italy, September 9–13, 2012.

- **O. Baskan**, M. F. M. Speetjens, G. Metcalfe, H. J. H. Clercx, *Experimental Investigation of Flow and Thermal Patterns in the Rotated Arc Mixer*, 9th European Fluid Mechanics Conference, Rome, Italy, September 9–13, 2012.

SUMMARY

Advective-Diffusive Scalar Transport in Laminar Periodic Flows: An Experimental Investigation

Heat and mass transfer in laminar periodic flows is of practical relevance to various industrial thermo-fluid processes that employ the inline mixing principle. Today's technology in inline mixing systems is based on empirical knowledge; yet, further advancement is feasible if fundamental transport mechanisms are well-understood. In the past few decades the fundamentals and applications of mass/scalar transport in laminar periodic flows have been studied in numerous theoretical and numerical investigations. Nevertheless, a complete understanding is not achieved yet. Particularly, the experimental observations are limited, i.e., restricted to highly-idealized flow geometries or allowing only partial access to the flow domain with (optical) diagnostic tools (Kusch and Ottino, 1992; Metcalfe et al., 2006). The work presented here aims to fill this gap via laboratory experiments in real mixer geometries.

The main focus is the experimental investigation of advective-diffusive scalar transport in time-periodic and spatially-periodic laminar flows and the strategy leans on the application of both Lagrangian and Eulerian methods. There are two distinct experimental facilities which employ state-of-the-art measurement techniques: the simplified Rotated Arc Mixer (RAM) facility for fundamental research in two-dimensional (2D) time-periodic flows and the Quatro Mixer facility for three-dimensional (3D) spatially-periodic flows (with industrial relevance).

The design of the RAM facility is based on a 2D time-periodic simplification of the 3D spatially-periodic RAM, where the cross-sectional progression is represented by the temporal evolution. Particle image velocimetry (PIV), infrared thermography (IRT) and dye visualization experiments are conducted to acquire the piece-wise steady velocity field, the evolution of the temperature field and the evolution of the concentration field in time, respectively. Dynamic mode decomposition (DMD) is applied to the time-resolved temperature field data to determine the dominant eigenmodes of the evolution. The comparative analysis of the theoretical, numerical and experimental dominant eigenmodes shows that the outcomes of the different methods agree well with each other.

Moreover, the Hamiltonian progression of the Lagrangian dynamics from an integrable to a chaotic state in 2D time-periodic RAM flow is visualized via direct measurement of Poincaré sections. The close agreement between simulated and measured dynamics validates this Hamiltonian progression, which is the fundamental route to chaotic dynamics in the considered class of flows. Furthermore, a parametric study on the advective-diffusive scalar transport in the limit of infinite Péclet number by measuring concentration fields and acquiring Poincaré sections is conducted. This set of experiments reveals how the global transport relies on the kinematic/geometric parameters governing the advection. Moreover, the results show that the scalar fields under the effect of the 2D time-

periodic flow retain the fundamental properties of the scalar fields in the 3D spatially-periodic flow.

The experiments conducted in the optically-accessible test section of the Quatro Mixer facility are two-fold: 3D Particle Tracking Velocimetry (3D PTV) for the acquisition of 3D flow field and 3D Laser-Induced Fluorescence (3D LIF) for the concentration field measurements. In the former, the velocity field and particle trajectories are reconstructed from instantaneous particle positions via 3D PTV algorithm and the experimental outcomes are compared to the numerical counterparts. Downstream evolution of the concentration field is investigated in the latter class of experiments via reconstruction of 3D fields from 2D intensity images and compared to the simulated concentration field. Despite the imperfections in the experiments, there is a good agreement between experimental and numerical results, which opens the way to detailed experimental measurement of mixing efficiency (and its optimization) in devices with a variety of geometries.

In conclusion, the experimental analyses presented in this thesis deepen the insight into the fundamentals of advective-diffusive scalar transport (in generic mixing devices). Moreover, the results validate the findings of theoretical and numerical research. The methodology followed within this framework is promising for future studies in order to understand and optimize mixing in industrial mixing devices.

SAMENVATTING

Advectief-Diffusief Scalair Transport in Laminaire Periodieke Stromingen: Een Experimentele Studie

Warmte- en massaoverdracht in laminaire periodieke stromingen is van praktisch belang voor een scala aan industriële thermo-fluidische processes die gebruik maken van het zogenaamde "inline" mengprincipe. De hedendaagse mengtechnologie is grotendeels gebaseerd op empirische kennis; verdere ontwikkeling is echter mogelijk als fundamentele transport mechanismes beter worden begrepen. In de afgelopen decennia zijn de fundamentele fysica en toepassing van massa/scalair transport in laminaire periodieke stromingen onderzocht in een reeks theoretische en numerieke studies. Desalniettemin is een volledig begrip nog steeds niet bereikt. Met name experimentele observaties zijn beperkt en betreffen doorgaans sterk geïdealiseerde stromingsgeometrien of systemen die slechts deels toegankelijk zijn voor optisch meettechnieken (Kusch en Ottino, 1992; Metcalfe et al., 2006). Het hier gepresenteerde werk poogt deze leegte op te vullen middels laboratorium experimenten in realistische mengergeometrien.

De nadruk ligt op experimenteel onderzoek van advectief-diffusief scalair transport in (temporeel en spatieel) periodieke laminaire stromingen, waarbij zowel Euleriaanse als Lagrangiaanse methodieken worden toegepast. Hiertie zijn twee experimentele opstellingen gerealiseerd die gebruik maken van geavanceerde meettechnieken: de vereenvoudigde "Rotated Arc Mixer" (RAM) opstelling voor fundamenteel onderzoek aan tweedimensionale (2D) temporeel periodieke stromingen en de "Quatro menger" opstelling voor drie-dimensionaal (3D) spatieel periodieke stromingen (met industriële relevantie). Het ontwerp van de RAM opstelling is gebaseerd op een 2D temporeel periodieke vereenvoudiging van de 3D spatieel periodieke RAM, waarbij de progressie in opeenvolgende dwarsdoorsnedes van de 3D RAM wordt gerepresenteerd door de temporele evolutie in de 2D RAM. Experimenten zijn uitgevoerd in de 2D RAM met behulp van "Particle image velocimetry" (PIV), infrared thermografie (IRT) en kleurstofvisualisatie ter verkrijging van respectievelijk het stuksgewijs stationaire snelheidsveld, de temporele evolutie van het temperatuurveld en de temporele evolutie van concentratievelden. Data analyse middels "Dynamic mode decomposition" (DMD) is toegepast op de data van het temperatuurveld ter bepaling van de dominante eigenmodes van de evolutie. De vergelijkende analyse van de theoretische, numerieke en experimentele dominante eigenmodes toont dat de uitkomsten van de verschillende methodes goed in overeenstemming zijn met elkaar.

Daarnaast is de Hamiltoniaanse progressie van de Lagrangiaanse dynamica van een integreerbare naar een chaotische toestand in de 2D temporeel periodieke RAM gevisualiseerd door middel van directe metingen van Poincaré secties. De nauwe overeenkomst tussen gesimuleerde en gemeten dynamica valideert deze Hamiltoniaanse progressie, welke de fundamentele route naar chaotische dynamica is in de beschouwde klasse van stromingen. Verder is een parametrische studie uitgevoerd aan het advectief-diffusief

scalair transport in de limiet van een oneindig Péclet getal door meting van concentratie-velden en bepaling van Poincaré secties. Deze serie van experimenten laat zien hoe het globale transport afhangt van de kinematische en geometrische parameters die de advec-tie bepalen. Bovendien laten deze resultaten zien dat de scalaire velden voor de 2D tem-poreel periodieke stroming de fundamentele eigenschappen van de scalaire velden van de 3D spatieel periodieke stroming behouden.

De experimenten uitgevoerd in de optisch toegankelijke test sectie van de Quatro men-ger zijn tweeledig: "3D Particle Tracking Velocimetry" (3D PTV) voor het verkrijgen van het 3D snelheidsveld en "3D Laser-Induced Fluorescence" (3D LIF) 'voor de metingen van het concentratieveld. Bij 3D PTV worden snelheidsveld en deeltjesbanen gereconstrueerd uit instantane deeltjesposities via een dataverwerkingsalgoritme en de uitkomsten daarvan worden vergeleken met numerieke tegenhangers. De stroomafwaartse evolutie van het concentratieveld is onderzocht middels 3D LIF via de reconstructie van 3D velden uit 2D intensiteitsbeelden en vergeleken met het gesimuleerde concentratieveld. Ondanks de imperfecties in de experimenten is er een goede overeenkomst tussen experimentele en numerieke resultaten, wat het pad effent naar gedetailleerde experimentele metingen van de mengefficientie (en de optimalisitie daarvan) in apparaten met verschillende geome-trien.

Ter conclusie, de experimentele analyses gepresenteerd in deze dissertatie verdiepen het inzicht in de fundamentele mechanismen van advectief-diffusief scalair transport (in generieke mengapparatuur). Bovendien valideren de resultaten de bevindingen van theo-retisch en numeriek onderzoek. De aanpakken zoals gevolgd in dit kader zijn veelbelovend voor toekomstige studies voor het begrijpen en optimaliseren van menging in industriële mengers.

ACKNOWLEDGMENTS

CURRICULUM VITÆ

Özge BAŞKAN

01-01-1985   Born in Ankara, Turkey.

EDUCATION

2010–2015   **Doctor of Philosophy**
                   Thesis Title: *Advective-diffusive scalar transport in laminar periodic flows:*
                   an experimental investigation,
                   Applied Physics Department,
                   Eindhoven University of Technology, Eindhoven, The Netherlands.

2009–2010   **Research Master**
                   Project Title: *Aerosol deposition in lung airways: oscillatory flow*
                   characteristics and particle behavior in an expanding/contracting airway,
                   Environmental and Applied Fluid Dynamics Department,
                   von Karman Institute for Fluid Dynamics, Rhode-Saint-Genése, Belgium.

2007–2009   **Master of Science**
                   Thesis Title: *Experimental and numerical investigation of flow field around*
                   flapping airfoils making figure-of-eight in hover,
                   Aerospace Engineering Department,
                   Middle East Technical University, Ankara, Turkey.

2002–2007   **Bachelor of Science**
                   Aerospace Engineering Department,
                   Middle East Technical University, Ankara, Turkey.

EXPERIENCE

2010–2015	**Ph.D. Researcher** Project Title: *Lagrangian "mixing analysis" of heat transfer: a new way for thermal optimisation,* Applied Physics Department, Eindhoven University of Technology, Eindhoven, The Netherlands.
2008–2009	**Researcher** Topic: *CFD analysis of a tactical unmanned air vehicle,* Aerospace Engineering Department, Middle East Technical University, Ankara, Turkey.
2006–2008	**Researcher** Topic: *Small-scale turbomachinery design and manufacturing,* Aerospace Engineering Department, Middle East Technical University, Ankara, Turkey.